

Passive Noise Control by Means of
Micro-Perforated Plates:
Developing Tools for an Optimal Design

To my beloved wife...



The presented work is part of the Marie Curie Initial Training Network “Thermoacoustic and Aeroacoustic Non-linearities in Green combustors with Orifice structure” (TANGO). We gratefully acknowledge the financial support from the European Commission under call FP7-PEOPLE-ITN-2012.

A catalogue record is available from the Eindhoven University of Technology Library.

ISBN: 978-90-386-4273-4

Typeset with \LaTeX .

Cover design: Yolanda Temiz, Eindhoven, the Netherlands.

Printed by Proefschriftmaken, Vianen, the Netherlands.

©2017 by M.A. Temiz. All rights reserved.

Passive Noise Control by Means of
Micro-Perforated Plates:
Developing Tools for an Optimal Design

PROEFSCHRIFT

ter verkrijging van de graad van doctor aan de Technische Universiteit Eindhoven, op gezag van de rector magnificus prof.dr.ir. F.P.T. Baaijens, voor een commissie aangewezen door het College voor Promoties, in het openbaar te verdedigen op donderdag 18 mei 2017 om 16:00 uur.

door

Muttalip Aşkın Temiz

geboren te Erbaa, Turkije

Dit proefschrift is goedgekeurd door de promotoren en de samenstelling van de promotiecommissie is als volgt:

voorzitter:	prof.dr.ir. A.A. van Steenhoven
1 ^e promotor:	prof.dr.ir. I. Lopez Arteaga
2 ^e promotor:	prof.dr.ir. A. Hirschberg
externe leden:	prof.dr. Y. Aurégan (LAUM) prof.dr. M. Åbom (KTH)
overige leden:	dr.ir. M.C.J. Hornikx
lid TU/e:	prof.dr. H. Nijmeijer

Het onderzoek of ontwerp dat in dit proefschrift wordt beschreven is uitgevoerd in overeenstemming met de TU/e Gedragscode Wetenschapsbeoefening.

Societal Summary

Noise is defined as the ‘undesired sound waves’ and usually considered as a problem of comfort. However, in various industrial applications from power generation with gas turbines to heating with domestic burners, the undesired sound waves produced by the combustion process (combustion noise) can threaten the efficiency of the system. This phenomenon is called ‘combustion instability’ and it can even cause mechanical failures. However, combustion instability can be prevented if the produced noise is suppressed by means of a sound absorber.

Micro-perforated plates (MPPs) are new-generation sound absorbers. They are plates with very small perforations (holes) whose diameter is in the order of a millimeter and the total area of the perforations is about 1% of the whole plate area. When they are supported with a back cavity and tuned for a certain frequency range, MPPs can efficiently absorb sound. They can be made of various materials from metal to textile, therefore their area of utilization is quite wide. The freedom in material choice makes them a promising candidate for sound absorption in hostile environments like combustion systems, aircraft engine casings, domestic boilers, car mufflers, etc. Nevertheless, since they are rather new, our knowledge about the sound absorption mechanism of such plates is limited.

The study presented in this thesis aims to gain more insight about the physical mechanism that causes sound absorption in micro-perforated plates so that more efficient designs can be made with less cost. To achieve this goal, experiments and computer simulations are performed. The effect of perforation size, plate thickness, open area ratio to the whole plate, perforation edge profile, plate flexibility and sound amplitude is investigated both experimentally and numerically. A numerical design tool is proposed to allow the optimal design of a flexible MPP.

The outcomes of the study presented in the thesis can be used for designing MPPs more accurately for increasing the efficiency of various industrial applications prone to combustion noise.

Contents

1	Introduction	1
1.1	Motivation	1
1.2	Micro-Perforated Plates	2
1.3	Problem Definition	4
1.4	Objective and Research Method	5
1.5	Contributions	5
1.6	Organization of the Thesis	6
2	The Influence of Edge Geometry on End-Correction Coefficients in Micro-Perforated Plates	7
2.1	Introduction	8
2.2	Theoretical Background	10
2.3	Numerical Set-up	11
2.4	Experimental Verification	13
2.5	Results	21
2.5.1	Perforations with square edges	22
2.5.2	Perforations with chamfered edges	23
2.5.3	Combinations of edge geometries	25
2.6	Concluding Remarks	27
3	Non-linear Acoustic Transfer Impedance of Micro-perforated Plates with Circular Orifice	29
3.1	Introduction	30
3.2	Theoretical Background	32
3.2.1	Strongly non-linear regime: $Sr \ll 1$	33
3.2.2	Almost linear regime: $Sr > 1$	34
3.2.3	Transition regime: $Sr = \mathcal{O}(1)$	35

3.3	Experiments	35
3.3.1	Properties of the setup	35
3.3.2	Properties of the DAQ system	37
3.3.3	Measurement method	37
3.3.4	Measuring $ \hat{u}_p $	38
3.3.5	Specifications of the samples	39
3.4	Results and Discussions	40
3.5	Conclusions	45
4	Effect of Orifice Edge Profile on Non-linear Acoustic Response	47
4.1	Introduction	48
4.2	Theoretical Background	49
4.3	Experiments	53
4.3.1	Description of the set-up	54
4.3.2	Description of the samples	55
4.3.3	Measurement procedure	57
4.3.4	Post-processing	58
4.4	Results and Discussions	58
4.4.1	Non-dimensional parameters	58
4.4.2	Effect of edge profile	59
4.4.3	Sound generation in higher harmonics	59
4.5	Conclusions	63
5	Building a Numerical Model to Investigate the Effect of Perforation Distribution in Flexible Micro-Perforated Plates	67
5.1	Introduction	68
5.2	Theoretical Background	70
5.2.1	Structural domain	70
5.2.2	Acoustic domain	71
5.3	Numerical Model	72
5.3.1	Boundary conditions	72
5.3.2	Finite element model	74
5.3.3	Meshing	74
5.3.4	Estimation of the absorption coefficient	75
5.3.5	Compensation for inviscid reactance	75
5.4	Validation of the Discrete Numerical Model and Discussions	80
5.4.1	Rigid plate	81
5.4.2	Flexible plate	83
5.5	Parametric Study Example	87

5.5.1	Influence of Plate Thickness	87
5.5.2	Influence of Distribution of the Perforations	92
5.6	Conclusions	96
6	Conclusions and Recommendations	99
6.1	Conclusions	99
6.2	Recommendations	101
	Appendices	103
A	Impedance Tube Set-Up	105
A.1	Technical Description	105
A.2	Signal Processing Techniques for Impedance Tube Measurements . .	105
A.2.1	Signal filtering	109
A.2.2	Converting measurement data to frequency domain	109
A.3	Calibration Procedure	112
A.3.1	Absolute and Relative Calibration	112
A.4	Multi-Microphone Method and Reflection Coefficient Measurements .	114
A.5	Validation	115
A.5.1	Correcting the microphone positions	116
A.6	Miscellaneous Precautions	120
B	Mesh Convergence	121
	Bibliography	125
	Summary	132

Chapter 1

Introduction

1.1 Motivation

The global mean temperature of our planet has risen by 1°C in the last 40 years [1, 2]. This is the record high value since it is being measured. This grim situation will not get any better if necessary measures are not taken. Many countries, companies and institutions are aware of this problem and they are trying to fight it with reducing the carbon emission in every way possible. Besides changing the regulations to reduce the emissions, it is important to provide the knowledge to the public to achieve this objective.

Combustion is everywhere: from a domestic boiler to a gas power plant whose output power is hundreds of mega-watts. Reducing the emissions in such devices requires increasing the efficiency. However, high efficiency combustors are more sensible to combustion instabilities [3]. As shown in Figure 1.1, it is a self-sustaining feedback mechanism in which the acoustics plays an important role. The heat release causes pressure perturbations, which generates acoustic waves. If the acoustic pressure oscillations are in phase with the heat release oscillations, then the perturbations are amplified at each cycle. In some cases this amplification can continue until a mechanical failure takes place [4].

TANGO, Thermoacoustic and Aeroacoustic Non-linearities in Green Combustors with Orifice Structures, is a European Commission funded project (FP7-PEOPLE-ITN-2012) that has been set-up for producing the knowledge for more environmental-friendly combustors. Its mission is defined as “To develop green combustion technologies and noise control methods in a gender-balanced, multi-disciplinary net-

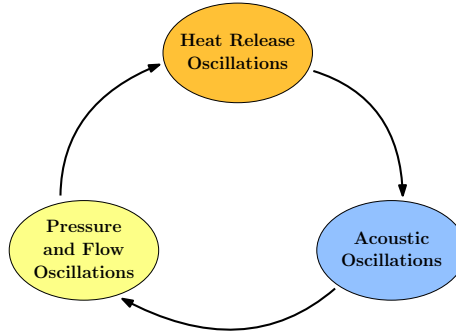


Figure 1.1: Feedback mechanism responsible from thermoacoustic instabilities.

work with academic and industrial collaboration, while also training highly skilled scientists of the future” [5]. One way to avoid or reduce the combustion instabilities is to break the feedback mechanism described in Figure 1.1. To achieve this, the present thesis consider the use of passive control by micro-perforated plates.

1.2 Micro-Perforated Plates

Micro-perforated plates (MPPs) are plates with orifices whose diameter (d_p) is in the order of 1 mm and the open area to the plate surface ratio, *i.e.* porosity (ϕ), is in the order of 1% for such plates. Moreover, the thickness of an MPP (t_p) is typically chosen as comparable to its perforation diameter, $t_p/d_p \sim \mathcal{O}(1)$. They are used with a back cavity [6].

The distinction between an MPP and a regular perforated plate is made through the definition of the *Shear number* Sh . It is the ratio of the perforation radius ($d_p/2$) to the oscillating viscous boundary layer (Stokes layer) thickness ($\sqrt{\nu/\omega}$), where ν is the kinematic viscosity of the acoustic medium and $\omega = 2\pi f$ is the angular frequency of the sound excitation [7]. When $Sh = d_p \sqrt{\omega/(4\nu)} \simeq 1$ for a perforated plate, the oscillating viscous boundary layers occupy the entire perforation cross-section, therefore it is considered as an MPP. Moreover, the small porosity value of an MPP ensures that the particle velocity amplitude in the perforations becomes large, resulting in a larger energy dissipation due to viscosity.

A single perforation in an MPP and its surroundings is similar to a Helmholtz resonator: they both have a perforation (neck) and a reacting backing volume. However, due to the typical size of the perforations in MPPs, acoustic particles trying to

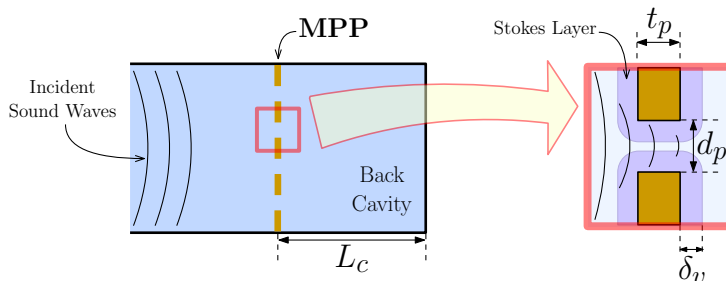


Figure 1.2: MPP in a duct: d_p is the perforation diameter, t_p is the plate thickness, L_c is the back cavity depth and δ_v is the Stokes layer thickness. The incident sound waves are absorbed due to viscosity in the perforations.

pass through experience viscous forces resulting from the Stokes layers as illustrated in Figure 1.2, whereas for Helmholtz resonators the viscous effects are negligible. This is the main difference between an MPP and the Helmholtz resonator. It is possible to model the Helmholtz resonator as a mass-spring system [8], where a single perforation in an MPP is required to be represented as a mass-spring-viscous damper system. Therefore, a Helmholtz resonator is a very effective absorber only at its resonance frequency whereas an MPP has a more broadband acoustic response yet a lower maximum absorption peak [9].

Micro-perforated plates (MPPs) have been used in sound absorption for more than 40 years. However, their primary area of usage has been limited to room acoustics until Maa [6] revealed their potential for the industrial applications. It should be noted that such applications exhibit a different acoustic problem since the frequency span of interest is less than 1 kHz [10], therefore the dissipation characteristics of MPPs is expected to be different. Nevertheless, the suitability of MPPs for industrial applications is based on several reasons: (i) Their acoustic performance is robust compared to classical acoustic absorbers having fibrous structure since their geometrical properties are harder to change in time [6]. (ii) Unlike classical sound absorbers, MPPs do not contaminate the acoustic medium with small particles breaking off from the absorber [11]. (iii) MPPs can be made from any material so that they can be more compact, lightweight and durable [6]. As a result, they are considered as promising sound absorbers to reduce the acoustic reflections from the intake of a combustion system [12, 13].

The viscous thermal dissipation of acoustic waves in stagnant fluid due to propagation in a long capillary has been studied by Kirchhoff [14]. However, Maa [6]

is the first scientist to combine this theory with the end-corrections proposed by Ingard [15] in order to predict the acoustic behaviour of perforations in a relatively thin plate. Besides, since the typical porosity of the plate is in the order of 1%, interaction between the neighbouring perforations is neglected. Hence, Maa [6] proposes a simple but very practical design expression for the linear transfer impedance of an MPP which depends only on the following parameters: perforation diameter d_p , plate thickness t_p , porosity ϕ , back cavity depth L_c and excitation frequency f .

The expression proposed by Maa [6] is valid in the linear regime. The acoustic linearity of a perforation is defined by the ratio of its diameter (d_p) to the acoustic particle displacement amplitude ($|\hat{u}_p|/\omega$), where $|\hat{u}_p|$ is the acoustic velocity amplitude of a particle in the perforation. This ratio is referred to as the Strouhal number [16]. The acoustic response of a perforation is linear when $Sr \gg 1$ and it is non-linear when $Sr \ll 1$. In the non-linear regime, the resistance of the perforations increases as the excitation amplitude increases [17, 18]. Attenuating the large amplitude standing waves in launcher fairings [11], noise reduction at the aircraft engine casings [9] and mufflers [19] are among the typical applications which require dealing with non-linear acoustic response of MPPs.

1.3 Problem Definition

Although MPPs have so many advantages, there are aspects requiring further study in order to utilize their full potential. Firstly, the end-corrections used by Maa [6] have been proposed for the limit where viscous forces are neglected, *i.e.* $Sh \gg 1$. This is a contradiction to the MPP concept. The difference between the theory and measurements is removed by choosing arbitrary factors for the end-correction coefficients found in various publications, mostly between 1 and 4 [6, 20, 21, 19]. This has been linked with edge profile of the perforation [19], however there has been limited study addressing this problem.

In addition, while the acoustic response of MPPs are proposed by Maa [6] in the linear regime, Ingard and Ising [18] have modelled the sound absorption of a perforation in the strongly non-linear regime, *i.e.* exposed to high-amplitude excitation. These two models explain the acoustic response of MPPs in the two limits, yet the transition between them has not been investigated systematically.

Moreover, depending on the material selection, structural vibrations can become a parameter defining the acoustic response of the MPP. For example, Lee and Swenson [22] have observed additional absorption peaks in their measurements with flexible MPPs. It is a challenging task to design and optimize MPPs when flexibility of the plate is also a design parameter. Furthermore, current models are only valid

for a uniform distribution of the perforations on the plate. Considering the vibro-acoustic coupling and the mode shapes of plates, a non-uniform distribution has the possibility to improve the acoustic properties of flexible MPPs. However, there is no efficient tool to perform such a parametric study without carrying out a large number of experiments.

1.4 Objective and Research Method

The main objective of this thesis is to provide knowledge about acoustic characteristics of perforated plates and methods to design better passive sound absorbers. Therefore, not only MPPs, but also regular perforated plates ($Sh > \mathcal{O}(1)$) are studied. In the present thesis, experimental and numerical studies are performed to achieve the main objective.

The experiments are carried out in a semi-anechoic chamber with an impedance tube set-up. Depending on the parameter to measure, open or closed-end (with back cavity) measurements are performed with MPP and regular perforated plate samples.

The finite-element method (FEM) is used for the numerical studies. The commercial FEM program COMSOL[®] v. 5.0 [23] is used in the simulations. The built-in modules such as *CFD*, *Linear Acoustics* and *Structural Mechanics* are made use of as well as its *Partial Differential Equation Interface*. The simulation results are validated with theory and measurements before conclusions are drawn.

On the other hand, the present thesis focuses only on circular perforations. Moreover, the effect of mean flow (grazing or bias flow) is not considered in the experiments or simulations.

1.5 Contributions

The main objective of the present thesis is achieved through the following contributions:

- The ambiguity about the end-correction coefficients for circular orifices and micro-perforations in the literature is resolved by proposing new expressions in the linear regime, which are functions of edge profile and Shear number.
- Expressions are proposed to describe the evolution of the acoustic response of MPPs from linear regime to non-linear regime.

- A numerical design and optimization tool, which employs a patch-impedance approach, is proposed for flexible MPPs. Due to this approach, the numerical tool enables to include the spatial effects of the perforation distribution and interaction between them.

1.6 Organization of the Thesis

The findings of this work have been used for preparing four journal paper manuscripts. Two of these manuscripts are already published and the other two are submitted. The thesis is organized in a way that each chapter covers the content of these manuscripts individually. **Chapter 2** discusses the linear edge effects of a circular perforation on estimating the end-correction coefficients with the help of an experimentally verified numerical model. **Chapter 3** investigates the acoustic response of micro-perforations in the transition between linear and strongly non-linear regimes. The effect of edge profile of perforations on acoustic response in non-linear regime is studied in **Chapter 4**. In **Chapter 5**, the structural vibration effects are included in the linear model and a numerical method to design flexible micro-perforated plates is proposed. The conclusions are summarized in **Chapter 6** and recommendations are given for a future study. Finally, some complementary information such as details of the measurement set-up, mesh study for the proposed numerical model, etc. are provided in **Appendices**.

Chapter 2

The Influence of Edge Geometry on End-Correction Coefficients in Micro-Perforated Plates¹

Abstract

Global expressions are proposed for end-correction coefficients in micro perforated plates (MPPs) using non-dimensional parameters. MPPs are sound absorbers with small perforation diameters so that the Stokes boundary layers fill up almost the entire perforation. Sound absorption does not only occur within the perforation, but also takes place just outside of it. The latter contribution plus the outside inertia effect on the transfer impedance of the MPP is referred to as end-corrections. In order to determine them, an analytical solution employing the very thin Stokes layer assumption has been derived. However, this assumption requires empirical coefficients in the end-corrections for accurate results. To explore the effects of various parameters a numerical model is used. This model is verified with open-end reflection coefficient measurements. The most prominent result from this study is that compared to plate thickness, the ratio of perforation diameter to Stokes layer

¹The content of this study is published in *The Journal of the Acoustical Society of America* by Temiz *et al.* [24].

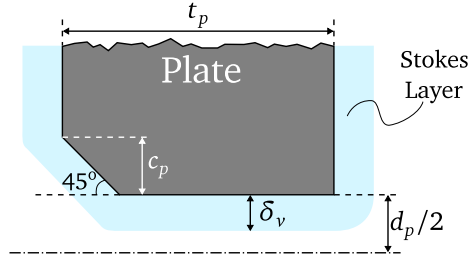


Figure 2.1: Representation of the Stokes layer ($\delta_v = \sqrt{\mu/(\rho_0\omega)}$) within a single perforation of an MPP in 2D-axisymmetrical geometry. The parameters defining perforation diameter (d_p), plate thickness (t_p), and chamfer length (c_p) are also shown on the figure.

thickness (Shear number) and edge geometry affect the end-correction coefficients more significantly. The effect of plate thickness can be neglected for practical purpose, therefore expressions for the end-corrections in terms of Shear number and edge geometry are provided. The relative error of these expressions are less than 3% compared to the numerical results.

2.1 Introduction

Micro perforated plates (MPPs) are plates with perforations whose diameter is in the order of a millimeter and with a low porosity, *i.e.* $\sigma = \mathcal{O}(1\%)$. Due to the small diameter size, the oscillating viscous boundary layers, *i.e.* Stokes layers, cover the majority of the perforation as can be seen in Figure 2.1.

MPPs are identified as efficient absorbers by Maa [6]. He combines the oscillating viscous flow in a capillary tube solution from Crandall [25], which is a simplified version of the visco-thermal derivation of Kirchhoff [14] with the end-corrections of Ingard [15]. This way, Maa [6] derives a *transfer impedance* expression for a single perforation. Nevertheless, Ingard [15] bases his end-correction coefficient derivation on very thin Stokes layer assumption. Thus, this model does not represent the acoustic behaviour of MPPs for Stokes boundary layers as thick as the perforation radius. Plus, this is an unrealistic assumption for the geometry neglecting completely the edge effect.

Consequently, the analytical model of Maa [6] requires empirical coefficients to match the experimental results. Especially the coefficient for the resistive end-

correction (α) varies between 2 and 4 in literature and this has been associated with edge geometry by Allam and Åbom [19]. On the other hand, the theoretical limit value for the reactive end-correction coefficient (δ) is reasonably accurate for most applications.

To solve this deficiency especially with the resistive end-correction coefficient, Bolton and Kim [26] have developed a numerical model in 2D axisymmetric coordinates. With this model they simulate viscous, incompressible, oscillating flow in the time domain. They include the end effects of the perforation by using upstream and downstream channels with fixed length of 1 mm. They have run simulations for 21 different combinations of plate thickness (t_p), perforation diameter (d_p) and porosity (σ) parameters. They propose an expression for the resistive end-correction coefficient in the dimensions of $[\text{Hz}^{-0.5}]$.

Furthermore, Herdtle *et al.* [27] have used Bolton and Kim's [26] CFD approach to compute the end-corrections for tapered perforations.

In another recent study by Carbajo *et al.* [28], a method similar to Bolton and Kim [26] is used to study the interaction between perforations. Although the two works mentioned above propose a valuable methodology, there is a need for a more generalized definition of the end-correction coefficients and experimental validation of the results. Furthermore, none of the studies discussed above consider the influence of the perforation edges on the acoustic performance of the MPP.

In this paper both the resistive and reactive end-correction coefficients are evaluated by means of an axisymmetrical, incompressible flow model in the frequency domain, and validated with experiments, also including the influence of the shape of the perforation edges. Although this approach is analogous to that of Bolton and Kim [26], the results are significantly different in the following aspects. Firstly, non-dimensional parameters are employed to express end-correction coefficients so that the results are generalized and useful for the design of MPPs with circular perforations. Secondly, linearized Navier-Stokes equations are solved numerically in the frequency domain. Moreover, it is made sure that the acoustic transfer impedance values are calculated independent of the upstream and downstream channel length. Finally, the effect of the edge profile on the end-correction coefficients is investigated. In other words, the aim of this study is to provide a consistent base for the calculation of the transfer impedance in MPPs with circular holes in the linear regime.

On the other hand, this study is limited to certain aspects. First of all, only low perforation rates ($\phi = \mathcal{O}(1\%)$) are focused so that the hydrodynamic interaction between perforations can be ignored [6, 19, 26]. Secondly, although slit shaped MPPs appear to be quite promising [19], this study concentrates on circular perforation geometries so that they can be represented in 2D axisymmetrical geometry

in numerical model. Finally, measurements with a single perforation diameter are carried out for all samples.

2.2 Theoretical Background

The transfer impedance of an MPP is defined as:

$$Z_{t-p} = \frac{\Delta \hat{p}}{\phi \hat{U}_p}, \quad (2.1)$$

where $\Delta \hat{p}$ is the *plane wave pressure* difference across the plate, ϕ is the porosity and \hat{U}_p is the volume flow rate divided by the perforation area. From experimental or simulated data, plane wave pressure is obtained on each side of the plate by extrapolating a plane wave model up to the surface of the plate. When \hat{U}_p is multiplied with ϕ , plane wave normal velocity before (or after) the plate is obtained. Please note that the circumflex accent (^) indicates complex quantity throughout this chapter.

For MPPs with circular perforations, the transfer impedance of a single perforation with a finite plate thickness is modeled by Maa [6] as follows:

$$Z_t = \frac{\Delta \hat{p}}{\hat{U}_p} = j\omega t_p \rho_0 \left[1 - \frac{2}{Sh\sqrt{-j}} \frac{J_1(Sh\sqrt{-j})}{J_0(Sh\sqrt{-j})} \right]^{-1} + 2\alpha R_s + j\delta\omega\rho_0 \frac{d_p}{2}, \quad (2.2)$$

using the $\exp(j\omega t)$ convention.

The first term in the right-hand side of Eq. (2.2) defines the oscillating fluid flow within the perforation where $\omega = 2\pi f$ is the radial frequency, ρ_0 is the density of air (1.184 kg/m³ @20°C, 1.205 kg/m³ @25°C), j is the imaginary number $\sqrt{-1}$, J_n is the Bessel function of 1st kind of order n and Sh is the Shear number which is defined [29] as $Sh = d_p \sqrt{\omega\rho_0}/(4\mu)$ where μ is the dynamic viscosity of air (1.82 × 10⁻⁵ kg/ms @20°C, 1.84 × 10⁻⁵ kg/ms @25°C).

The second term in the right-hand side of Eq. (2.2) is the resistive and the last one is the reactive (inertial) end-correction expressions, respectively. R_s is the surface resistance on one side of the plate which is calculated by $R_s = 0.5\sqrt{2\mu\rho_0\omega}$. Moreover, the non-dimensional resistive and the reactive end-correction coefficients are denoted by α and δ in Eq. (2.2). The end effects become very important in plates with normalized thickness, $t^* = t_p/d_p$, in the order of unity.

Even though Maa [6] has proposed his analytical model for the sharp-edge perforation case, the presence of end-correction coefficients in the model provides the flexibility to include different edge types.

This study starts with the sharp-edge case and then, extends for various types and combinations for chamfered edges. The behaviour of the chamfered edges are expected to be similar to those with rounded edges. Chamfers are preferred to roundings due to manufacturing accuracy.

2.3 Numerical Set-up

The numerical part of the study contains a model tailored to a single perforation. A viscous, incompressible flow in 2D axisymmetric coordinates is assumed. To compare the results with Maa's linear model [6] and extend it further, the calculations are kept in the linear regime also. As a result, the following linearized incompressible Navier-Stokes equations in the frequency domain are solved in the model:

$$\frac{\partial \hat{u}_r}{\partial r} + \frac{\hat{u}_r}{r} + \frac{\partial \hat{u}_z}{\partial z} = 0, \quad (2.3a)$$

$$j\rho_0\omega\hat{u}_r + \frac{\partial \hat{p}}{\partial r} - \mu \left(\frac{\partial^2 \hat{u}_r}{\partial r^2} + \frac{1}{r} \frac{\partial \hat{u}_r}{\partial r} + \frac{\partial^2 \hat{u}_r}{\partial z^2} \right) = 0, \quad (2.3b)$$

$$j\rho_0\omega\hat{u}_z + \frac{\partial \hat{p}}{\partial z} - \mu \left(\frac{\partial^2 \hat{u}_z}{\partial r^2} + \frac{1}{r} \frac{\partial \hat{u}_z}{\partial r} + \frac{\partial^2 \hat{u}_z}{\partial z^2} \right) = 0, \quad (2.3c)$$

where r and z represents the radial and axial axes components; ρ_0 represents the base flow density; \hat{u} and \hat{p} represent acoustic velocity and pressure. In COMSOL Multiphysics[®] [23], Eq. (2.3) is discretized using finite elements in the *Coefficient Form PDE* module of the program. In the simulations, quadratic elements are used. Since the flow is laminar, no turbulence model was needed. A schematic drawing of the computational domain and the boundary conditions used are presented in Figure 2.2.

As can be seen from Figure 2.2, the geometry covers both inner and outer regions of the perforation. The outer region is the upstream / downstream channel and its diameter is taken as $D = d_p / \sqrt{\phi}$. Doing that, it is ensured that the effect of the perforation is negligible at the inlet and outlet boundaries. During the course of the simulations it is seen that an increase of 33% in the channel length results with a change of less than 0.001% in the pressure amplitude, which also indicates that a long enough computational domain was used. A typical pressure distribution obtained by solving linearized incompressible Navier-Stokes equations is shown in Figure 2.3.

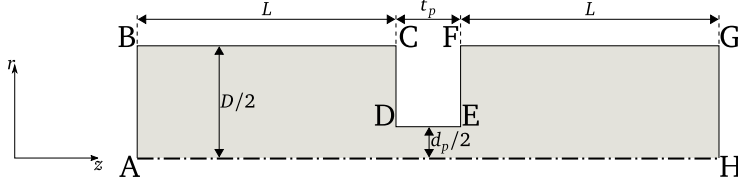


Figure 2.2: Computational domain of a single perforation. $|AB|$ harmonic velocity inlet; $|BC|$ and $|FG|$ slip wall; $|CD|$, $|DE|$ and $|EF|$ no-slip wall; $|GH|$ viscous-free, zero-pressure outlet and $|AH|$ radial symmetry axis.

The transfer impedance is calculated by dividing the acoustic pressure difference between two sides of the perforation by the volume flux per perforation area, as stated in Eq. (2.1). The relevant acoustic pressure at one side of the perforation is obtained by linear extrapolation, assuming an incompressible uniform flow, from the inlet (or the outlet) boundary of the computational domain to the surface of the perforation [27]. In this incompressible model the pressure difference ($\Delta\hat{P}$) is therefore given by

$$\Delta\hat{P} = \hat{P}_u - \hat{P}_d - j2L\rho_0\omega\hat{U}, \quad (2.4)$$

where $\hat{P}_u = \hat{p}(z_{AB})$ and $\hat{P}_d = \hat{p}(z_{GH})$ are the upstream and the downstream pressures at the inlet and the outlet of the numerical domain, respectively. Furthermore, \hat{U} is the imposed uniform inlet velocity of the model and L is the length of the upstream and downstream sections. The correction given in Eq. (2.4) ensures that $\Delta\hat{P}$ is independent of the upstream / downstream channel length.

In order to avoid the need for resolving sharp edges, fillets with small radius, r_f , are used at the edge points. The simulations are repeated for different fillet radius to perforation diameter values, r_f/d_p , such as 6.25×10^{-3} , 3.13×10^{-3} and 1.56×10^{-3} . Observing the change is linear, we extrapolate Z_{t-p} to the $r_f = 0$ case and approximate the limit value as accurately as possible.

Using this approach, not only perforations with square-edge profile but also other types of edge profiles are investigated in this study. The schematic representations of these profiles are shown in Figure 2.4.

In all the cases shown in Figure 2.4, the sharp corners are taken care of with the method mentioned above to avoid numerical singularity.

With COMSOL's built-in mesh generation tool, a mesh with non-constant distribution is built to minimize the number of grid points. This results with a combination of triangular and rectangular mesh types. Although triangular mesh dominates

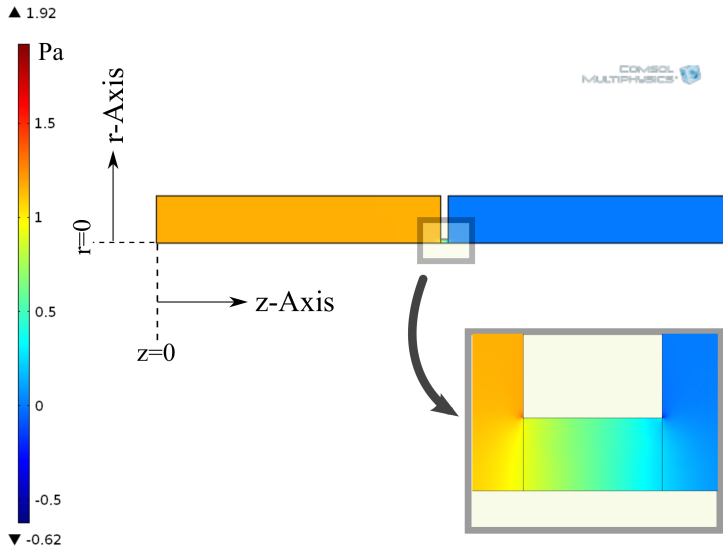


Figure 2.3: A typical pressure amplitude distribution around a perforation with the square-edge profile.

the domain; in the vicinity of the boundaries with *no-slip BC*, rectangular mesh type is present. An example for this distribution is shown in Figure 2.5.

A mesh study resulted in that, for the mesh used, the difference in the value of Z_{t-p} is less than 0.02% compared to the successive finer grid level.

2.4 Experimental Verification

The verification of the numerical model is done by comparing 4 different cases with experimental results. In all these cases, samples with a single perforation is used as in the numerical model. Their properties are given in Table 2.1 and their photo is provided in Figure 2.6.

The samples introduced in Table 2.1 are placed at the end of a 1 m long impedance tube. The tube is made of aluminium with an inner diameter of 50 mm and a wall thickness of 10 mm. A photo and a schematic drawing of the system are given in Figure 2.7.

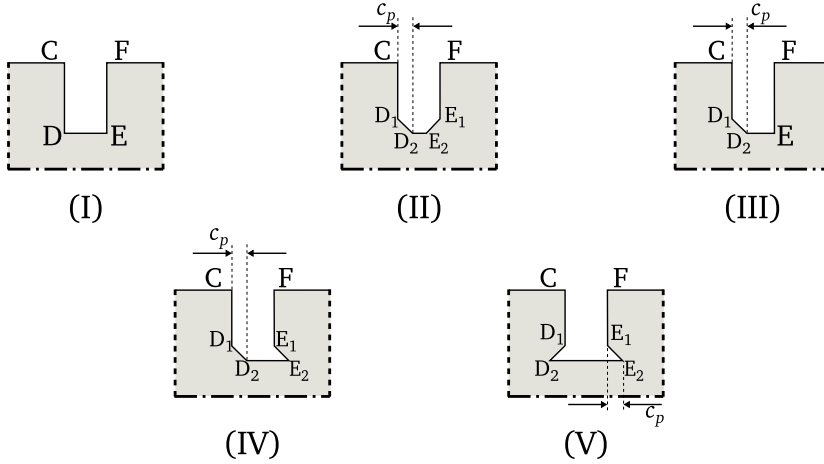


Figure 2.4: Edge geometries investigated in this study: (I) square-edge; (II) both-sides-chamfered; (III) one-side-chamfered; (IV) punched; and (V) inverse-chamfered profiles.

Table 2.1: Specifications of Sample I (square), Sample II (one-side-chamfered), Sample III (both-ends-chamfered) and Sample IV (punched).

Sample Name	d_p [mm]	t_p [mm]	ϕ	c_p [mm]
Sample I	4.20 ± 0.05	4.00 ± 0.01	0.71%	N/A
Sample II	4.20 ± 0.05	4.00 ± 0.01	0.71%	0.35 ± 0.05
Sample III	4.20 ± 0.05	4.00 ± 0.01	0.71%	1.00 ± 0.05
Sample IV	4.20 ± 0.05	4.00 ± 0.01	0.71%	1.00 ± 0.05

For data acquisition, a *NI PCIe-6361 X-Series* card with 16 analog input and 2 analog output channels is used. The signals are generated and recorded using *LabView*[®]. One output channel is used for the loudspeaker and six input channels are used for the microphones. The type of the microphones is *BSWA MPA416* with a sensitivity of 50.45 mV/Pa. They are equally distributed by a distance of 175 mm. This set-up employs the algorithm described in Figure 2.8 to perform reflection coefficient measurements.

For the calibration of the microphones, a one-time measurement is performed before the others. Using a calibration mount specially designed for this purpose,

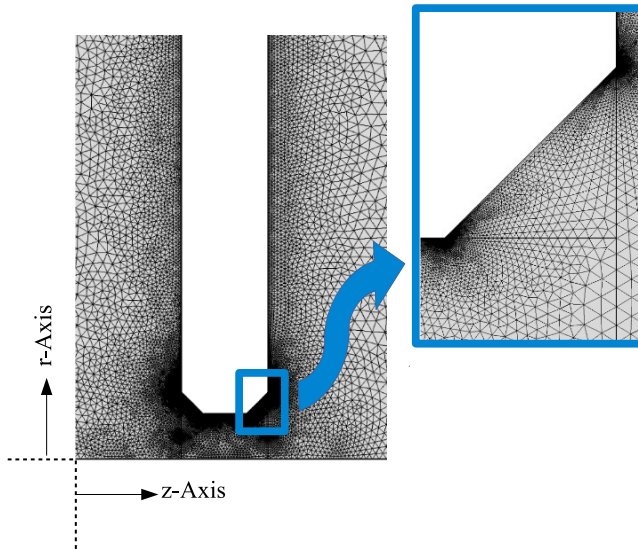


Figure 2.5: An example of how non-constant distribution of the mesh looks like around the *both-sides-chamfered* perforation. Note that the mesh is finer in the vicinity of the edges.

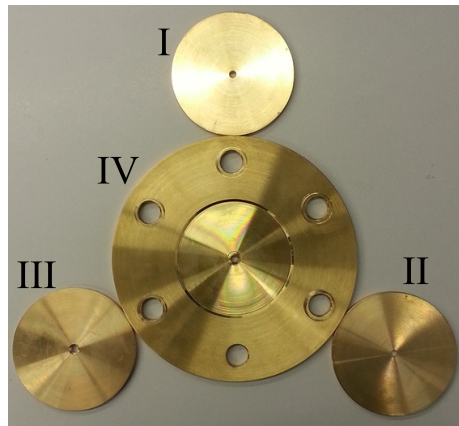


Figure 2.6: Samples used in the impedance tube to verify the numerical model. Samples I, II and III require a sample holder while Sample IV has it built-in.

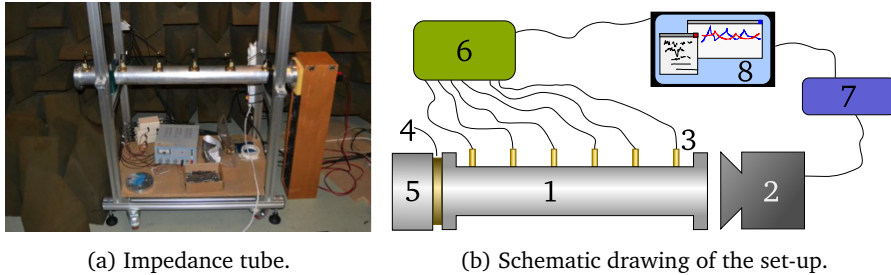


Figure 2.7: The set-up used for verification of the numerical model. (a) The photo of the set-up, (b) schematic drawing of the set-up: 1: the impedance tube, 2: loudspeaker, 3: microphones, 4: MPP sample, 5: (hollow) sample holder, 6: microphone amplifier, 7: loudspeaker amplifier, 8: analyzer and computer.

all the microphones are placed at the same distance from the loudspeaker and the closed end tube termination. The idea is that: for each frequency step, every microphone should read the same complex pressure value according to the *plane wave* assumption. As a result, one of the microphones is selected as the reference and other microphones are forced to have the same value for the same frequency. This is achieved by calculating the calibration coefficients for each frequency step. This procedure is a relative calibration technique. However, since only reflection coefficients are measured in this study, an absolute calibration is not necessary. In this technique, the arbitrarily selected reference microphone should remain the same throughout all the measurements. Finally, the microphones are relatively calibrated for the frequency range [100, 700] Hz. Please note that, although the tube allows one to carry on measurements approximately up to 3.4 kHz; considering the sample dimensions, the viscous effects are expected to be small enough to be neglected for $f > 700$ Hz ($Sh > 35$). Moreover, above this frequency, the influence of the finite compliance of the microphones becomes significant [30]. This effect is not corrected for this study.

In the measurements of MPPs, after the pressure data from the microphones are saved, the corresponding reflection coefficient for each frequency step is calculated custom-built script. This script omits the first and last 2 seconds from the measurements to avoid transient effects and uses the calibration coefficients obtained before.

Both of the scripts calculating the calibration and reflection coefficients employ a *lock-in* method [31]. This method correlates the input signal to the output to

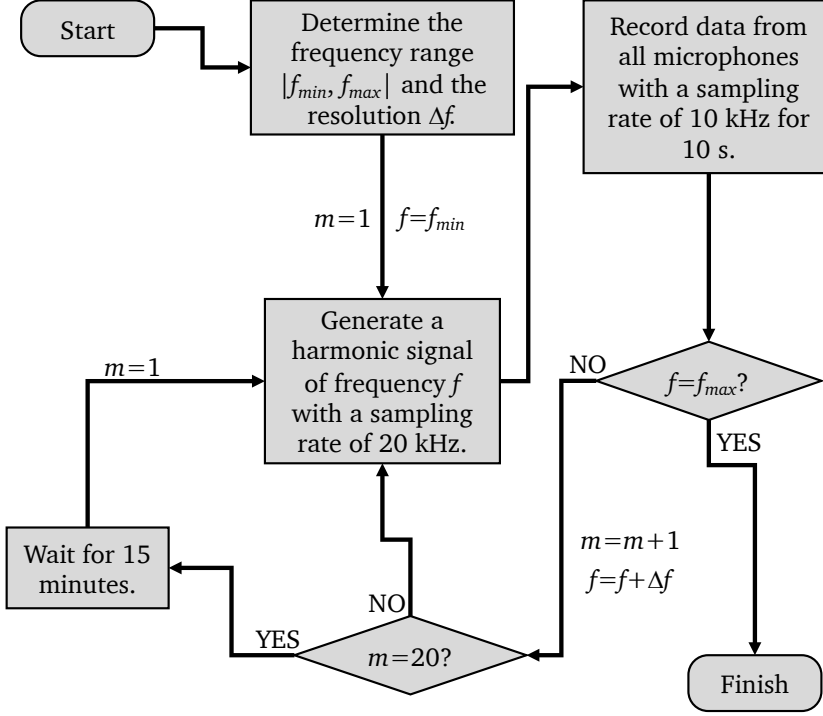


Figure 2.8: Measurement algorithm.

calculate the measurements in the Fourier domain. The advantage of this method over FFT (or DFT) is that it ensures there is no spectral leakage.

The calculation of the reflection coefficient is based on the plane wave assumption. In other words, within the tube, all the points at position z are assumed to have the same complex pressure amplitude $\hat{p}(z)$, and this can be decomposed into right, \hat{p}_+ , and left, \hat{p}_- , travelling pressure waves such as:

$$\hat{p}(z) = \hat{p}_+ \exp(-jk_c z) + \hat{p}_- \exp(jk_c z), \quad (2.5)$$

where k_c is the complex wave number taking visco-thermal effects into account and described by Peters *et al* [29] as follows:

$$k_c = \frac{\omega}{c_0} \left[1 + \frac{1-j}{\sqrt{2}Sh} \left(1 + \frac{\gamma-1}{Pr^{0.5}} \right) \right] - \frac{\omega}{c_0} \left[\frac{j}{Sh^2} \left(1 + \frac{\gamma-1}{Pr^{0.5}} - \frac{1}{2} \gamma \frac{\gamma-1}{Pr} \right) \right], \quad (2.6)$$

where Pr is the Prandtl number and γ is the heat capacity ratio. In the calculations, the term with Sh^2 is omitted since its value does not exceed 2% of the first order term in Eq. (2.6).

Introducing this complex wave number into the method of least square fit for 6 microphones by Jang and Ih [32], the plane wave decomposition is obtained and the reflection coefficient can be expressed as

$$R = \frac{\hat{p}_- \exp(jk_c z)}{\hat{p}_+ \exp(-jk_c z)}. \quad (2.7)$$

In Figure 2.8, one can see a 15-minute delay between two successive 20-step measurements. The reason of this is to restore the uniform temperature in the tube. This is due to the fact that measurements are affected by the change in the speed of sound, c_0 . For 20 frequency steps one has 40 wave amplitudes as unknown, plus c_0 as an additional unknown. The signals of the 6 microphones provide a set of 120 equations for those 41 unknowns, which is solved by the least square method proposed by Aurégan[33]. For the completely closed-end case, the deviation of the measured reflection coefficient from the theoretical value $R = 1.000$ is less than 0.3%.

The transfer impedance is measured by the following procedure:

- i. Measure the open end reflection coefficient of the open impedance tube without the sample plate, R_{OE} , and calculate the radiation impedance, Z_R , using $Z_R = \rho_0 c_0 (1 + R_{OE}) / (1 - R_{OE})$.
- ii. Place the sample plate to the end, measure the reflection coefficient of sample-loaded end, R_p , and calculate $Z_p = \rho_0 c_0 (1 + R_p) / (1 - R_p)$.
- iii. Obtain the transfer impedance of the plate, Z_{t-p} , by subtracting the radiation impedance from the sample-loaded end impedance: $Z_{t-p} = Z_p - Z_R$.

The samples are attached in between the impedance tube and the hollow sample holder (see Figure 2.7), whose inner diameter is the same as the tube and length is 1.5 times the diameter. Since tube terminations in both sample-loaded and open-end (without the sample) cases are identical and the surroundings is the same, one can expect the radiation impedance values to be the same. Besides, it should be

noted that since $\phi \sim \mathcal{O}(1\%)$ for the samples, Z_R is expected to be much lower than Z_p and the possible error is negligible in $Z_{t-p} = Z_R - Z_p$.

Being aware of the non-linearity issues in the MPP measurements, an empirical procedure is employed to avoid such effects. The excitation amplitude is decreased gradually at the lowest frequency of interest. When two successive measurements give the same reflection coefficient value, the measurements are carried out for the frequency range with that particular amplitude. This is based on the definition of Strouhal number, $Sr = \phi \omega d_p / |\hat{U}|$, by Ingard and Ising [18]. According to this definition if $Sr > 1$, one does not observe non-linear effects in the MPPs and Sr increases with increasing frequency. It is furthermore verified that Sr remains larger than unity for all the measurements given in this study.

Comparison between the numerical model and the experiments is done in terms of non-dimensional end-correction coefficients α and δ . These coefficients are calculated by rearranging Eq. (2.2);

$$\alpha = \frac{(\Re\{Z_{t-p}\} - \Re\{Z_{t-p}\}_{th})\phi}{2R_S}, \quad (2.8a)$$

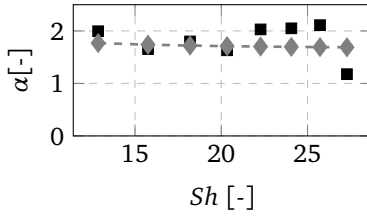
$$\delta = \frac{(\Im\{Z_{t-p}\} - \Im\{Z_{t-p}\}_{th})\phi}{\rho_0 \omega d_p / 2}, \quad (2.8b)$$

where subscript *th* represents the word *theoretical* and this corresponds to the transfer impedance calculated by means of the theory by Crandall [25]. In other words, the theoretical transfer impedance of a perforation is calculated by Eq. (2.2) without the end-corrections ($\alpha = \delta = 0$) and dividing it by the porosity (ϕ). His model takes into account only the inside of the perforation of length t_{eff} . This effective thickness can be calculated as $t_{eff} = t_p - nc_p$ with c_p is the chamfer length and the coefficient n is the edge type factor whose values for different edge types are listed in Table 2.2.

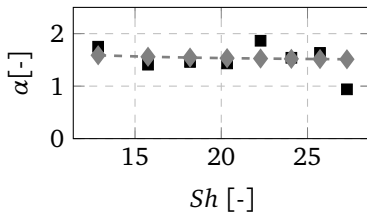
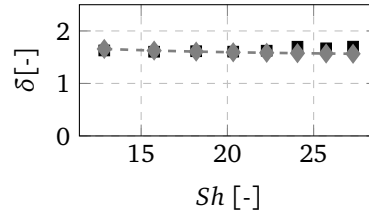
When employing Eq. (2.8) with the values of Z_{t-p} determined from measurements, one obtains experimental values for α and δ . Similarly, in order to obtain numerical end-correction coefficients, Z_{t-p} calculated by simulations should be used.

For the samples introduced in Table 2.1, the comparison between numerical and experimental end-correction coefficients is shown in Figure 2.9.

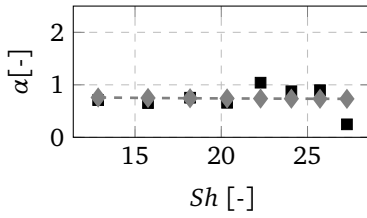
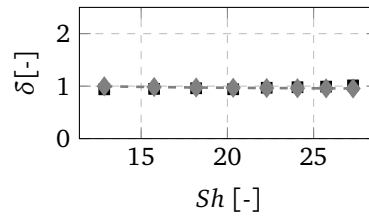
In this study, samples whose perforation diameter is rather larger than a typical MPP are concentrated on for the verification of the numerical model. This results in a higher Sh number in the frequency of interest, *i.e.* $Sh > 10$. The numerical model presented here has been already validated in the low Sh number region, $1 < Sh < 14$, for square edges [34]. In this previous study imperfections in the



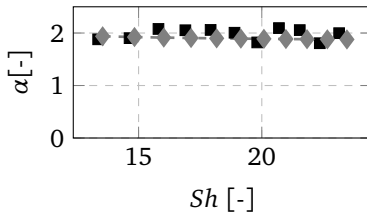
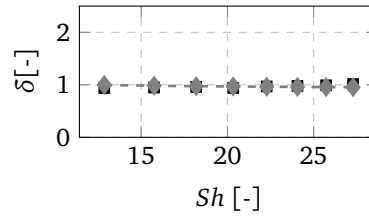
(a) Sample I



(b) Sample II



(c) Sample III



(d) Sample IV

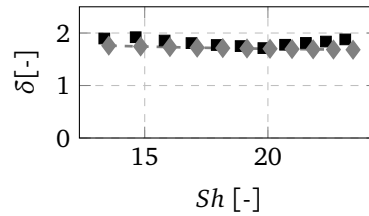


Figure 2.9: Comparison of the resistive and reactive end-correction coefficients of samples with different edge geometries: (■) Experimental, (-♦-) numerical results.

Table 2.2: Factor n for different edge geometries.

Edge Type	n
Square	0
One-Side-Chamfered	1
Both-Sides-Chamfered	2
One-Side-Inverse-Chamfered	-1
Both-Sides-Inverse-Chamfered	-2
Punched	0

perforation geometry of some of the samples are observed, with holes that seem to have a triangular rather than circular shape. It is concluded that, to ensure a high accuracy of the hole geometry and edge shape larger hole diameter and thickness values should be used. As a result, the samples described in Table 2.1 are produced and tested.

Although the open-end impedance measurement is easy to apply, it has a disadvantage where the reflection coefficient value approaches unity (recall $Z_R = \rho_0 c_0 (1 + R_{OE}) / (1 - R_{OE})$). A very small disturbance when $|R| \approx 1$ can lead to large errors on transfer impedance. Thus, in all measurements a large uncertainty above 450 – 500 Hz is observed and therefore results up to $Sh \approx 27$ are presented. It can be concluded from the results in Figure 2.9 that the numerically determined end-correction coefficients are in good agreement with the experimental values for the range of Sh numbers considered. Therefore the numerical model proposed is validated and will be used in the following section to calculate the end-correction coefficients for perforations with different edge profiles.

2.5 Results

After experimental verification, the numerical model is used for broadening the study for $1 < Sh < 35$. Doing so, it is aimed to cover the important Sh number region, $1 < Sh < 10$ for the MPPs according to Maa [6] and extend it to theoretical limits where the end-correction coefficients are comparable with the results from the simulations. This study is divided in three main classes according to the perforation edge profile.

2.5.1 Perforations with square edges

The properties of the numerical cases designed to cover the Sh number range of interest are presented in Table 2.3.

Table 2.3: Properties of the square-edge cases investigated numerically.

	d_p [mm]	t_p [mm]	ϕ
Case 1	0.3	1.0	0.77%
Case 2	0.8	0.4	0.74%
Case 3	0.8	1.0	0.74%
Case 4	0.8	8.0	0.74%
Case 5	1.6	1.6	0.72%
Case 6	4.2	4.0	0.71%

With the use of Eq. (2.8), α and δ are calculated from the simulations for each case. To observe the effect of the thickness of the Stokes layer on these coefficients, the results are presented from all cases in two graphs: α vs. Sh and δ vs. Sh , which can be seen in Figure 2.10.

From Figure 2.10, a strong dependence on Sh is observed for both α and δ . Assuming that Sh is the only parameter defining the end-correction coefficients in sharp-edge perforations, a practical expression for computing α and δ is proposed for $1 < Sh < 35$ and $Sr > 1$ as follows;

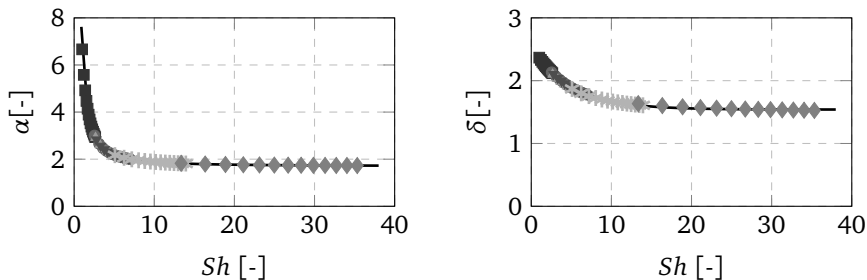
$$\alpha_s = 5.08Sh^{-1.45} + 1.70, \quad (2.9a)$$

$$\delta_s = 0.97 \exp(-0.20Sh) + 1.54, \quad (2.9b)$$

where subscript 's' represents the perforations with the *square edge* geometry.

The expressions given in Eq. (2.9) consists of fit formulas from 411 data points with a quality of $R_\alpha^2 = 0.9995$ and $R_\delta^2 = 0.9960$. The curves calculated using Eq. (2.9) are compared to numerical data in Figure 2.10.

This investigation on square-edge perforations is extended with the non-dimensional plate thickness, $t^* = t_p/d_p$. This time, a surface fit with two independent parameters is performed to include thickness effect in α and δ . The updated expressions with the wall thickness for the end-correction coefficients for the perforations with



(a) Resitive end-correction coefficient.

(b) Reactive end-correction coefficient.

Figure 2.10: End-correction coefficients for square-edge profile plotted as functions of Sh : (\blacksquare) Case 1, (\bullet) Case 2, (\blacktriangle) Case 3, (\blacktriangledown) Case 4, ($*$) Case 5, (\blacklozenge) Case 6, and (—) numerical fit.

square-edge profile become;

$$\alpha_s = 5.08Sh^{-1.45} + 1.70 - 0.002/t^*, \quad (2.10a)$$

$$\delta_s = 0.97 \exp(-0.20Sh) + 1.54 - 0.003/t^*. \quad (2.10b)$$

The new fits given in Eq. (2.10) have a marginally better quality, $R_\alpha^2 = 0.9995$ and $R_\delta^2 = 0.9961$, so it is concluded that α and δ do not significantly depend on t^* for $t^* \geq 0.5$.

2.5.2 Perforations with chamfered edges

The chamfered edge profile is classified in two types depending on if it reduces or increases the effective plate thickness, t_{eff} . The chamfered edge with 45° angle reduces t_{eff} and is defined as *normal* where the one with 135° angle increases t_{eff} and is defined as *inverse* chamfer. Recall that $t_{eff} = t_p - nc_p$ where n can be obtained from Table 2.2. While calculating the theoretical transfer impedance by Crandall [25], effective thickness should be used.

Even though they have different profiles at the perforation edges, the definition of the chamfer length, c_p , and the non-dimensional chamfer length, $c^* = c_p/d_p$, are still the same for both normal and inverted chamfers. The properties of the numerical cases designed for investigating chamfers can be seen in Table 2.4. The limit $c^* = 0$ is the case of square-edge and should be taken into account to relate

the results with the previous part of the study. For this reason, Case 6 is included in both normal and inverse chamfer types.

For this part of the study, 4 different cases are considered. These cases include the smallest and largest non-dimensional chamfer length limits, *i.e.* $c^* = 0$ and $c^* = t^*/2$, respectively. The properties of these numerical cases can be seen in Table 2.4.

Table 2.4: Properties of the chamfered-edge cases investigated numerically.

	d_p [mm]	t_p [mm]	ϕ	c_p [mm]	Type
Case 7	4.2	4.0	0.71%	0.35	Normal
Case 8	4.2	4.0	0.71%	1.0	Normal
Case 9	4.2	4.0	0.71%	2.0	Normal
Case 10	4.2	4.0	0.71%	0.50	Inverse
Case 11	4.2	4.0	0.71%	1.0	Inverse
Case 12	4.2	4.0	0.71%	2.0	Inverse

Including the square-edge geometry in both chamfer types, the simulations provide 244 data points for each coefficient in both types. For perforations with chamfered edges, the best surface representing the distribution of the points for α and δ are in $13 < Sh < 35$ and $Sr > 1$.

$$\alpha_c = 5.08Sh^{-1.45} + 1.70 + 1.18c^{*1.74}Sh^{-0.26}, \quad (2.11a)$$

$$\delta_c = 0.97 \exp(-0.20Sh) + 1.54 + 0.97c^{*0.56} \exp(-0.01Sh), \quad (2.11b)$$

where the subscript 'c' represents the perforations with the *chamfered* edge geometry.

The quality of these fits can be quantified by $R_\alpha^2 = 0.9808$ and $R_\delta^2 = 0.9945$.

The same study on perforations with inverse-chamfered edge profile results with the following α and δ fits in $13 < Sh < 35$ and $Sr > 1$ as;

$$\alpha_{ic} = 5.08Sh^{-1.45} + 1.70 + 0.08c^{*0.17}Sh^{0.36}, \quad (2.12a)$$

$$\delta_{ic} = 0.97 \exp(-0.20Sh) + 1.54 - 0.17c^{*0.41} \exp(0.02Sh), \quad (2.12b)$$

where the subscript 'ic' denotes the *inverse-chamfered* edge geometry.

For these fits, the quality factors are calculated as $R_\alpha^2 = 0.9986$ and $R_\delta^2 = 0.9883$.

2.5.3 Combinations of edge geometries

Neither square nor both-sides-chamfered edge geometries are easy to manufacture in mass production of the MPPs. Hence two example geometries that can be used as practical approximations are considered. These are one-side-chamfered and punched edge profiles, which can be seen in Figure 2.4.

In this part of the study, simulations are run for perforations with smaller diameters to cover lower Sh number region. The properties of the simulated cases are listed in Table 2.5.

Table 2.5: Properties of the numerical cases to verify the proposed fit. Cases C1 to C4 represent one-sided-chamfer edge profile where Cases P1 to P4 represent punched edge profile. $\phi = 0.71\%$ for all cases.

	d_p [mm]	t_p [mm]	c_p [mm]
Case C1	0.3	1.0	0.025
Case C2	0.9	1.0	0.075
Case C3	1.5	1.0	0.125
Case C4	4.2	4.0	0.350
Case P1	4.2	1.0	0.071
Case P2	4.2	1.0	0.214
Case P3	4.2	1.0	0.357
Case P4	4.2	4.0	1.00

One-side-chamfered

This geometry is considered for the cases where the perforations are opened with drills when supported by an additional material from behind. One side of the perforation has the chamfer geometry where the other end has a square profile. Referring to the linearity, the end-corrections can be proposed as a combination of both cases mentioned as

$$\alpha = (\alpha_s + \alpha_c)/2, \quad (2.13a)$$

$$\delta = (\delta_s + \delta_c)/2, \quad (2.13b)$$

where subscripts s and c denote end-corrections for square-edge and chamfered edge profiles respectively, which is calculated from Eqs. (2.9) and (2.11). These

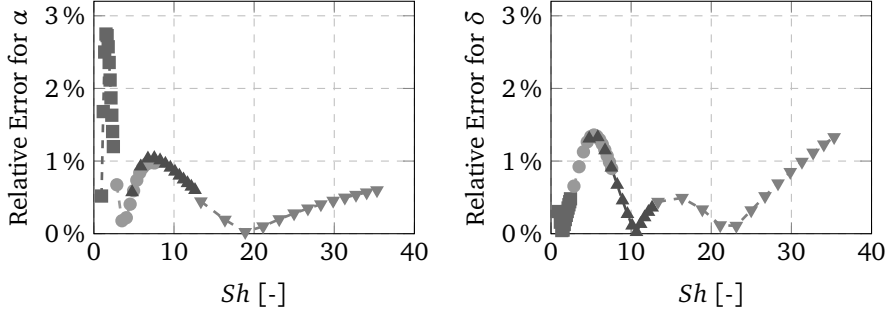


Figure 2.11: The relative percent error of the end-correction coefficients obtained by the proposed fit with respect to the numerical simulations in one-side-chamfered edge profile: (-■-) Case C1, (-●-) Case C2, (-▲-) Case C3, and (-▼-) Case C4.

expressions are assumed to hold for the lower Sh region as well since the governing physics is the same and non-dimensional numbers are used. To check that assumption, $c^* = 0.083$ is selected as in Sample II, and the results are compared of this linear combination with numerical simulations in terms of relative percent error, ϵ_r . For instance, the relative percent error is calculated for α as follows: $\epsilon_r = 100|\alpha_{num} - \alpha_{fit}|/\alpha_{num}$. Replacing α with δ , one obtains the same error definition for the reactive end-correction coefficient. These error plots are provided in Figure 2.11.

Punched hole

The idea behind investigating this geometry for is to approximate the perforations opened by punching the plate. This geometry consists of a chamfered edge and an inverse-chamfered edge profile.

Similar to the one-side-chamfered profile, the end-correction coefficients of this one can be calculated as

$$\alpha = (\alpha_c + \alpha_{ic})/2, \quad (2.14a)$$

$$\delta = (\delta_c + \delta_{ic})/2. \quad (2.14b)$$

where subscript *ic* stands for *inverse-chamfered* and can be calculated using Eq. (2.12). The relative percent error between the numerical results and the proposed fit is shown in Figure 2.12.

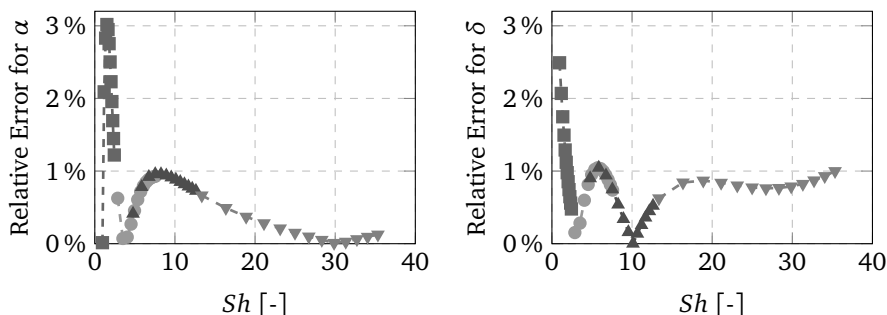


Figure 2.12: The relative percent error of the end-correction coefficients obtained by the proposed fit with respect to the numerical simulations in punched hole geometry: (-■-) Case P1, (-●-) Case P2, (-▲-) Case P3, and (-▼-) Case P4.

Please recall that one-sided-chamfered edge is composed of square-edge and (normal) chamfered edge profiles. Similarly, punched hole geometry is composed of (normal) chamfered edge and inverse edge profiles. Hence, verifying the linear combination of these edge profiles with numerical results is a compact verification of all the fits proposed in this study. From Figures 2.11 and 2.12 it is seen that even for low Sh number region, the fits and the numerical results are in accordance within less than 3% in the Sh number region of interest. Hence, the assumption for the lower Sh number region holds and the proposed fits can be used for calculating end-correction coefficients of MPPs for $Sr > 1$.

2.6 Concluding Remarks

This study proposes expressions for dimensionless end-correction coefficients, α and δ in MPPs based on numerical analysis; whose results are verified by experiments. Using the numerical model described here, different edge profiles such as square, chamfered, inverse-chamfered and their linear combinations are investigated.

The transfer impedance is measured with the open-end method. Yet, when the amplitude of the reflection coefficient of the sample is close to 1, the method becomes prone to errors. For this reason, the measurements with the MPP samples could go up to 450-500 Hz. This corresponds to $Sh \approx 27$ for samples $d_p = 4.2$ mm. If studying with higher Sh is required, one should employ another experiment tech-

nique.

The numerical results show that the plate thickness has negligible effect on the *end-correction coefficients*. It is also concluded that α and δ strongly depend on Sh number and the edge profile. These arguments have been tested in a large variety of non-dimensional thickness range such as $0.5 < t^* < 10$.

Square-edge profile is an important comparison case with the theory. It is reported in the literature [19] that, α can be taken either 2 or 4. The results from this study show that α value can be out of this interval depending on the Shear number. Moreover, with increasing Sh number, an asymptotic approach is observed in end-correction coefficients. These are 1.70 for α and 1.54 for δ . Experiments with the samples also support this statement. Please recall that Ingard [15] proposed α to be 2 empirically; where the result from this study, $\alpha = 1.70$, is close to his. Although Morse and Ingard [35] propose a purely analytical solution for α , it does not show the asymptotic behaviour that one sees in the experiments. On the other hand, both Morse and Ingard [35] and Pierce [36] agree on the theoretical limit for $\delta = 1.57$ in very thin plates. This value is comparable with the findings from the simulations, $\delta = 1.54$.

The chamfered-edge geometry increases α and δ compared to square-edge profile. Yet, the overall transfer impedance value decreases in presence of chamfers. This is due to the fact that the viscous friction is dominant in the narrow part of the perforations, which is defined by t_{eff} in this study, and chamfers reduce this effective plate thickness. On the other hand, inverse-chamfered edges increase t_{eff} , resulting with a higher transfer impedance compared to sharp-edges. In inverse-chamfers, the fluid particles must follow a streamline making a 135° turn. This increase the resistance of the edge but makes it harder for fluid particles to oscillate in and out of the perforation. As a result, compared to sharp-edge geometry, α increases but δ decreases for inverse-chamfered edges.

Since the entire investigation is carried out in linear regime, end-correction coefficients for sharp-edge, chamfered-edge and inverse-chamfered-edge geometries are combined linearly to obtain α and δ for one-side-chamfered edge and punched edge profiles. Although the fit is obtained from data in the region $13 < Sh < 35$, the end-correction coefficients calculated with the proposed expressions are in good agreement with the numerical results even for the region $1 < Sh < 13$. Moreover, the expressions proposed for chamfered profiles are designed to reduce into expressions for square-edge profiles when $c^* = 0$ is selected. Consequently, the expressions offered in this study are generalized and the error between them and the numerical results are less than 3% for $1 < Sh < 35$.

Chapter 3

Non-linear Acoustic Transfer Impedance of Micro-perforated Plates with Circular Orifice¹

Abstract

A practical description of the transitional behaviour of micro-perforated plates (MPPs) is provided between the linear and strongly non-linear regimes. Micro-perforated plates are efficient sound absorbers whose application areas vary from room acoustics to duct acoustics. Although there are accurate models for the linear and strongly non-linear acoustic behaviour of MPPs, the transition from one to another has not been a focus of interest so far. A series of measurements are performed with MPP samples for various excitation amplitudes. The deviation from the linear impedance is found to be a function of excitation amplitude and oscillating viscous boundary layer thickness, expressed in terms of the Strouhal number and the Shear number. Typical for MPPs is a Shear number of order unity, implying that the viscous boundary layer thickness is in the order of the perforation radius. Using the measurement data, expressions are proposed for calculating the non-linear acoustic resistance and reactance for circular perforations with sharp square edges. Some additional data is provided for the higher Shear number range. The behaviour at low amplitudes for high Shear numbers deviates strongly from the typical MPP behaviour. This is due to local vortex forming at the sharp edges of the perforation.

¹The content of this study is published in *Journal of Sound and Vibration* by Temiz *et al.* [37].

3.1 Introduction

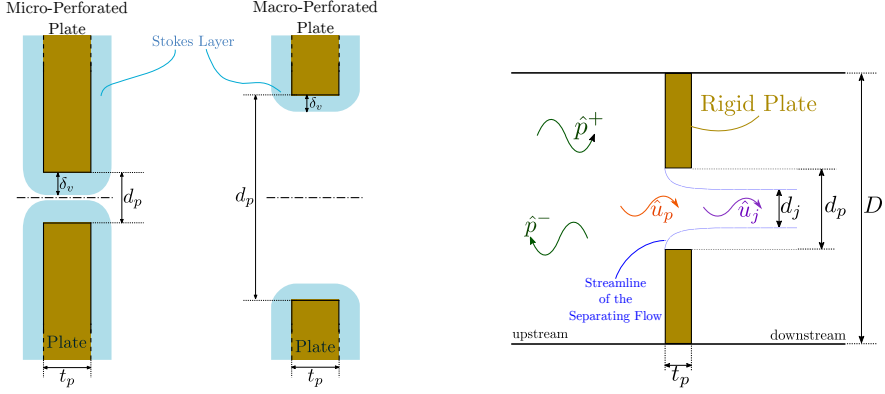
Maa [6] introduced the micro-perforated plates (MPPs) as promising sound absorbers in the presence of a supporting air cavity. MPPs are plates with small perforations whose diameter is in the order of a millimeter and low porosity, *i.e.* $\sim 1\%$. Due to these features MPPs have high acoustic resistance and low reactance. Moreover, they can be produced from any material, so that their durability and weight can be adjusted according to the application. There are a large number of possible application fields such as room acoustics, duct acoustics and thermo-acoustics.

In many practical applications, even in case of moderate intensity of the incident sound, the acoustic particle velocity in the perforations can reach high values [38]. This results in flow separation and vortices at the sharp edges of the perforations. Vortex formation takes energy from the acoustic wave and as a result increases the acoustic resistance of the perforation. Sivian [39] was the first scientist to observe this phenomenon experimentally. Inspired by his findings, Ingard and Labate [17] have performed experiments to conclude that the mechanisms causing extra resistance are flow circulations and these vortices are visualized. Later on, Ingard and Ising [18] have measured quantitatively the non-linear acoustic resistance through an orifice. The orifice used in their experiments had sharp edges. Guess [40] proposes a design method for perforated liners with a backing cavity under high acoustic excitation and subjected to grazing flow. Nevertheless, non-linear effects are included only for the resistance in his method. Later, Disselhorst and van Wijngaarden [41] have measured and described theoretically the amount of dissipated energy due to vortex formation at an open pipe termination and have investigated the influence of rounding off the edges. Cummings and Eversman [42] have improved the quasi-steady model describing the behaviour of perforations at high Shear numbers and very high amplitudes of the acoustic particle velocity. In their model, the acoustic flow separates at the sharp edges and forms a free jet with a cross-section smaller than the perforation area, this is called a *vena-contracta*. Testud *et al.* [43] report that the separated flow reattaches for thick orifices, whose thickness is larger than twice the diameter. Aurégan and Pachebat [44] have studied rigid porous materials both in the moderate and high intensity acoustic amplitudes. One of the most significant observations of this particular study is that in the moderate excitation case the relation between the resistance and the Reynold's number is quadratic. Another contribution to the quasi-steady approach for high amplitude acoustic excitation has been provided by Hofmans *et al.* [45]. Instead of a circular perforation, they have investigated a slit geometry and a method is proposed for obtaining the *vena-contracta* factor as a function of geometry and Mach number of the acoustic jet. Shortly after the study of Hofmans *et al.* [45], Jing and Sun [46]

have proposed an empirical model for the non-linear acoustical behaviour of the in-duct orifices. Their focus has been on very high excitation amplitudes. Leung *et al.* [47] have carried out some numerical experiments with an in-duct orifice with and without flow. They have observed that vortices are shed both upstream and downstream in absence of main flow, but shedding can take place only in the downstream when there is a bias flow present. Buick *et al.* [48] have performed a quite comprehensive study including numerical, analytical and experimental results altogether for explaining the acoustic losses in the open termination of a tube. Although the models do not converge perfectly, all of them result in that there are two separate cases in non-linear acoustic absorption: one case in which vortices are formed locally and remain close to the edges; and the other case in which the vortices are shed far from the orifice. Their observations agree with those of Aurégan and Pachebat [44]. A more practical study has been carried out by Park [11]. A design method for MPPs is proposed including the non-linear effects for the impedance. The non-linear resistance term is updated in this study, however for the reactance, an expression from early works of Maa [38] is used. Ji and Zhao [49] have applied the Lattice Boltzmann Method for modelling the non-linear acoustic losses of an in-duct orifice. They have successfully reproduced the experimental results of Jing and Sun [46] and their method promises a less expensive computation compared to classical Navier-Stokes solvers. Nevertheless, none of these studies address MPPs directly. Also, they mainly focus on the regime where strong non-linear effects are observed.

This study focuses on non-linear acoustic behaviour of MPPs with circular orifices with sharp square edges (90° angle). Besides, it is extended to plates with perforations whose diameters are larger than those of MPPs. In this way, the results are linked with previous studies on orifices whose diameter is larger than the MPP range. Furthermore, the scope of this study is limited to the transition between linear and non-linear regimes, to bridge the gap between these two regimes. Moreover, both the non-linear acoustic resistance and reactance are investigated.

The results in this study are obtained from open-end transfer impedance measurements. The dimensions of the samples used in these measurements cover both the typical MPP range and slightly beyond. Practical formulas are proposed to form a bridge between linear and non-linear regimes in MPPs. These formulas are expressed in terms of dimensionless parameters, introduced in the next section.



(a) Difference between micro and macro-perforated plates.

(b) Quasi-steady flow under the influence of high level acoustic excitation.

Figure 3.1: Orifice geometry (a) and the quasi-steady acoustic flow (b) with orifice diameter d , plate thickness t , channel diameter D , Stokes layer thickness δ_v , (complex) acoustic pressure \hat{p} and (complex) acoustic particle velocity \hat{u} where the subscripts p and j imply *perforation* and *jet flow* respectively.

3.2 Theoretical Background

In the linear regime the absorption of the acoustic energy takes place in the Stokes layers shown in Figure 3.1a. These layers form due to the presence of the solid-walled plate [50]. The thickness of the oscillating Stokes layer is $\delta_v = \sqrt{\mu/\omega\rho_0}$ where $\omega = 2\pi f$ is the angular frequency, ρ_0 is the density of air (1.18 kg/m^3 @25°C, 1 atm, dry air) and μ is the dynamic viscosity of air ($1.85 \times 10^{-5} \text{ kg/ms}$ @25°C).

The Stokes layer thickness relative to the perforation diameter d_p is the main parameter that defines a micro-perforated plate (MPP) and is referred to as the *Shear number*,

$$Sh = \frac{d_p}{2\delta_v} = d_p \sqrt{\frac{\omega\rho_0}{4\mu}}. \quad (3.1)$$

In an MPP the Stokes layers cover almost completely the perforation, *i.e.* $Sh = \mathcal{O}(1)$. For low enough excitation amplitudes, the linear transfer impedance of an MPP is calculated as a function of perforation geometry and frequency only [24].

When the excitation amplitude is larger than a critical value, vortices start forming at the sharp corners of the perforation [18]. This is schematically shown in Figure 3.1b. The formation of vortices is a non-linear mechanism. This takes up energy from the acoustic waves resulting in additional absorption. The criterion for these vortices to start forming is based on the *Strouhal number*, which is calculated as

$$Sr = \frac{\omega d_p}{|\hat{u}_p|}, \quad (3.2)$$

where $|\hat{u}_p|$ is the cross-sectional surface averaged acoustic velocity amplitude at the orifice.

For $Sr \gg 1$, the particle displacement is smaller than the orifice diameter and vortices are unlikely to be observed. In other words, the acoustic system is linear. In the opposite limit, $Sr \ll 1$, the particle displacement in the vicinity of the orifice is so large that vortices are blown away by the acoustic flow, which can be described as a free jet. In between these two limiting cases, *i.e.* $Sr = \mathcal{O}(1)$, vortices form at the edges of the perforations but they remain local. In this study, to focus on the transition regime, range $0.05 < Sr < 10$ is investigated only. The limit cases are now discussed in more detail.

3.2.1 Strongly non-linear regime: $Sr \ll 1$

If the particle displacement is much larger than the orifice diameter, *i.e.* $Sr \ll 1$, the non-linear resistance due to vortex shedding dominates the absorption mechanism as shown by Ingard and Ising [18]. Assuming that the acoustic pressure is negligible on the downstream side of the orifice, the pressure amplitude on the upstream is expressed by

$$|\hat{p}_{up}| = \rho_0 |\hat{u}_p|^2, \quad (3.3)$$

according to Ingard and Ising's experiments [18], where \hat{p}_{up} is the complex pressure amplitude at the upstream of the orifice. Note that the derivation of this formula by Ingard and Ising [18] is not correct.

Cummings and Eversman [42], propose a simple theoretical approach to represent the acoustic flow through the orifice in a duct in the high Sh number limit. They assume a quasi-steady behaviour in which the relation between the pressure change and the particle velocity can be derived from the Bernoulli equation. They find:

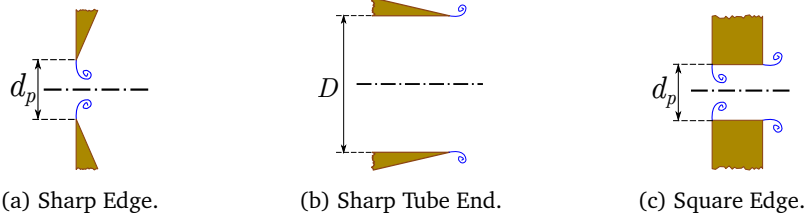


Figure 3.2: Edge profiles described in (a) Ingard and Ising's [18], (b) Disselhorst and van Wijngaarden's [41] and (c) current study.

$$|\hat{p}_{up}| \simeq \rho_0 |\hat{u}_p|^2 \frac{1 - \sigma^2 C_v^2}{2C_v^2}, \quad (3.4)$$

where σ is the porosity and C_v is the vena-contracta factor. Considering the typical properties of MPPs, the term $\sigma^2 C_v^2$ can be neglected due to low values of σ .

Bearing in mind that Ingard and Ising [18] used an orifice with a sharp-edge profile, both of the expressions given earlier in this section (Eqs. (3.3) and (3.4)) are in practice equivalent because the vena-contracta factor for sharp edges (see Figure 3.2) is $C_v \simeq 0.7$. Yet, the model by Cummings and Eversman [42] takes other types of edge profiles into account as well, because another value of *vena-contracta* can be used.

3.2.2 Almost linear regime: $Sr > 1$

Disselhorst and van Wijngaarden [41] give the power absorbed by vortices, \bar{P} , in the high Sr limit as

$$\bar{P} = \alpha \left[\rho_0 \pi \left(\frac{D}{2} \right)^2 |\hat{u}_D|^3 / 2 \right] \frac{Sr^{1/3}}{\sqrt[3]{2}}, \quad (3.5)$$

for an open tube termination. In Eq. (3.5), α is a constant changing between 0.6 and 1.0 depending on the number of point vortices used to describe the flow [16] and \hat{u}_D is the acoustic particle velocity amplitude at the tube termination. Written in terms of acoustic pressure amplitude, Eq. (3.5) takes the following form:

$$|\hat{p}_{up}| = 2\alpha \rho_0 |\hat{u}_D|^2 \frac{Sr^{1/3}}{\sqrt[3]{2}}. \quad (3.6)$$

According to Disslehorst and van Wijngaarden [41] the higher Sr gets, the larger normalized non-linear resistance becomes. Yet it should be noted that this model is based on a high Sh limit and does not apply to MPPs for which $Sh = \mathcal{O}(1)$.

3.2.3 Transition regime: $Sr = \mathcal{O}(1)$

The study of Aurégan and Pachebat [44] focuses on acoustic resistance in porous materials. They quantify the non-linearity in the results with Reynolds number instead of Strouhal number, which is defined as $Re = D|\hat{u}_p|\rho_0/\mu$. Their main result is that for $Re \ll 1$, the non-linear correction to Darcy's law takes the following form:

$$R_{NL} = R_L(1 + C_2 Re^2), \quad (3.7)$$

where $R = \Re\{Z_t\}$ is the acoustic resistance and C_2 is a constant defined empirically. By Eq. (3.7), one concludes that the non-linear resistance in the transition regime must be quadratically related to the particle velocity in the low Sh number limit valid for MPPs.

3.3 Experiments

3.3.1 Properties of the setup

The experimental set-up used in this study is an impedance tube with 6 pre-polarized 1/4in microphones (type BWSA, sensitivity 50 mV/Pa). The schematic description of the set-up, including the dimensions of the tube and positions of the microphones, is shown in Figure 3.3.

The measurements have been conducted in a semi-anechoic room to avoid problems related to room resonances. The air in the tube is excited by a 3.5 in, 25 W loudspeaker. The microphone closest to the tube termination is calibrated by a B & K piston-phone at 1000 Hz for 1 Pa. The relative calibration of the remaining microphones with respect to the first one is performed using an apparatus, which is displayed in Figure 3.4 specially designed for this purpose. Using the apparatus, the response of the 6 microphones are measured simultaneously to an identical pressure fluctuation. For each frequency step, the pressure amplitude and the phase of each microphone are adjusted to the reference microphone's by means of a calibration factor.

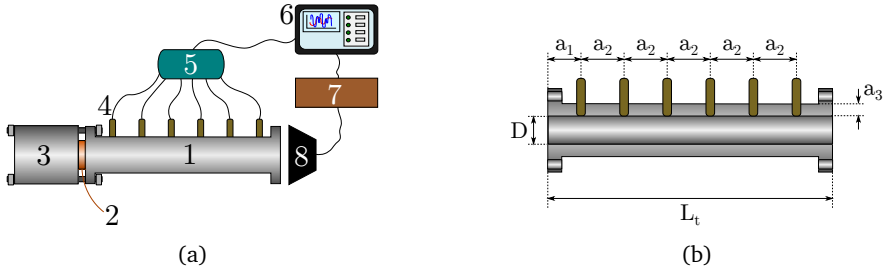


Figure 3.3: Impedance tube used in the measurements: (a) schematic drawing of the components which are: (1) the tube, (2) the sample, (3) (hollow) sample holder, (4) microphones, (5) microphone amplifier, (6) analyser and computer, (7) loudspeaker amplifier and (8) loudspeaker; (b) dimensions of the tube: $a_1 = 50$ mm, $a_2 = 175$ mm, $a_3 = 10$ mm, $D = 50$ mm and $L_t = 1$ m.

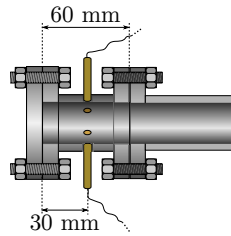


Figure 3.4: Placement of the microphones for the relative calibration process. All the microphones are located axially at the same distance from the loudspeaker and the closed tube termination.

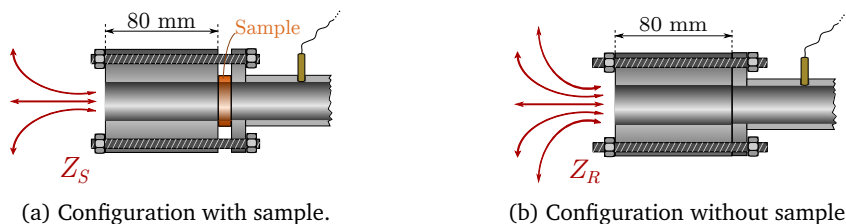


Figure 3.5: Open-end impedance tube measurements are performed in 2 steps. First, the impedance values for the sample loaded (a), then the open-end (b) configurations are measured. The transfer impedance of the sample is calculated from these values by $Z_t = Z_S - Z_R$.

3.3.2 Properties of the DAQ system

For data acquisition, an *NI PCIe-6361 X-Series* DAQ card with 16 analog input and 2 analog output channels is used. A script built in *NI LabView*[®] software controls the signal processing and data acquisition during the measurements. The post-processing of the microphone readings is done separately in a user-built Matlab script with a *Lock-in* method [31]. The sampling rate is 20 kHz for the excitation signal and 10 kHz for recording the input signal. Each frequency step is measured for 10 seconds. To avoid transient effects in the measurements, the first and last 2 seconds are omitted in the post-processing. The amplitude of the excitation signal is adjusted automatically until it satisfies the pre-determined pressure value for the reference microphone, *i.e.* the microphone closest to the sample.

3.3.3 Measurement method

The idea behind the open-end transfer impedance measurement is displayed in Figure 3.5. Since the samples have relatively low porosity, *i.e.* $\sigma = \mathcal{O}(1\%)$, the open-end radiation impedance (see Figure 3.5b) is expected to be negligible compared to the impedance measured for the sample loaded termination (see Figure 3.5a). Nevertheless, to take open end radiation effects into account, the acoustic transfer impedance of a sample is calculated as $Z_t = Z_S - Z_R$, where Z_S is the impedance for the loaded case and Z_R is the measured open-end radiation impedance.

To measure the impedance, the relation between the reflection coefficient, ζ , and the impedance, Z is used [32]. Based on this relation, the impedance in each measurement is calculated as $Z = \rho_0 c_0 (1 + \zeta) / (1 - \zeta)$. Then the measured radiation

impedance Z_R is subtracted from the sample loaded end termination impedance Z_S to find the transfer impedance, $Z_t = Z_S - Z_R$.

The calculation of ζ is performed by the wave decomposition described by Jang and Ih [32]. In our study, this method is improved by employing the complex wave number approximation of Peters *et al.* [29].

In this study, the measurements and the calibration are performed for $60 \text{ Hz} < f < 240 \text{ Hz}$. The frequency step is 20 Hz and multiples of the grid frequency, *i.e.* 100 Hz and 200 Hz, are excluded from the calculations for the sake of reliability. The deviation from the theoretical limit is less than 0.5% for the closed-end reflection coefficient measurements in the frequency span of interest.

During the experiments, 6 sets of measurements are performed for each sample: 1 set in the linear and 5 sets in the non-linear regime. To make sure the measurement set with the lowest excitation amplitude is in the linear regime, an empirical method is followed. Measurements start with an arbitrary excitation amplitude and the resulting reflection coefficient is recorded for the lowest frequency of interest. As non-linear effects decrease with increasing frequency [47], the amplitude is gradually reduced until two successive measurements give the same (or very close) reflection coefficient value. For this amplitude value, the linear transfer impedance Z_{t-L} is calculated from the reflection coefficient throughout the frequency span of interest. Next, the amplitude is doubled and the non-linear transfer impedance values Z_{t-NL} in the frequency span are recorded. Finally, this last step is repeated until the 6 sets are completed.

3.3.4 Measuring $|\hat{u}_p|$

The required acoustic particle velocity amplitude to calculate Sr at a specific frequency and excitation amplitude is deduced from the pressure amplitude in the tube.

The wave decomposition provides the amplitudes of right and left travelling pressure waves, \hat{p}^+ and \hat{p}^- respectively (see Figure 3.1b). By Euler's law, the relation between the amplitudes of the pressure waves and the particle velocity is given by

$$\hat{u}_D = \frac{\hat{p}^+ \exp(jk^+x) - \hat{p}^- \exp(jk^-x)}{\rho_0 c_0}, \quad (3.8)$$

where \hat{u}_D is the particle velocity in the tube, $j = \sqrt{-1}$ is the imaginary number, x is the distance from the reference plane, k is the complex wave number and

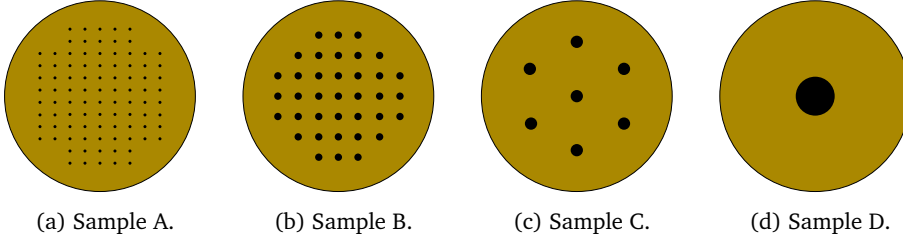


Figure 3.6: Schematic drawings of samples used. Samples A, B and C have multiple orifices where Sample D has a single orifice. All of the orifices are assumed to have square edge profiles.

superscripts ‘+’ and ‘-’ indicate the right and left travelling waves respectively. In case of no mean flow $k = k^+ = k^-$, and is approximated by Peters *et al.* [29] as

$$k = \frac{\omega}{c_0} \left[1 + \frac{1-j}{\sqrt{2}} \frac{1}{Sh_D} \left(1 + \frac{\gamma-1}{Pr^{0.5}} \right) \right] - \frac{\omega}{c_0} \frac{j}{Sh_D^2} \left(1 + \frac{\gamma-1}{Pr^{0.5}} - \frac{1}{2} \gamma \frac{\gamma-1}{Pr} \right), \quad (3.9)$$

where γ and Pr are respectively the ratio of the specific heats and Prandtl number for air, and Sh_D is the ratio of the tube diameter to the Stokes layer thickness. Since the calculation is performed just before the sample in the upstream region, $x = 0^-$ is valid. Considering continuity, one calculates the acoustic particle velocity in the perforation as

$$|\hat{u}_p| = \frac{|\hat{p}^+ - \hat{p}^-|}{\rho_0 c_0 \sigma}. \quad (3.10)$$

3.3.5 Specifications of the samples

Throughout this study we have used 4 samples with different diameters and comparable porosity values. Schematic drawings of these samples are given in Figure 3.6 and their specifications are provided in Table 3.1.

The *vena-contracta* coefficient C_v given in Table 3.1 depends on both orifice edge profile and Reynolds number [51]. Considering the samples used in this study, the Reynolds number of the acoustic flow in the perforation is $Re_p = |\hat{u}_p| d_p \rho_0 / \mu$ and for this set of measurements $Re_p = \mathcal{O}(10)$.

All of the samples are made of brass by drilling. The outer diameter of the samples is 70 mm. To ensure that there is no air leakage between the samples and

Table 3.1: Specifications of the samples.

Sample	d_p [mm]	t_p [mm]	σ	C_v
Sample A	0.3	1.0	0.77%	0.70
Sample B	0.8	1.6	0.74%	0.70
Sample C	1.6	1.6	0.72%	0.70
Sample D	4.2	4.0	0.71%	0.70

the impedance tube o-rings are used for mounting the samples.

3.4 Results and Discussions

Since the non-linear effects are interested in this study, the linear contribution is subtracted from the non-linear resistance and reactance that are measured in the tube just before the sample. To calculate a single perforation, this quantity is multiplied with the porosity, σ . Furthermore, the change in resistance is normalized with the non-linear limit proposed by Ingard and Ising [18] where for reactance it is normalized by the fluctuating mass term proposed by Ingard [15]. By these normalizations, one obtains non-dimensional resistance and reactance changes due to non-linearity, ΔR_{NL} and $\Delta \delta_{NL}$ respectively. These parameters are given in Eqs. (3.11a) and (3.11b).

$$\Delta R_{NL} = \frac{(\Re\{Z_{t-NL}\} - \Re\{Z_{t-L}\})\sigma}{|\hat{u}_p|\rho_0}, \quad (3.11a)$$

$$\Delta \delta_{NL} = \frac{(\Im\{Z_{t-NL}\} - \Im\{Z_{t-L}\})\sigma}{\omega\rho_0 d_p/2}. \quad (3.11b)$$

Recall that, the resistance expression by Ingard and Ising [18] is only valid for orifices with sharp edge profiles. For a universal non-dimensional parameter, the effect of the orifice edge should corrected via Eq. (3.4) as,

$$\Delta R_{NL-C} = 2C_v^2 \Delta R_{NL}. \quad (3.12)$$

The plots of ΔR_{NL-C} and $\Delta \delta_{NL}$ are provided as functions of Sr in Figures 3.7 to 3.9. In these graphs, for each Sh value, there is a separate curve (symbol).

In Figure 3.7, it is seen that for $Sh = \mathcal{O}(1)$, the effect of Shear number cannot be ignored both for ΔR_{NL-C} and $\Delta \delta_{NL}$. Nevertheless, as the Shear number increases

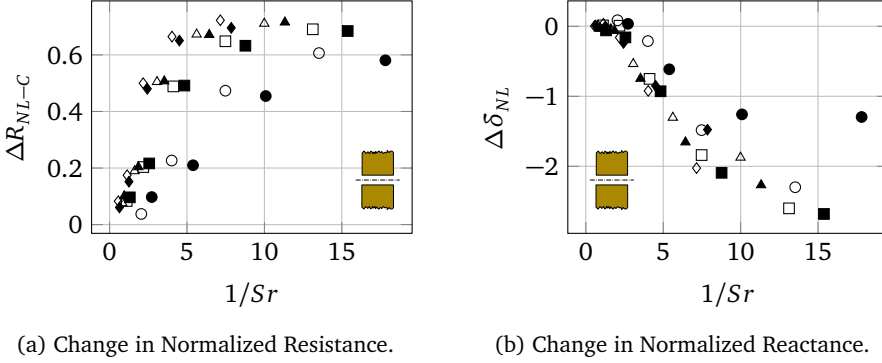


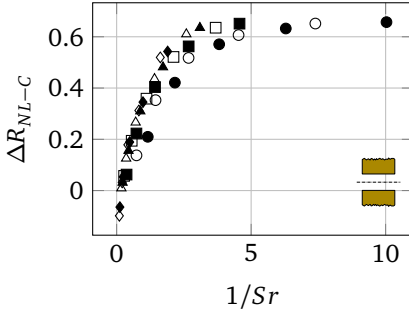
Figure 3.7: The effect of Sh number for Sample A: \bullet $Sh = 0.75$, \circ $Sh = 0.86$, \blacksquare $Sh = 1.05$, \square $Sh = 1.14$, \blacktriangle $Sh = 1.22$, \triangle $Sh = 1.29$, \blacklozenge $Sh = 1.43$, \diamond $Sh = 1.49$.

this dependence vanishes rapidly both for the resistance and reactance change due to non-linearity in MPPs. Moreover, in the resistance case, ΔR_{NL-C} approaches an asymptote which is determined by C_v . It is seen that for high Strouhal and low Shear numbers ($Sr \gg 1$, $Sh = \mathcal{O}(1)$), the non-linear normalized resistance is proportional to the inverse of the Strouhal number (Figure 3.7). Hence the non-linear contribution to the resistance is proportional to the square of the acoustic amplitude (and Reynolds number) as predicted by Aurégan and Pachebat [44].

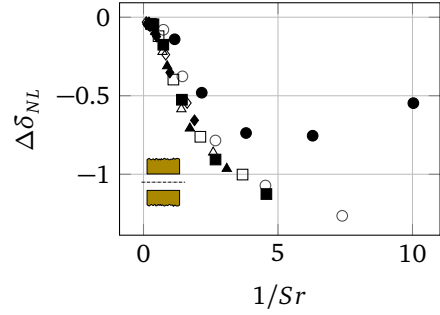
On the other hand, deriving conclusion on the reactance is not as straightforward as the resistance case. One observes that δ_{NL} approaches 0 for high the Sr limit regardless of the Sh value, as expected from the definition given in Eq. (3.11b). Yet, for the low Sr limit, no clear trend is observed for the interval of Sr where the measurements are performed. For example, in Figure 3.7b, the case $Sh = 0.75$, $\Delta\delta_{NL}$ has a tendency of having a plateau; yet this behaviour cannot be easily generalized by looking at other Sh number cases.

The distributions of ΔR_{NL-C} and $\Delta\delta_{NL}$ in Figures 3.8 and 3.9 agree with the previous observations for Sample A in Figure 3.7. As the Shear number increases, the deviation between the measurement points becomes smaller for both the normalized resistance and reactance.

Based on the measurement data presented in Figures 3.7–3.9, fits are proposed as functions of Sr and Sh . The fits representing the change in normalized resistance and reactance are given as F_C and G_C , respectively.

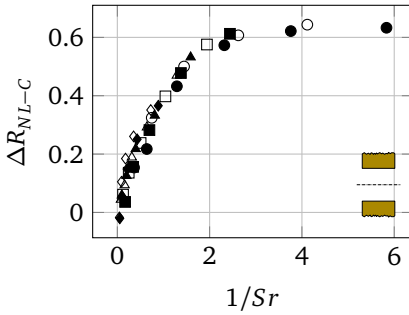


(a) Change in Normalized Resistance.

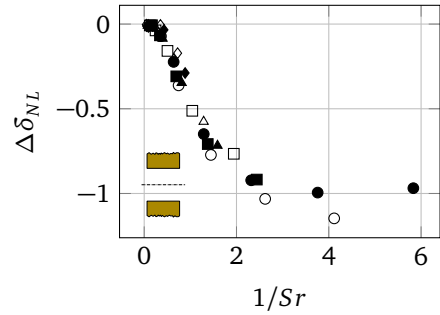


(b) Change in Normalized Reactance.

Figure 3.8: The effect of Sh number for Sample B: \bullet $Sh = 1.99$, \circ $Sh = 2.29$, \blacksquare $Sh = 2.81$, \square $Sh = 3.04$, \blacktriangle $Sh = 3.25$, \triangle $Sh = 3.44$, \blacklozenge $Sh = 3.81$, \diamond $Sh = 3.98$.



(a) Change in Normalized Resistance.



(b) Change in Normalized Reactance.

Figure 3.9: The effect of Sh number for Sample C: \bullet $Sh = 3.98$, \circ $Sh = 4.59$, \blacksquare $Sh = 5.62$, \square $Sh = 6.07$, \blacktriangle $Sh = 6.49$, \triangle $Sh = 6.88$, \blacklozenge $Sh = 7.61$, \diamond $Sh = 3.98$.

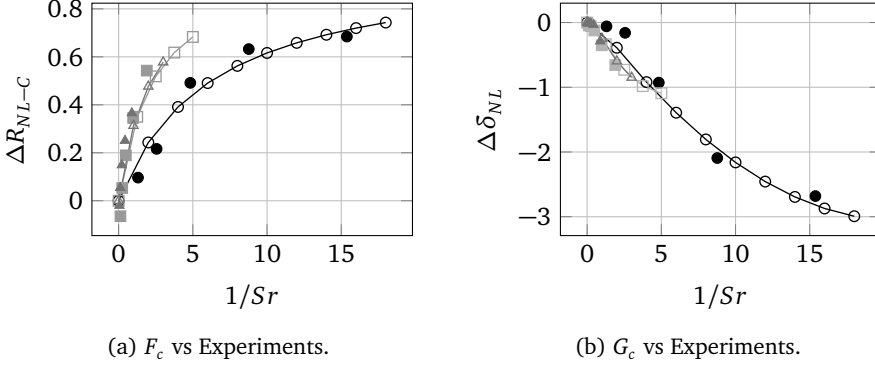


Figure 3.10: Comparison of the proposed expressions F_c and G_c with experiment results. In sake of simplicity, one Sh value is chosen from Samples A, B and C as examples: \bullet $Sh = 1.05$ (Exp), \circ $Sh = 1.05$ (Fit); \blacksquare $Sh = 3.81$ (Exp), \square $Sh = 3.81$ (Fit); \blacktriangle $Sh = 7.61$ (Exp), \triangle $Sh = 7.61$ (Fit).

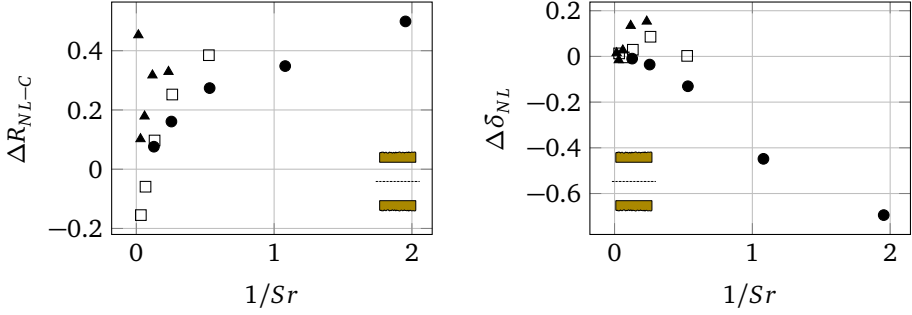
$$F_c(Sr, Sh) = \frac{1}{1 + 2Sr[1 + 0.06 \exp(3.74/Sh)]}. \quad (3.13)$$

$$G_c(Sr, Sh) = \begin{cases} 0.20 - \frac{0.50}{Sr} \left(1 - \frac{0.42}{Sh^2}\right) + \frac{0.05}{Sr^2} \left(1 - \frac{0.68}{Sh^2}\right), & \text{if } Sr \leq 1. \\ -0.05 \left[\frac{1}{Sr} \left(1 - \frac{1}{Sh}\right)\right] - 0.60 \left[\frac{1}{Sr} \left(1 - \frac{1}{Sh}\right)\right]^2, & \text{otherwise.} \end{cases} \quad (3.14)$$

The expressions in Eqs. (3.13) and (3.14) are obtained by curve fitting of the experimental data. For these fits, 118 data points were used. The correlation coefficients r_F and r_G for F_c and G_c are given as $r_F^2 = 0.92$ and $r_G^2 = 0.85$ respectively.

The comparison between the proposed expressions and the experimental data is given in Figure 3.10. In this figure, to maintain simplicity, 3 Shear number cases are selected. These cases are chosen in such a way that experimental data with low ($Sh = 1.05$), medium ($Sh = 3.81$) and high ($Sh = 7.61$) values for the Shear number are compared with the proposed expressions. As it is seen in Figure 3.10, the proposed expressions represent the Sr and Sh number dependence in the transition regime.

As shown in Figure 3.10, the proposed expressions represent the general behaviour of the measurements well in the transition regime. With these expressions, one can calculate the non-linear resistance and reactance as



(a) Change in Normalized Resistance.

(b) Change in Normalized Reactance.

Figure 3.11: The effect of Sh for Sample D. As the shear layer gets thin, different non-linear mechanisms are activated: ● $Sh = 10.4$, □ $Sh = 14.8$ and ▲ $Sh = 18.1$.

$$\Re\{Z_{t-NL}\} = \Re\{Z_{t-L}\} + \frac{F_c(Sr, Sh)|\hat{u}_p|\rho_0}{2C_v^2\sigma}, \quad (3.15a)$$

$$\Im\{Z_{t-NL}\} = \Im\{Z_{t-L}\} + \frac{G_c(Sr, Sh)\omega\rho_0d_p}{2\sigma}. \quad (3.15b)$$

For the resistance, as Sr increases, the dependence between the dimensionless ΔR_{NL-C} and acoustic particle velocity amplitude becomes almost linear according to the proposed expression in Eq. 3.13. This behaviour corresponds to the prediction for porous media by Aurégan and Pachebat [44].

Although it is not in the focus of this study, some experiments have been carried out with orifices which have considerably larger diameters than typical MPPs ($Sh \gg 1$). For example with Sample D, some peculiar behaviour is observed both for the resistance and the reactance. The measurement results for this sample with three different Sh levels are given in Figure 3.11.

For Sample D, when the Stokes layer is thin compared to the diameter of the orifice, the resistance increases as Sr becomes very large. Considering the results from Disselthorst and van Wijgaarden [41] and Peters and Hirschberg [16], similar behaviour has been observed with tube terminations with sharp edges. An increase following $Sr^{1/3}$ is expected for the normalized non-linear contribution to the resistance, following Eq. (3.6). Yet, further research and measurements are required to support this explanation.

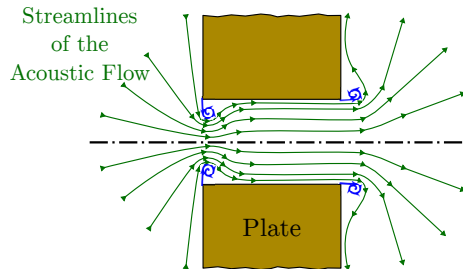


Figure 3.12: Sketch of the acoustic flow with flow separation at sharp edges and reattachment.

Furthermore, an overshoot to positive values is observed in Figure 3.11b for the non-linear contribution to the inertia. As the Shear number increases, the overshoot becomes stronger. This corresponds to the weak non-linear behaviour reported by Ingard and Labate [17]. At such amplitudes, vortices are formed at the edges of the orifice, but they remain close to the edge. The formation of a jet flow is not reached there. The flow separates from the orifice edges, but reattachment of this flow occurs soon downstream. The reattachment of the flow also occurs for relatively thin orifices [17]. The schematic description of reattachment is illustrated in Figure 3.12.

The local contraction of the acoustic flow due to vortex formation occurs at the upstream edge. This corresponds to a local increase of flow velocity due to the contraction of the flow. Further increase of the inertia is due to the increased effective length of the perforation caused by the vortex shedding at the downstream edge of the perforation.

In case of Sample A, some slightly positive valued data points are observed for the high Str limit. Yet, for this sample, the Stokes layer thickness is comparable with the orifice radius which could be a reason for the suppression of the overshoot.

3.5 Conclusions

This study focuses on the acoustic response of micro-perforated plates (MPPs) with circular orifices and square edges in the linear to non-linear transition regime. In this regime, the deviation from the linear resistance and reactance due to the increase in the excitation amplitude is interested in. To measure this, an impedance tube set-up is used. Dimensionless functions of Strouhal (Str) and Shear (Sh) num-

bers are proposed both for non-linear resistance and reactance, *i.e.* F_c and G_c respectively.

The non-linear effects are initiated around $Sr = \mathcal{O}(1)$. In this investigation, to see the transition from linear to non-linear regimes, the excitation amplitude is varied for Strouhal number values $Sr \in [0.05, 10]$. Furthermore, to meet the typical micro-perforated plate range and to observe the perforations slightly larger than this range Shear number values are limited to within the range $0.75 < Sh < 8$.

The most prominent result of the study is that in the transition regime, the non-linear corrections both for resistance and reactance depend mainly on Sr and Sh for MPPs. The dependence on Sh is significant for $Sh = \mathcal{O}(1)$, and becomes negligible for higher values of $Sh > 3$.

The non-linear correction for the resistance, F_c , is selected in such a manner that it vanishes for $Sr \gg 1$ and approaches to an asymptote defined by C_v for $Sr \ll 1$. In other words, F_c satisfies the limits for both the linear and quasi-steady approach. Moreover, in the transition regime, the relation between the resistance and the particle velocity is quadratic according to F_c . This is in agreement with previous analytical models [44, 52, 53]. For higher Shear numbers and $Sr \gg 1$, a more complex behaviour is observed which has been described by Disselhorst and van Wijngaarden [41].

The proposed non-linear correction function for the inertia G_c also vanishes for $Sr \gg 1$. Yet, for the $Sr \ll 1$, it does not have a limit. The inertance is negligible in the limit $Sr \ll 1$. Moreover, especially for high Sh and high Sr cases, an overshoot to positive values is observed for the non-linear correction for the inertia. The mechanism responsible for this is suspected to be the local vortex shedding as described by Ingard and Labate [17]. This results in a local increase in flow velocity and correspondingly of inertia.

With the correction functions proposed, a link between the linear and non-linear acoustic behaviour for MPPs is provided for practical applications.

Chapter 4

Effect of Orifice Edge Profile on Non-linear Acoustic Response

Abstract

This study investigates the effect of edge profiles on the acoustic response of orifices subjected to high-amplitude excitation. Due to the ease in its manufacturing process, an orifice is one of the most widely utilized sound control elements in acoustic engineering. However, each manufacturing technique produces its own edge profile. The current study leans over the effect of various edge profiles on the non-linear acoustic response of an orifice. To focus only on the difference on edge profiles, 7 single-orifice samples are tested in an impedance tube set-up at various excitation levels. It is found that chamfering reduces the non-linear transfer resistance by 50% in comparison to sharp edges in the transition regime, where the particle displacements are comparable to the orifice diameter. Moreover, the measurement results are compared to a quasi-steady approach in terms of reflection coefficient and sound generation in higher harmonics. The quasi-steady approach is revealed to be accurate for strongly non-linear regime, *i.e.* for acoustic particle displacements in the orifice much larger than the orifice plate thickness. However it severely underestimates the reflection coefficient of an orifice close to an open-end for excitation levels corresponding to the transition regime.

4.1 Introduction

Using orifices (perforations) to control the acoustic properties of a wall is a common practice in engineering. They are also used for sound absorption in resonators [15] or for sound generation in (woodwind) musical instruments [54]. In other words, plates with orifices have a wide range of acoustic applications that can involve high-amplitude sound waves.

There are various techniques to produce plates with orifices such as drilling, laser cutting, punching, etc. Each technique results in a different edge-profile. Even for cases with low-amplitude excitations, it is known that the edge-profile alters the acoustic response of an orifice plate [24]. Thus, the effect of orifice edge-profile in high-amplitude applications should be known for better design. There are some remarkable studies related to this problem in the literature.

Sivian [39] is one of the pioneer scientists to study the acoustic impedance of the orifices. In his experiments, Sivian [39] discovers an increase in the resistance with increasing excitation amplitude. The revelation of this non-linear phenomenon inspires Ingard and Labate [17] to carry out experiments where the acoustic flow around a thin orifice is visualized. In their measurements with high-amplitude excitations, they observe that the additional resistance results from acoustic flow separation at the sharp edges of the orifice. When the amplitude is increased further, it is also seen that the vortices are detached from the edges and carried away by the acoustic flow. An oscillating jet is formed at both sides of the orifice. Bies and Wilson [55] have studied the non-linear acoustic response of a Helmholtz resonator experimentally and found that the reactance decreases with the increasing excitation amplitude. They explain this phenomenon by the conversion of alternating flow to turbulent flow. Ingard and Ising [18] have used a hot-wire technique to measure the particle velocity in the acoustic jet through the orifice and observe that the non-linear resistance is proportional to the particle velocity. They propose a quasi-steady model for computing the non-linear resistance of an orifice, however this model does not include the effect of area contraction in jet forming. Melling [56] and Cummings and Eversman [42] improve the quasi-steady model by introducing the *vena-contracta* factor into the non-linear resistance expression proposed by Ingard and Ising [18]. Cummings [57] has shown that the quasi-steady approach can be used for estimating the sound generation in higher harmonics. An application of the quasi-steady approach is reported by Hirschberg *et al.* [58] to explain the sound generation in clarinet. Recently, Temiz *et al.* [37] carry out measurements on orifices with sharp square-edge profile in the transition regime and propose expressions to link linear and non-linear regimes.

The edge profile of the orifice is not the primary focus in the studies mentioned

so far. However, its effect on the non-linear acoustic response is not completely ignored. Thurston [59] has measured the higher harmonics of orifices with various edge profiles and reports the emergence of even harmonics in case of an asymmetric orifice. Working on musical instruments, Keefe [54] concludes that the sound quality of a woodwind instrument can be enhanced by minimizing the non-linear effects at the inner-side of a tone-hole. McDonald [60] proposes that the reduction of non-linear effects can be achieved by undercutting the edges of the tone-holes. Förner *et al.* [61] have studied the effect of chamfering the edges on the reflection characteristics of a Helmholtz resonator under high-amplitude excitation. In this study they compare experimental results with a numerical model. Using the same numerical model in another study, Förner *et al.* [62] has investigated sound generation in the higher harmonics and compare their results with the quasi-steady approach.

Non-linear response of orifices with an asymmetric profile is used as jet pumps to avoid steady flow in thermoacoustic devices. A detailed study of the flow in such orifice pumps is provided by Oosterhuis *et al.* [63].

In this study, the effect of orifice edge profile on the non-linear acoustic response is investigated. Firstly, 7 samples with equal plate thickness (t_p), orifice diameter (d_p) and porosity (ϕ) values are chosen. The thickness of the plate is chosen to be comparable to the orifice diameter, *i.e.* $t_p/d_p \sim \mathcal{O}(1)$. These samples are placed in an impedance tube set-up to perform open-end transfer impedance measurements, described in detail by Temiz *et al.* [37]. The reflection coefficient values of each sample are estimated using the quasi-steady approach and compared to the measured ones. Finally, the sound generation at higher harmonics for a selection of samples is calculated using the quasi-steady approach and compared to the measurements.

4.2 Theoretical Background

The acoustic field is assumed to be dominated by a fundamental harmonic $\omega = 2\pi f$, where f is the excitation frequency. Besides, the measure for the acoustic non-linearity of an orifice is provided by the *Strouhal number* Sr defined as

$$Sr = \frac{\omega d_p}{|\hat{u}_p|}, \quad (4.1)$$

where d_p is the orifice diameter and $|\hat{u}_p|$ is the amplitude of the acoustic particle velocity through the orifice at the excitation frequency. Therefore, Sr is the ratio of the orifice diameter to the amplitude of the acoustic particle displacement. When



Figure 4.1: Formation of the acoustic jet in orifices. The jet continuously changes direction depending on the pressure difference between the two sides of the orifice where d_p and d_j are the orifice and jet cross-section diameters, respectively.

$Sr \gg 1$, the acoustic response of the orifice is linear and for $Sr < 1$ it is non-linear. However, the latter one is divided into two as *transition regime*, i.e. $Sr \sim \mathcal{O}(1)$; and *strongly non-linear* regime for $Sr \ll 1$, where the flow within the orifice is quasi-steady and convective effects dominate over unsteady inertial effects.

The non-linear acoustic response of an orifice is caused by the flow separation as shown by Ingard and Labate [17] in their experiments. When $Sr \ll 1$, this separation results into formation of a free jet as illustrated in Figure 4.1.

In the quasi-steady limit ($Sr \ll 1$), the acoustic transfer impedance of the orifice is predominantly determined by the resistance as shown by the measurements of Ingard and Ising [18]. This non-linear acoustic resistance $\Re\{Z_t\}$ can be approximated by

$$\Re\{Z_t\} = \rho_0 |\hat{u}_p|, \quad (4.2)$$

where ρ_0 is the density of the fluid and $Z_t = (\hat{p}_1 - \hat{p}_2)/\hat{u}_p$ is the transfer impedance of the orifice; as \hat{p}_1 and \hat{p}_2 are the acoustic pressure amplitudes of upstream and downstream, respectively.

However, the expression given in Eq. (4.2) does not take the area contraction of the jet into account. Therefore it is only valid for thin orifices with sharp edges as used by Ingard and Ising [18].

Cummings and Eversman [42] included the effect of various edge profiles into Eq. (4.2) by applying a quasi-steady model based on the unsteady Bernoulli equation.

$$\Re\{Z_t\} = \rho_0 |\hat{u}_p| \frac{1 - \phi^2 C_v^2}{2C_v^2}, \quad (4.3)$$

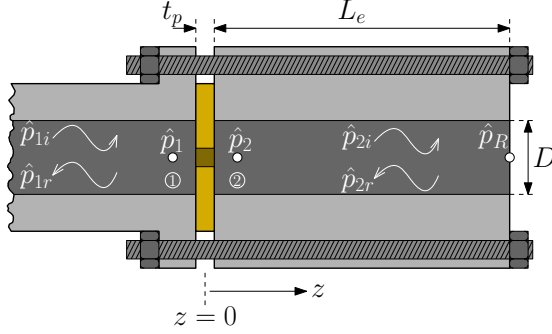


Figure 4.2: Tube termination. The sample is mounted between the tube and the extension ($L_e = 80$ mm).

where $\phi = d_p^2/D^2$ is the porosity of the orifice, D is the pipe diameter, and $C_v = d_p^2/d_j^2$ is the *vena-contracta* factor, which is the ratio of the jet cross-section area ($\pi d_j^2/4$) to the orifice area ($\pi d_p^2/4$). For orifices with porosity value $\phi \sim \mathcal{O}(10^{-2})$, the term $\phi^2 C_v^2$ is negligible.

Please note that, Eq. (4.2) and (4.3) are equivalent for orifices with sharp edges in a thin plate, because in that case the value of *vena-contracta* factor is $C_v \simeq 0.7$ [45].

Based on the quasi-steady approach given in Eq. (4.3), Cummings [57] gives the relation between the upstream and the downstream acoustic pressure oscillations of the orifice as follows:

$$p'_1(t) = p'_2(t) + \rho_0 \frac{u'_p(t)|u'_p(t)|}{2C_v^2} + \rho_0 l_{eq} \frac{du'_p(t)}{dt}, \quad (4.4)$$

where l_{eq} is the equivalent length of the air slug oscillating through the orifice, $p'(t)$ and $u'(t)$ are acoustic pressure and particle velocity oscillations in time domain and subscripts 1, 2 and p represent the upstream, downstream and inside of the orifice, respectively (see Figure 4.2). The linear friction term is neglected in Eq. (4.4). Furthermore, the equivalent length l_{eq} of the orifice is in principle both frequency and amplitude dependent.

Assuming planar harmonic waves on both sides of the orifice, the acoustic pressures $p'_1(t) = \hat{p}_1 \exp(j\omega t)$ and $p'_2(t) = \hat{p}_2 \exp(j\omega t)$ are decomposed into incident

and reflected waves as

$$\hat{p}_1 = \hat{p}_{1i} \exp(-jk_0 z_1) + \hat{p}_{1r} \exp(jk_0 z_1), \quad (4.5a)$$

$$\hat{p}_2 = \hat{p}_{2i} \exp(-jk_0 z_2) + \hat{p}_{2r} \exp(jk_0 z_2), \quad (4.5b)$$

where $k_0 = \omega/c_0$ is the wave number, z_n is the coordinate along the tube, c_0 is the speed of sound, and subscripts i and r stand for *incident* and *reflected* (with respect to the downstream open pipe termination).

As shown in Figure 4.2, the downstream side of the orifice is terminated with an open-end in a semi-anechoic room at $z = L_e$, whose radiation impedance is given by Levine and Schwinger [64] as

$$Z_R = \rho_0 c_0 \left[\frac{1}{4} \left(k_0 \frac{D}{2} \right)^2 + j k_0 \delta_0 \right], \quad (4.6)$$

where $\delta_0 \simeq 0.61(D/2)$ for an unflanged pipe whose inner diameter is D . Then, the acoustic pressure close to the orifice ($z = 0$) downstream is expressed as

$$\begin{aligned} \hat{p}_2 &= \hat{p}_{2i} + \hat{p}_{2r} = \hat{p}_{2i} (1 + \zeta_R) \\ &= \hat{p}_{2i} \left[1 + \frac{Z_R - \rho_0 c_0}{Z_R + \rho_0 c_0} \exp(-2jk_0 L_e) \right], \end{aligned} \quad (4.7)$$

where $\zeta_R = \hat{p}_{2r}/\hat{p}_{2i}$ is the reflection coefficient of the downstream termination.

Applying the conservation of mass law on both sides of the orifice, *i.e.* $\phi \hat{u}_p = \hat{u}_1 = \hat{u}_2$, the following relation between the decomposed acoustic pressures is obtained

$$\hat{p}_{2i} = \frac{\hat{p}_{1i} - \hat{p}_{1r}}{1 - \zeta_R}. \quad (4.8)$$

Neglecting the non-linear term in Eq. (4.4) one obtains the expression for the reflected pressure wave amplitude at the fundamental frequency ω :

$$\hat{p}_{1r} = \hat{p}_{1i} \eta_R + j \left(\frac{1 - \eta_R}{2} \right) \frac{\omega l_{eq} (\hat{p}_{1i} - \hat{p}_{1r})}{c_0 \phi}. \quad (4.9)$$

Neglecting the inertial term and adding the non-linear term of Eq. (4.4) in the time domain, one has for the quasi-steady approximation:

$$p'_{1r}(t) = p'_{1i}(t) \Re\{\eta_R\} + \frac{[p'_{1i}(t) - p'_{1r}(t)] |p'_{1i}(t) - p'_{1r}(t)|}{2\rho_0 c_0^2 \phi^2 C_v^2}. \quad (4.10)$$



Figure 4.3: The difference of the jet area between the inflow and outflow of an orifice with an asymmetrical edge-profile. For the outflow, the separation occurs at the sharp upstream edge and $C_v \simeq 0.7$. For the inflow, the separation takes place downstream and due to the chamfer, the vena contracta factor is $C_v \simeq 0.95$.

In Eq. (4.10), the values for η_R are used at the fundamental frequency ω and the only unknown is $p'_{1i}(t)$. In this study, $p'_{1i}(t)$ is reconstructed from its harmonics \hat{p}_{1ni} as follows:

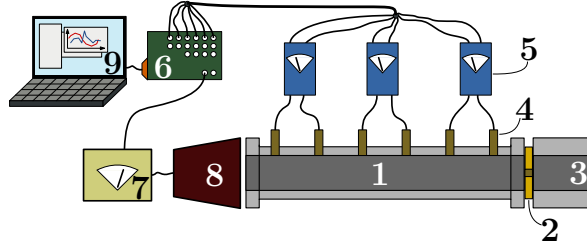
$$p'_{1i}(t) = \text{Re} \left\{ \sum_{n=1}^q \hat{p}_{1ni} \exp(jn\omega t) \right\}, \quad (4.11)$$

where q is the number of harmonics taken into account. Once $p'_{1i}(t)$ is reconstructed, it is introduced into Eq. (4.10) to solve for $p'_{1r}(t)$ for a given time t . In this study, Eq. (4.10) is solved using the `fzero` function of MATLAB[®] for each time step. Then \hat{p}_{1r} and its harmonics are calculated by FFT.

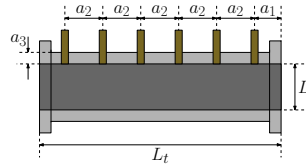
Whilst solving Eq. (4.10), one should take a possible time dependency of C_v into account. For orifices with symmetric edge-profiles C_v is constant. However, for asymmetrical edge-profiles as shown in Figure 4.3, C_v changes value depending on the direction of the flow through the orifice. As proposed by Förner *et al.* [62], $C_v = C_v^+$ used for $p'_1(t) > p'_2(t)$ and $C_v = C_v^-$ used for $p'_1(t) < p'_2(t)$ in Eq. (4.10). This time dependence for asymmetrical edge-profiles is iteratively taken care in the calculations.

4.3 Experiments

The acoustic response of seven samples was measured using an impedance tube set-up in a semi-anechoic chamber. The details of the set-up and the samples are provided in this section.



(a) Schematic description of the experimental set-up.



(b) Microphone positions on the impedance tube (1).

Figure 4.4: (a) 1-Impedance tube, 2-orifice, 3-extension, 4-microphone(s), 5-microphone amplifier(s), 6-data acquisition card, 7-loudspeaker amplifier, 8-loudspeaker, 9-analyser; (b) $a_1 = 50$ mm, $a_2 = 175$ mm, $a_3 = 10$ mm, $L_t = 1$ m and $D = 50$ mm.

4.3.1 Description of the set-up

The set-up is composed of an aluminium tube, six microphones and microphone amplifiers, a speaker, a power amplifier and an analyser. The schematic drawing of the set-up is provided in Figure 4.4a.

The aluminium tube is 1-m long and the wall thickness is 10 mm. There are six mounts opened along the tube to fit the microphones in, whose positions are specified in Figure 4.4b. Both ends of the tube are flanged allowing various structures to be attached.

The analyser consists of an *NI PCIe-6361 X-Series* data acquisition card and a PC with *NI LabView* software. The data acquisition card has 16 analog input and 2 analog output channels. The sampling rates for the input and output signals are 10 kHz and 20 kHz, respectively.

The microphones are $1/4''$ pre-polarized BSWA-type microphones with a sensitivity of 50 mV/Pa. Before measuring, absolute calibration is performed on the closest microphone to the tube termination. It is calibrated by using a B&K hand-

Table 4.1: Properties of the samples measured in this study. **S**: square-edge; **OSC**: one-side-chamfered; **BSC**: both-sides-chamfered; **P**: punched; and **IC**: inverted-chamfer. All of the samples have the same orifice diameter $d_p = 4.2$ mm, and porosity $\phi = 0.7\%$.

Sample	t_p [mm]	t_{eff} [mm]	c_p [mm]	Edge Profile
1	4.00	4.00	0	S
2a	4.00	3.65	0.35	OSC
2b	4.00	3.30	0.35	BSC
3a	4.00	3.0	1.0	OSC
3b	4.00	2.0	1.0	BSC
4	4.00	4.0	1.0	P
5	2.00	4.0	1.0	IC

held piston-phone at 1000 Hz for 1 Pa amplitude ($SPL = 99.4$ dB). The remaining microphones are calibrated relative to the first one using a specially designed apparatus. This apparatus ensures that all the microphones are located at the same distance from a closed-end termination so that they are exposed to identical pressure fluctuations simultaneously. The difference in the measurements are eliminated by a set of calibration coefficients for each microphone at each frequency.

To excite the air in the tube, a 3.5", 25 W loudspeaker is used. This loudspeaker is detached from the tube to avoid coupling with the structural vibration modes.

4.3.2 Description of the samples

To study the effect of edge profiles in orifices, samples with comparable plate thickness and orifice diameter are chosen for the measurements. The main difference between these samples are the edge-profiles as shown in Figure 4.5.

All of the samples are made of brass except for Sample 5, which is made of aluminium. The samples are located at the end of the tube and supported by an 80-mm length extension for sample mounting. To prevent the air leakage in mounting, o-rings are used where metal-to-metal contact is present.

The samples are designed to have the same orifice diameter $d_p = 4.2$ mm and the porosity value $\phi = 0.7\%$. Besides, the plate thickness is not always equal to the effective plate thickness t_{eff} , which is the length of the orifice with constant diameter in z -direction. The physical properties of the samples are listed in Table 4.1.

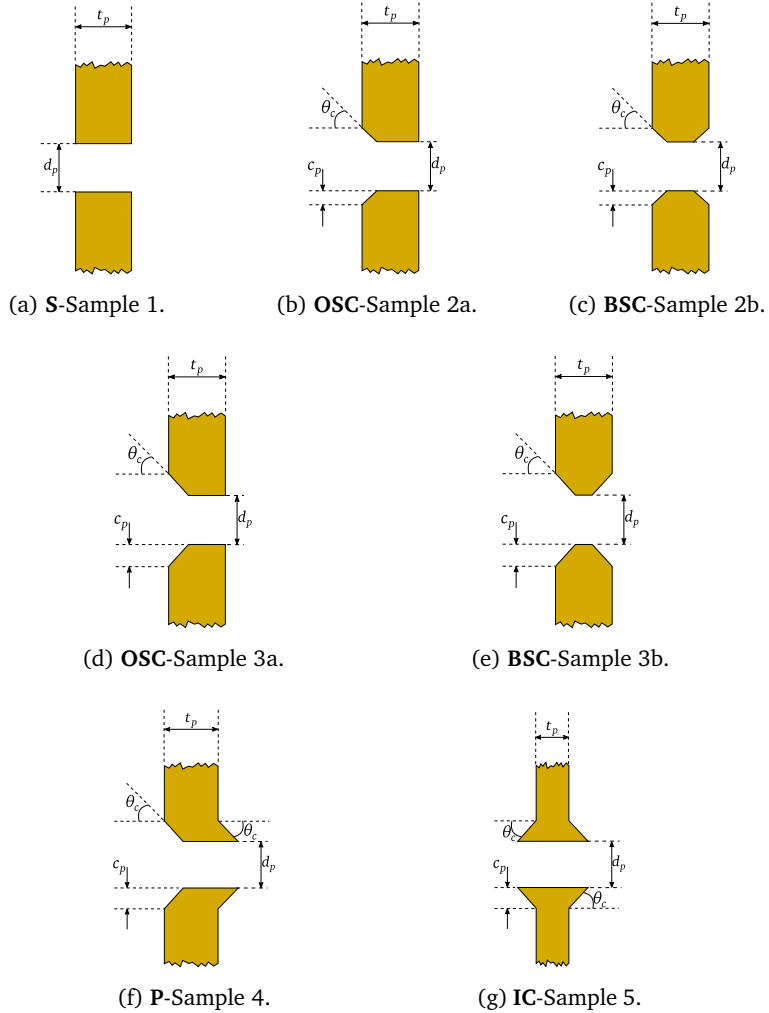


Figure 4.5: Edge profiles of the samples. (a) Square-edge (**S**), (b) and (d) one-side-chamfered **OSC**, (c) and (e) both-sides-chamfered **BSC**, (f) punched **P** and (g) inverted-chamfer **IC** edge profiles ($\theta_c = 45^\circ$). Samples (b) and (c) have small chamfers ($c_p = 0.35$ mm) whereas Samples (c) and (e) have large chamfers ($c_p = 1.0$ mm).

Table 4.2: The list of excitation frequency and reference amplitude values used in the measurements.

Frequency	Value	Amplitude	Value
f_1	80 Hz	A_1	0.4 Pa
f_2	120 Hz	A_2	0.8 Pa
f_3	160 Hz	A_3	1.6 Pa
f_4	240 Hz	A_4	3.2 Pa
f_5	280 Hz	A_5	6.4 Pa
f_6	140 Hz	A_6	13 Pa
f_7	180 Hz	A_7	20 Pa
f_8	220 Hz	A_8	26 Pa
f_9	260 Hz	A_9	32 Pa
		A_{10}	40 Pa

4.3.3 Measurement procedure

The amplitude of the generated signal that drives the loudspeaker is regulated by a custom-built measurement script in *LabView* software. This script measures the signal amplitude of the microphone closest to the sample and iterates the output signal amplitude until it matches the desired value. The actual measurement does not start until the desired amplitude is reached. The measurements are performed for 9 frequency and 10 amplitude values for each sample (see Table 4.2). The acoustic velocity amplitude in the perforation ($|\hat{u}_p|$) is computed as described by Temiz *et al.* [37].

Some precautions are taken for increasing the accuracy of the measurements. For example, there is a 10-minute *cool-down* period after every five measurement steps in order to prevent a possible temperature gradient in the tube. For the same token, a monotonous increase in excitation frequency is avoided as it is shown in Table 4.2. Furthermore, the grid frequency (50 Hz) and its harmonics are excluded in the measurements. Additionally, some physical precautions are taken. For example, the tube and the loudspeaker are separated (no mechanical contact). The microphone cables are fixed by means of Scotch tape to the tube in order to minimize the effects of structural vibrations in the measurements. Eventually, the measured reflection coefficient of a closed-end termination deviates from the theoretical value by 0.5% at most in the frequency span of interest (80 – 280 Hz).

4.3.4 Post-processing

The time data in each measurement step is processed by a custom-built MATLAB[®] script after the measurements. First, a lock-in method is used for translating the time data into frequency domain for each microphone. Using the wave decomposition by Jang and Ih [32], the incident and reflected complex pressure amplitudes, \hat{p}_{1i} and \hat{p}_{1r} , respectively, are obtained to be able to calculate the reflection coefficient

$$\zeta = \frac{\hat{p}_{1r}}{\hat{p}_{1i}}. \quad (4.12)$$

Moreover, the transfer impedance of the samples is estimated by the open-end transfer impedance measurements as described by Temiz *et al.* [24].

4.4 Results and Discussions

4.4.1 Non-dimensional parameters

To allow for more general conclusions, the quantities measured in this study are made non-dimensional.

The real part of the transfer impedance is normalized by the quasi-steady limit proposed by Ingard and Ising [18] so that

$$\tilde{\Re} = \frac{\Re\{Z_t\}\phi}{\rho_0|\dot{u}_p|}. \quad (4.13)$$

The imaginary part of the transfer impedance is normalized by the reactive end-correction coefficient proposed by Ingard [15] as

$$\tilde{\Im} = \frac{2\Im\{Z_t\}\phi}{\rho_0\omega d_p}. \quad (4.14)$$

The Shear number is the ratio of the oscillating boundary layer (Stokes layer) thickness to the orifice diameter

$$Sh = d_p \sqrt{\frac{\omega\rho_0}{\mu}}, \quad (4.15)$$

where μ is the dynamic viscosity and ρ_0 is the density of air. In other words, the excitation frequency is made non-dimensional by using it to calculate the Shear number. This study focuses on high Sh results.

4.4.2 Effect of edge profile

The results with $Sh = 12.1$ are shown in Figure 4.6. To help the reader, the edge-profiles of the samples are added to the beginning of the sample name in the rest of the text, e.g. **S**-Sample 1, **OSC**-Sample 2a, etc.

As it can be seen in Figure 4.6, the edge profiles affect the resistance significantly in the non-linear regime, i.e. $Sr < 1$. For example, the normalized resistance of **S**-Sample 1 is $\sim 50\%$ larger than that of **BSC**-Sample 3b. This difference in the linear regime is around 30%.

Secondly, as indicated in Figure 4.5 and Table 4.1, the difference between **BSC**-Sample 2b and **BSC**-Sample 3b is the chamfer size. Although the chamfer size increases by 3 times in this comparison, the difference in the normalized resistance is only about 10%. Same type of behaviour can be observed in the one-sided-chamfer case, namely between **OSC**-Sample 2a and **OSC**-Sample 3a. As mentioned by Förner *et al.* [61], corners with obtuse angle prevent the flow separation in the perforations. Therefore the non-linear sound absorbing mechanism loses its efficiency in the presence of chamfers. However, the chamfer size does not affect the vortex shedding mechanism significantly. Thus, increasing the chamfer size does not modify the non-linear resistance considerably.

On the other hand, **S**-Sample 1 and **IC**-Sample 5 exhibit comparable non-linear behaviour in terms of normalized resistance. This implies the acoustic flow separation from an edge with acute angle behaves similarly to the one from an edge with right angle. This argument is supported by the normalized resistance values of **OSC**-Sample 3a and **P**-Sample 4 in non-linear regime, which are also comparable.

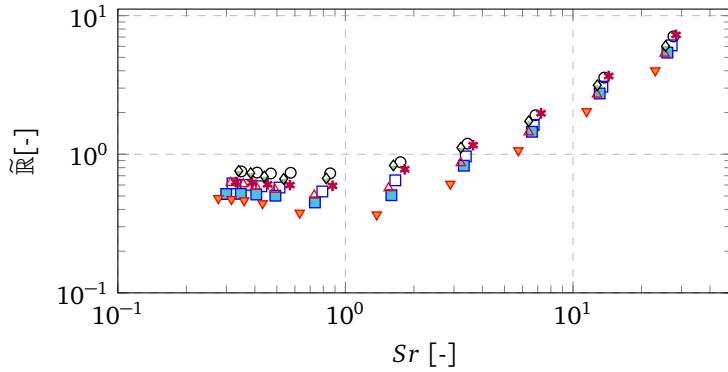
The acoustic reactance of an orifice decreases as non-linearity increases ($Sr \rightarrow 0$). This phenomenon is also observed by Bies and Wilson [55], Ingard and Ising [18], and Melling [56] in their measurements. This decline is due to the fact that flow separation causes a reduction in the oscillating mass through the orifice.

Compared to the resistance, the effect of edge profile on normalized reactance is limited, but still evident. For example, when Sr is changed from 25 to 0.3, the relative decrease in \tilde{X} for **S**-Sample 1 and **IC**-Sample 5, is $\sim 40\%$, where it is $\sim 30\%$ for **BSC**-Sample 2b and **BSC**-Sample 3b.

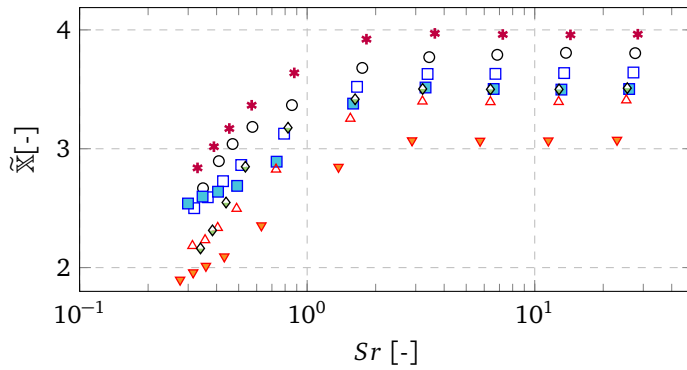
Consequently, edge profiles reducing flow separation reduce the non-linear effects in acoustic response of orifices.

4.4.3 Sound generation in higher harmonics

Sound generation in higher harmonics due to non-linearity is studied for Samples 1, 2a and 3a. For each sample, \hat{p}_{1r} and its harmonics are both measured and



(a) Normalized resistance. (x and y-axes are shown in logarithmic scale)



(b) Normalized reactance. (x and y-axes are shown in logarithmic and linear scales, respectively.)

Figure 4.6: The effect of the edge profile on (a) the normalized resistance, (b) normalized reactance of an orifice. **S**-Sample 1 (\circ), **OSC**-Sample 2a (\square), **BSC**-Sample 2b (\blacksquare), **OSC**-Sample 3a (\triangle), **BSC**-Sample 3b (\blacktriangledown), **P**-Sample 4 ($*$) and **IC**-Sample 5 (\diamond) at $Sh = 12.1$. (See sample geometries in Figure 4.5.)

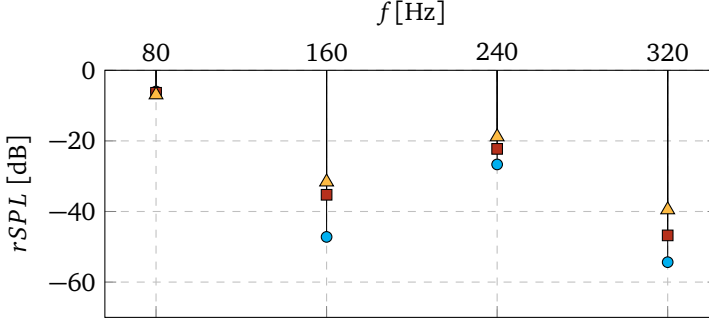


Figure 4.7: Measured $rSPL_n = 20 \log(\hat{p}_{1nr}/\hat{p}_{11i})$ values for **S**-Sample 1 (●-symmetrical square-edges), **OSC**-Sample 2a (■-asymmetrical small chamfer) and **OSC**-Sample 3a (▲-asymmetrical large chamfer): $f_1 = 80$ Hz.

computed by means of Eq. (4.10) and they are compared by means of a reflected sound pressure level, $rSPL$, which is defined as

$$rSPL_n = 20 \log \left(\frac{\hat{p}_{1nr}}{\hat{p}_{11i}} \right), \quad (4.16)$$

where \hat{p}_{1nr} is the n^{th} harmonic of the reflected pressure wave in the tube and \hat{p}_{11i} is the fundamental harmonic of the incident pressure wave in the tube. The measurements are restricted to 80 Hz and 120 Hz, allowing a high accuracy at low Sr . In calculations, the first four harmonics are taken into consideration. Unfortunately the fifth harmonic is a multiple of the grid frequency 50 Hz.

In Figure 4.7 the measured $rSPL$ values for **S**-Sample 1, **OSC**-Sample 2a and **OSC**-Sample 3a are compared for the fundamental frequency of 80 Hz.

As it can be seen from Figure 4.7, **OSC**-Sample 2a and **OSC**-Sample 3a exhibit a significantly stronger sound generation in the even-harmonics, *i.e.* 160 Hz and 320 Hz, due to the asymmetry between the inflow and outflow conditions (see Figure 4.3). However, the sound generation at odd-harmonic (240 Hz) is dominant compared to the even-harmonics, which is in accordance with the detailed numerical flow simulation results from the study by Förner *et al.* [62].

In Figure 4.8, the measured $rSPL$ values are compared with the calculated ones, which are obtained using quasi-steady approach given in Eq. (4.10). In the analytical model, the relevant value for the *vena-contracta* factor is chosen from Table 4.3.

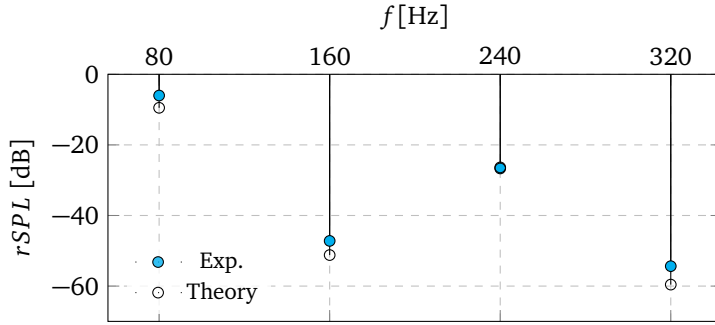
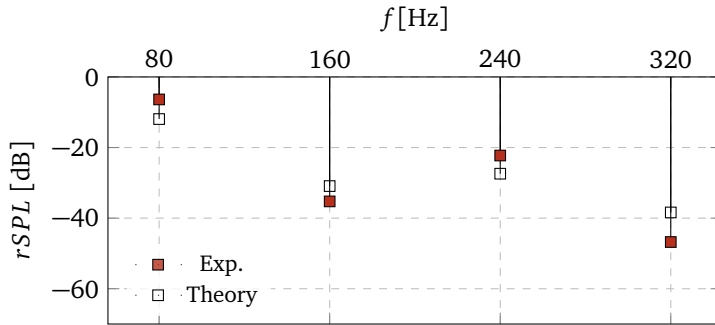
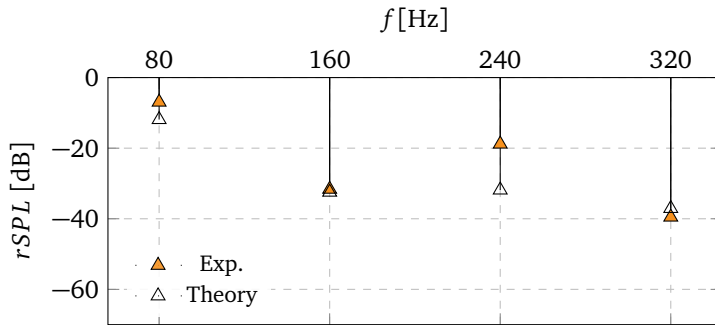
(a) S-Sample 1, $Sr = 0.35$.(b) OSC-Sample 2a, $Sr = 0.32$.(c) OSC-Sample 3a, $Sr = 0.31$.

Figure 4.8: Quasi-steady model vs measurements ($rSPL = 20 \log(\hat{p}_{1mr}/\hat{p}_{ref})$, $f_1 = 80 \text{ Hz}$, $\hat{p}_{ref} = \hat{p}_{11i}$).

Table 4.3: Value table for *vena-contracta* factor (C_v) during acoustic flow through the samples.

	$p'_1(t) > p'_2(t)$	$p'_1(t) \leq p'_2(t)$
Sample 1 and 5	0.70	0.70
Sample 2a, 3a and 4	0.70	0.95
Sample 2b and 3b	0.95	0.95

As it can be seen in the comparison graphs, the $rSPL$ values calculated for the first harmonic using the quasi-steady approach deviates by ~ 4 dB. This is due to the fact the system is still in the transition regime at $Sr \sim 0.35$. In other words, the contributions from the linear resistance and reactance are not small enough to be neglected. However, the quasi-steady approach in time domain succeeds to capture the effect of asymmetrical edge profile on sound generation in higher harmonics.

One can observe even a further deviation in $rSPL$ values if the quasi-steady approach is used for higher Sr values ($Sr \sim 0.6$) as in Figure 4.9.

If the system is not in strongly non-linear regime, then the quasi-steady approach starts underestimating the reflection coefficient in the fundamental frequency and overestimating the sound generation in the odd-harmonic. As stated in Chapter 3, for $Sr \sim 1$, the non-linear response of an orifice is not only function of Sr , but also a function of Sh . However, the quasi-steady model does not take the viscous losses into consideration. As it is seen in Figure 4.10, the normalized resistance curves start separating from each other at $Sr \simeq 0.5$.

The observations for the validity of the quasi-steady approach is complemented by comparing the measured and calculated values of the reflection coefficients for all the samples previously mentioned in this chapter (see Fig. 4.5). In Tables 4.4 and 4.5, ζ_{exp} and ζ_{qs} represent the reflection coefficients which are measured, and calculated using the quasi-steady approach, respectively. Please note that Table 4.4 provides the results for 80 Hz, whereas Table 4.5 presents for 120 Hz.

4.5 Conclusions

In this study, the effect of edge profiles on the non-linear response of an orifice and sound generation in higher harmonics is studied.

It is observed that the edge profile plays an important role in the non-linear resistance. For example, orifices with both-sides-chamfered edge-profile (**BSC**) ex-

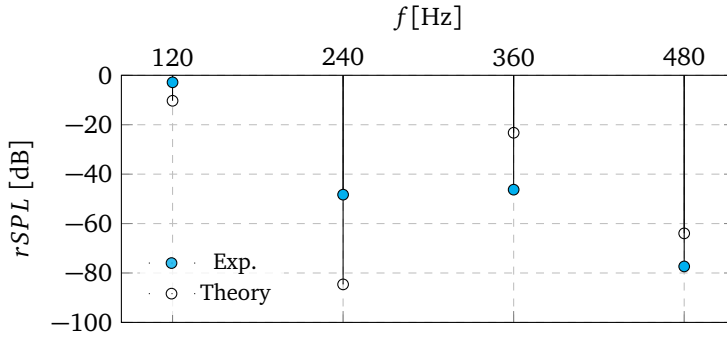
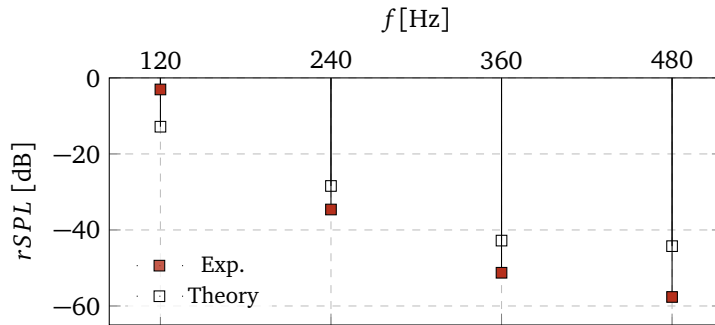
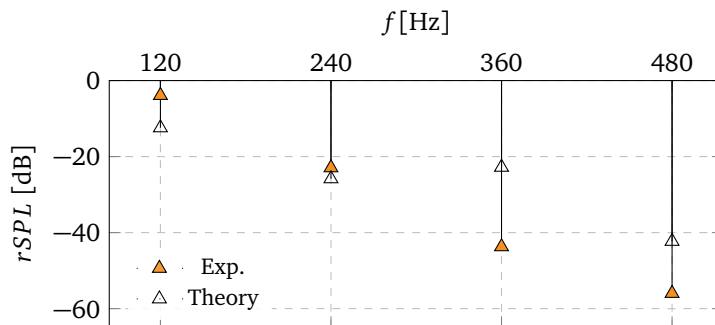
(a) S-Sample 1, $Sr = 0.64$.(b) OSC-Sample 2a, $Sr = 0.56$.(c) OSC-Sample 3a, $Sr = 0.56$.

Figure 4.9: Quasi-steady model vs measurements ($rSPL = 20 \log(\hat{p}_{1mr}/\hat{p}_{ref})$, $f_1 = 120\text{Hz}$).

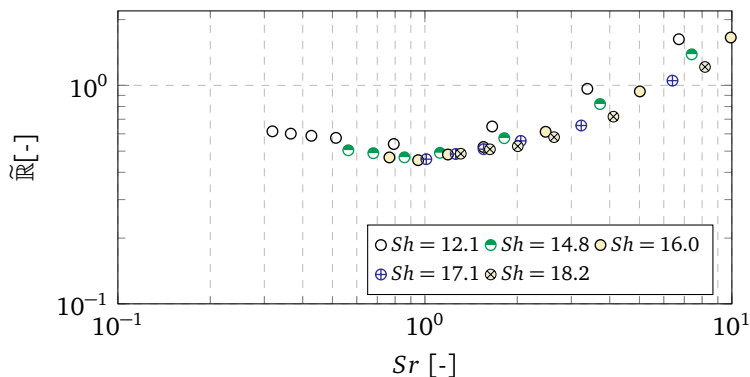


Figure 4.10: Sample 2a, Sh range. (Both x and y -axes are shown in logarithmic scale.)

Table 4.4: Comparison of measured and estimated reflection coefficient amplitudes at the fundamental harmonic frequency $f = 80$ Hz.

	Sr	$ \zeta_{exp} $	$ \zeta_{qs} $
Sample 1	0.38	0.50	0.34
Sample 2a	0.35	0.48	0.25
Sample 2b	0.33	0.48	0.17
Sample 3a	0.34	0.45	0.25
Sample 3b	0.30	0.41	0.19
Sample 4	0.36	0.51	0.25
Sample 5	0.37	0.46	0.34

hibit 50% less non-linear resistance compared to the one with square-edge profile (S). The chamfers delay acoustic flow separation to higher excitation amplitudes.

The presence of a chamfer is more substantial than the size of it for non-linear response. Tripling the size of a chamfer provides only $\sim 10\%$ more reduction in the normalized resistance.

An inverse-chamfer edge-profile (IC) behaves similarly to the square-edge profile considering the non-linear resistance. Therefore, it is possible to model the edge profiles with acute angles as square-edges in non-linear regime.

As non-linearity increases, the normalized transfer reactance decreases. Al-

Table 4.5: Comparison of measured and estimated reflection coefficient amplitudes at the fundamental harmonic frequency $f = 120$ Hz.

	Sr	$ \zeta_{exp} $	$ \zeta_{qs} $
Sample 1	0.70	0.72	0.31
Sample 2a	0.61	0.71	0.23
Sample 2b	0.56	0.68	0.15
Sample 3a	0.56	0.64	0.24
Sample 3b	0.49	0.60	0.16
Sample 4	0.69	0.77	0.22
Sample 5	0.65	0.69	0.31

though this reduction depends less on the edge profile, the decrease in **BSC** is less than **S** and **IC** by $\sim 15\%$.

A quasi-steady theory is employed to study the sound generation in higher harmonics. However, it is observed this approach fails to represent the acoustic response of an orifice at the transition regime ($Sr \sim 1$). For the fundamental harmonic, the deviation between the measured and estimated reflection coefficients is about 4 dB for $Sr \simeq 0.3$ and 10 dB for $Sr \simeq 0.6$. Although the quasi-steady approach is an efficient method to estimate the non-linear response of an orifice and even sound generation at higher harmonics in strongly non-linear regime, it does not represent the acoustic behaviour accurately in transition regime ($Sr \sim \mathcal{O}(1)$). Therefore, it is evident that a more sophisticated approach is required to capture the acoustic response of an orifice in the transition regime.

Chapter 5

Building a Numerical Model to Investigate the Effect of Perforation Distribution in Flexible Micro-Perforated Plates¹

Abstract

This study proposes a Finite Element (FE)-based efficient numerical model of the vibro-acoustic coupling in flexible micro-perforated plates (f-MPPs) where each perforation is described as an imposed impedance boundary condition (uniform impedance patch) on the plate. This approach opens the possibility of predicting the influence of perforation distribution on the acoustic performance of f-MPP. Micro perforated plates have been a topic of interest as a promising sound absorber in a wide range of applications, from room acoustics to combustion chambers. One great advantage of these plates is that it gives the designer the freedom of choice on material in production. Depending on the material and the dimensions, the acoustical modes of the medium can couple with the structural modes of the plate. This

¹The content of this chapter is compiled as a manuscript by M.A. Temiz, J. Tournadre, I. Lopez Arteaga and A. Hirschberg; and submitted to *Applied Acoustics* in November 2016.

coupling changes the number of absorption peaks, frequency and amplitude of the Helmholtz resonance of the system, therefore the coupling becomes an extra parameter in the design process. Current analytical models superpose the mechanical impedance of the plate with the acoustic impedance of the perforations to compute this coupling. This approach works fairly well for plates with uniform perforation distribution. If a non-uniform distribution is required, the conventional methods fall short in calculating the acoustic response of an f-MPP. This study proposes a numerical method which assumes perforations as discrete impedance patches on the flexible plate so that they can be considered separately. The method couples the solution of the Helmholtz equation in air with shell plate theory to model the vibro-acoustic effects and the impedance patches are represented as imposed transfer impedance boundary conditions. The assessment of the method is performed in terms of comparing the calculated absorption coefficient values from the simulations of several test cases, fundamental theories and measurement results from the literature. The simulation results agree both with these theoretical limits and measurement results.

5.1 Introduction

Micro-perforated plates (MPPs) have been designated as high potential sound absorbers by Maa [6] for various applications including the ones with severe environments. Before the study of Maa [6], they were used only as protective layer for classical sound absorbers. MPPs are plates with small perforations whose diameter is in the order of 1 mm with low porosity values, *i.e.* $\phi = \mathcal{O}(1\%)$. When backed by a cavity, they provide broadband acoustic dissipation compared to Helmholtz resonators.

The present study is limited to the amplitude range for which the behaviour can be described by a linear model. This excludes damping due to vortex shedding. The linear sound absorption mechanism in MPPs is based on the conversion of the kinetic energy of the fluid particles into heat energy due to the viscous resistance in the perforations. As the viscous resistance increases with the relative velocity between the plate and the fluid, the kinetic energy loss of the particles and the corresponding sound absorption is larger when the excitation frequency approaches to the Helmholtz resonance frequency of the back cavity. For a rigid MPP, the relative particle velocity of the air is the same for each perforation at all frequencies when excited by a planar acoustic wave. On the other hand, when the plate is flexible, at certain frequencies the plate vibrates with the mode shape depending on its geometry, excitation frequency, boundary conditions and material. Due to this

mode shape, even under acoustic plane wave excitation, the relative air particle velocity with respect to the plate depends on the position of the perforation within the plate. Therefore, the perforation position is potentially a design parameter in flexible micro-perforated plates (f-MPPs).

Sound absorption by flexible plates is a known phenomenon in room acoustics. One of the first analytical models for a flexible plate, which does not have perforations but backed by an air cavity, is provided by Cremer and Müller [65]. In this model, they couple the bending waves of the flexible plate with the acoustic waves of the air cavity. An important contribution to this model is made by Basten *et al.* [66]. They consider an enclosed air cavity between two flexible plates and the distance between these plates are small. Basten *et al.* [66] analytically show that, such a small gap between the flexible plates causes the visco-thermal effects to become dominant in the cavity.

On the MPP side, the first scientists to observe that plate vibrations affect the absorption mechanism are Lee and Swenson [22]. In their experiments, they report an additional absorption peak which cannot be modeled by the rigid MPP theory. The first analytical model including the flexible effects in MPPs is given by Lee *et al.* [67]. Inspired by their work, Toyoda *et al.* [68] propose a similar approach for modeling of f-MPPs having circular geometry. Both Lee *et al.* [67] and Toyoda *et al.* [68] calculate the structural impedance of the flexible plate using modal analysis and combine it with the acoustic transfer impedance defined by Maa [6]. In both of these studies, the mathematical models are verified by experiments. Bravo *et al.* [9, 69] consider a case where the back cavity walls are flexible and provide a theoretical model where the absorption mechanism is governed by the relative velocity between the air particles and the flexible plate. They verify this model by experiments. Li *et al.* [70] propose a sophisticated model to account for the non-zero velocity boundary condition at the inner walls of the perforations. This boundary condition redefines the classical acoustic transfer impedance expression by Maa [6].

All of the studies mentioned so far explain a different aspect of the vibro-acoustic coupling in f-MPPs. On the other hand, except for the one by Li *et al.* [70], all of the studies use the concept of a plate-averaged MPP transfer impedance. Even though the model by Li *et al.* [70] takes perforation positions into account, their method confine them to radial distributions only. In case of uniform distribution of perforations, the aforementioned methods are all adequate, yet they fall short in case of a non-uniform spatial distribution.

The focus of this study is to provide a numerical method for modelling f-MPPs in a way that each perforation is considered separately. Thus it can be used for investigating the acoustic properties of an f-MPP with a non-uniform perforation

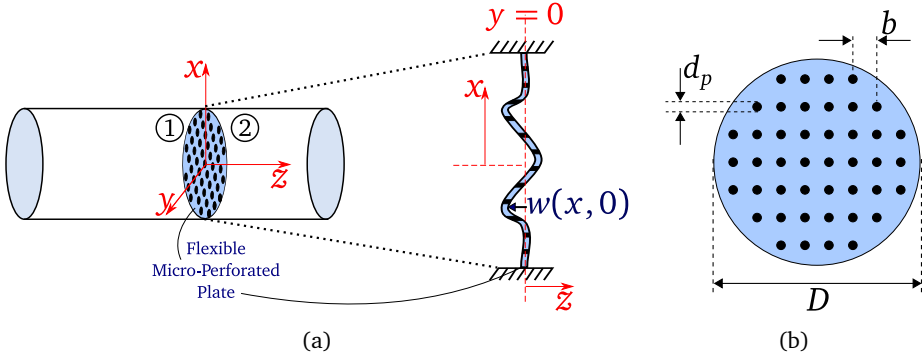


Figure 5.1: (a) The schematic drawing of the flexible micro-perforated plate (f-MPP) placed between the impedance tube (Domain ①) and the back cavity (Domain ②). The plate displacement vector $w(x, y)$ is also illustrated on the cross-sectional view of the f-MPP; (b) front view of an f-MPP whose perforations are distributed uniformly.

distribution, allowing one to design the optimum distribution for a desired acoustic response.

To validate the theory, a cylindrical impedance tube is modelled numerically and the acoustic properties of the f-MPP with a back cavity is assessed in terms of absorption coefficient, β . The model outputs are compared with fundamental plate and acoustic theories and experiments reported in the literature.

5.2 Theoretical Background

The numerical domain of the impedance tube configuration, which is presented schematically in Figure 5.1, is composed of two domains: a structural domain (shell) and an acoustic domain. This section provides the governing equations used for modelling these domains.

5.2.1 Structural domain

The equation of motion of the thin, homogeneous flexible plate shown in Figure 5.1 is given by Kirchhoff [71] as

$$D_p \nabla^2 \nabla^2 w(r) - \rho_p t_p \omega^2 w(r) = \hat{P}, \quad (5.1)$$

where ∇^2 is the *Laplacian* operator, $w(x, y)$ is the plate displacement in the z -direction, ρ_p is the plate density (mass per unit of surface), t_p is the plate thickness; \hat{P} is the external pressure difference acting on the plate; $D_p = E(1 + j\eta)t_p^3/[12(1 - \nu^2)]$ is the flexural rigidity of the plate where j is the imaginary number ($j^2 = -1$), E is the Young's modulus, η is the loss factor and ν is the Poisson ratio of the plate material. As the typical porosity of an f-MPP is in the order of 10^{-2} [24], the effect of perforations on the structural properties of the flexible plate is ignored for the modelling.

5.2.2 Acoustic domain

Domains ① and ② in Figure 5.1 are acoustic domains and they are assumed to be excited by harmonic plane waves. Furthermore, thermo-viscous losses at the sound-hard boundaries are negligible in these acoustic domains. Under these assumptions, the spatial pressure distribution in frequency domain is given by Helmholtz equation [8]

$$\omega^2 \hat{p}_n(z) + c_0^2 \nabla^2 \hat{p}_n(z) = 0, \quad (5.2)$$

where $\omega = 2\pi f$ is the radial frequency, c_0 is the speed of sound in air and \hat{p}_n is the acoustic pressure in frequency domain for acoustic medium n ; *i.e.* $n = 1$ for the impedance tube and $n = 2$ for the back cavity domains, respectively (see Figure 5.1).

The two acoustical domains in Figure 5.1 are connected through micro-perforations which can be considered as independent *uniform impedance patches* on the flexible plate. These patches are defined as imposed transfer impedance boundaries in the numerical model and the mathematical expression for each patch is given by Temiz *et al.* [24] as

$$Z_t = \frac{\hat{p}_1 - \hat{p}_2}{\hat{u}_p} = j\omega t_p \rho_0 \left[1 - \frac{2 J_1(Sh\sqrt{-j})}{Sh\sqrt{-j} J_0(Sh\sqrt{-j})} \right]^{-1} + 2\alpha_s R_s + j\delta_s \omega \rho_0 \frac{d_p}{2}, \quad (5.3)$$

where \hat{u}_p is the average acoustic particle velocity in the perforation, ρ_0 is the density of the acoustic medium and J_m is the Bessel function of first kind of order m . The other parameters in Eq. (5.3) are calculated for square-edged perforations as [24]

$$Sh = d_p \sqrt{\omega \rho_0 / (4\mu)}, \quad (5.4a)$$

$$R_s = 0.5 \sqrt{2\mu \rho_0 \omega}, \quad (5.4b)$$

$$\alpha_s = 5.08 Sh^{-1.45} + 1.70, \quad (5.4c)$$

$$\delta_s = 0.97 \exp(-0.20Sh) + 1.54, \quad (5.4d)$$

where Sh is the Shear number: the ratio of the perforation diameter to the oscillating boundary layer thickness, μ is the dynamic viscosity of air (1.82×10^{-5} kg/ms at 20°C), R_s is the surface resistance, α_s and δ_s are resistive and reactive end-correction coefficients for circular orifices with square-edge geometries. Note that as α_s and δ_s are functions of Sh , they take the effect of viscosity on the inductance into account. Other expressions for other edge geometries are proposed by Temiz *et al.* [24]. The expression given in Eq. (5.3) is valid when the perforations are far enough from each other, so that they do not interact. Eq. (5.4) is based on numerical simulations and was validated experimentally [24].

5.3 Numerical Model

The numerical model is built in the finite element program COMSOL Multiphysics® (ver. 5.0) [23] using the built-in *Pressure Acoustics* and *Plate* modules. The model represents a cylindrical impedance tube set-up with two microphones to estimate the absorption coefficient. At one end of the tube, the flexible micro-perforated plate and the back cavity is placed where the other end is used for introducing the acoustic plane wave into the system. The micro-perforations are modelled as described in the previous section. The simplified representation of the numerical domain, which describes the boundary conditions employed, is given in Figure 5.2.

5.3.1 Boundary conditions

Four types of boundary conditions are used to model the configuration represented in Figure 5.1.

- Imposed pressure boundary (Ω_p): To represent the plane wave excitation incident to the f-MPP, this boundary condition is employed at the upstream of the tube geometry. The equation for this boundary is

$$\hat{p}|_{\Omega_p} = \hat{p}_{ex}, \quad (5.5)$$

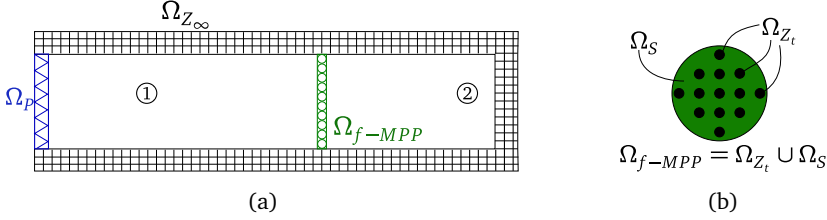


Figure 5.2: The description of the boundary conditions used for modelling the (a) impedance tube; (b) f-MPP: Ω_p is the imposed pressure, Ω_{Z_∞} is the sound-hard, Ω_{f-MPP} is the f-MPP, Ω_{Z_t} is the imposed transfer impedance and Ω_S is the vibro-acoustic coupling boundary.

where \hat{p}_{ex} is the prescribed pressure amplitude (in frequency domain).

- Sound-hard boundary (Z_∞): The normal acoustic velocity vanishes at the side walls of the impedance tube and the termination of the back cavity by this boundary condition.

$$\hat{u}|_{\Omega_{Z_\infty}} = 0. \quad (5.6)$$

- Imposed transfer impedance boundary (Ω_{Z_t}): The change ($\hat{p}_1 - \hat{p}_2$) in the acoustic pressure from Domain ① to ② through the perforations is related to the particle velocity (\hat{u}_p) by the boundary condition, on the patch surface

$$\frac{\hat{p}_1 - \hat{p}_2}{\hat{u}_p}|_{\Omega_{Z_t}} = Z_t, \quad (5.7)$$

where Z_t is calculated by using Eq. (5.3).

- Vibro-acoustic coupling boundary (Ω_S): On this boundary, the acoustics of Domains ① and ② are coupled with the structural vibrations of the shell domain. This is achieved by the following equations

$$\hat{u}(x, y)|_{\Omega_S} = \frac{dw(x, y)}{dt} = j\omega w(x, y) \quad (5.8a)$$

$$\hat{P}|_{\Omega_S} = \hat{p}_1|_{\Omega_S} - \hat{p}_2|_{\Omega_S}, \quad (5.8b)$$

where Eq. (5.8a) couples the plate displacements with the acoustic particle velocity and Eq. (5.8b) couples the forcing source term in Eq. (5.1) on the

flexible plate with the acoustic pressure difference between Domains (1) and (2).

The boundary condition represented as Ω_{f-MPP} is the combination of Ω_{Z_i} and Ω_S , as can be seen in Figure 5.2

5.3.2 Finite element model

The finite element model of the configuration is obtained by discretizing Eqs. (5.1) and (5.2) over the numerical domain using quadratic shape function for both acoustic and structural domains. After introducing the boundary conditions (Eqs. (5.5)-(5.8)) into the weak form of the governing equations (Eqs. (5.1) and (5.2)), the system of equations representing the numerical model takes the following form:

$$\left\{ \begin{bmatrix} \mathbf{K}_s & \mathbf{K}_c \\ 0 & \mathbf{K}_a \end{bmatrix} + j\omega \begin{bmatrix} \mathbf{C}_s & 0 \\ 0 & \mathbf{C}_a \end{bmatrix} - \omega^2 \begin{bmatrix} \mathbf{M}_s & 0 \\ \mathbf{M}_c & \mathbf{M}_a \end{bmatrix} \right\} \begin{Bmatrix} \mathbf{w}_u \\ \mathbf{p}_u \end{Bmatrix} = \begin{Bmatrix} \mathbf{F}_{si} \\ \mathbf{F}_{ai} \end{Bmatrix}, \quad (5.9)$$

where, \mathbf{K} is the stiffness, \mathbf{M} is the mass, \mathbf{C} is the dissipation and \mathbf{F} is the forcing matrices. The subscripts 'a', 's' and 'c' represent the words *acoustic*, *structural* and *coupling*. The vectors \mathbf{w}_u and \mathbf{p}_u stand for the free plate displacement and acoustic pressure vectors, respectively. These are the vectors that are not imposed as boundary conditions and need to be solved for. The imposed boundary conditions introduced in the acoustic and structural forcing vectors, \mathbf{F}_{ai} and \mathbf{F}_{si} . Finally, Eqs. (5.8a) and (5.8b) are represented by \mathbf{M}_c and \mathbf{K}_c , respectively [72].

The system of equations given in Eq. (5.9) is solved by using a direct linear solver.

5.3.3 Meshing

The mesh used for discretizing the numerical domain is built by COMSOL automatically based on the physics used in the model. The *extra-fine* mesh option is chosen for all models in this study. Although it is built automatically, the mesh is manually checked to satisfy following conditions: (1) the largest acoustic element is never larger than 1/10 of the smallest acoustic wave length of interest; (2) there are at least 8 elements for each perforation; (3) the mesh around the perforation is finer than the rest of the acoustic domain matching locally the perforation mesh.

In the model, triangular elements are used for surfaces and boundaries whereas tetrahedral elements are used for volumes to mesh the numerical domain. An example of the meshed geometry is shown in Figure 5.3.

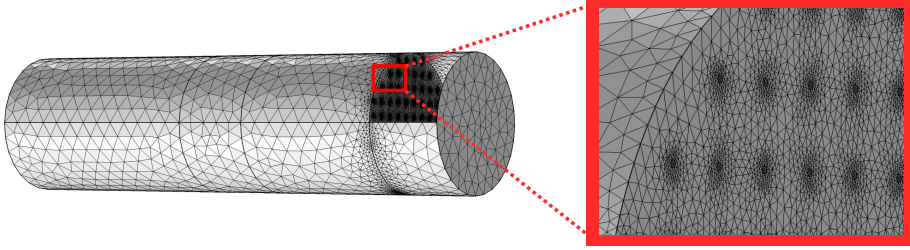


Figure 5.3: The example of typical meshing of the numerical geometry. The meshing is performed with COMSOL's built-in physics controlled meshing tool and some part of the side surface is left open to show the meshing around the perforations.

The study for mesh convergence is discussed in Appendix B.

5.3.4 Estimation of the absorption coefficient

In this study, the absorption coefficient is represented by β in order not to confuse it with the resistive end-correction coefficient α . To calculate the absorption coefficient β , the two-microphone method by Bodén and Åbom [73] is applied to the numerical model. Two microphone positions, z_{m1} and z_{m2} are chosen on Domain ① and the pressure values are averaged by section at these two positions in z as \hat{p}_{m1} and \hat{p}_{m2} . Using these pressure readings, wave decomposition is performed to obtain complex amplitudes of the right and left travelling pressure waves, \hat{p}^+ and \hat{p}^- respectively. Therefore, the absorption coefficient is calculated as

$$\beta = 1 - \left| \frac{\hat{p}^-}{\hat{p}^+} \right|^2. \quad (5.10)$$

5.3.5 Compensation for inviscid reactance

Since the numerical method described in this section allows one to model the perforations separately, it is referred here as the *discrete model*. On the contrary, the conventional analytical model assumes an average transfer impedance value over the plate and lumps this value to the MPP to compute the acoustic properties of the system, therefore it is referred to as the *lumped model* in the present paper. Provided that the perforations are far enough from each other, so that no interactions between perforations take place, the discrete and lumped models should provide

Table 5.1: Properties of the cases from Toyoda *et al.* [68] used for comparing the discrete and lumped models. Please see Figure 5.4 for the definition of parameters.

	Case A1	Case A2	Case A3
d_p [mm]	0.5	1.0	2.0
t_p [mm]	0.5	0.5	0.5
b [mm]	10	10	10
n_p [mm]	76	76	76
ϕ [-]	0.2%	0.8%	3.1%
D [mm]	100	100	100
L [mm]	300	300	300
L_c [mm]	50	50	50

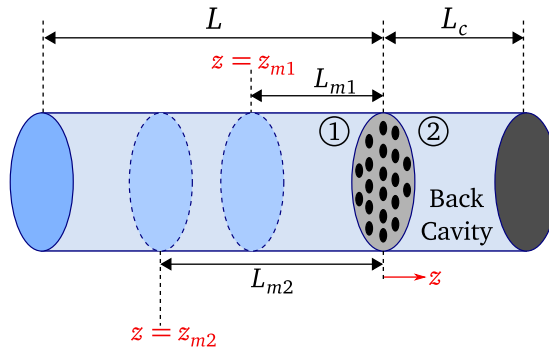


Figure 5.4: Geometric parameters of the numerical domain.

comparable results for the rigid plate. Please note that, for the rigid plate modelling, the vibro-acoustic boundary condition (Ω_S) is replaced with the sound-hard boundary condition (Ω_{z_∞}).

To verify this, three test cases are considered. The physical properties of these cases are provided in Table 5.1 and Figure 5.4.

In Table 5.1, b is the distance between the two neighbouring perforations, n_p is the number of perforations on the plate, L is the length of the impedance tube and L_c is the depth of the back cavity (see Figure 5.4). These parameters are taken from the study by Toyoda *et al.* [68].

The comparison between the absorption coefficients predicted by the lumped and discrete models for Cases A1 to A3 is given in Figure 5.5. As it can be seen

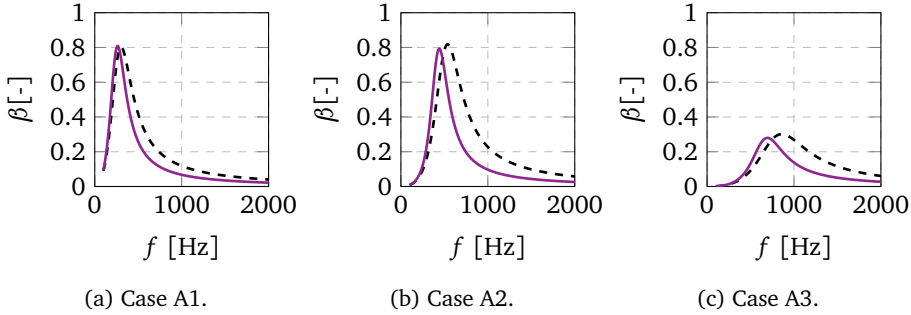


Figure 5.5: Comparison of the absorption coefficients calculated with the discrete model (—) and the conventional lumped model (- - -).

in these graphs, the discrepancy between the analytical results and the numerical ones increase from Cases A1 to A3. Considering the parameters given in Table 5.1, only perforation diameter and plate porosity values differ among the test cases.

The same discrepancy is reported by Temiz *et al.* [72] with another FE program, namely LMS Virtual.Lab [74]. Hence, the discrepancy between the predictions of the lumped and discrete models is not solver dependent.

Keeping in mind that the Helmholtz equation does not take the viscous effects into account, the frequency shift observed in Figure 5.5 is a result of reactance only. In fact, Eq. (5.3) takes a reactance (end-correction δ_s) into account describing the inertia of the non-uniform acoustic flow around the opening of the perforations. The solution of the Helmholtz equation should therefore disregard this effect. To eliminate this inviscid reactance contribution (δ_H) by the Helmholtz equation, its value is estimated and subtracted from Eq. (5.3). This subtraction can be performed under the assumptions that the acoustic flow is almost incompressible around the perforations and that acoustic impedance can be superposed due to the linearity of the system.

This new expression is referred as the *modified transfer impedance* and should be used at the imposed transfer impedance boundaries in the proposed numerical model. To calculate the inviscid reactance contribution, a set of simulations have been carried out. The numerical domain for this set of simulations is almost identical to the one described so far in this paper. The schematic description of the numerical domain used in this parametric study is given in Figure 5.6 and the parameters investigated are provided in Table 5.2. By examining Figure 5.6, the differences can be noted: a single orifice is modelled (instead of an MPP) and the

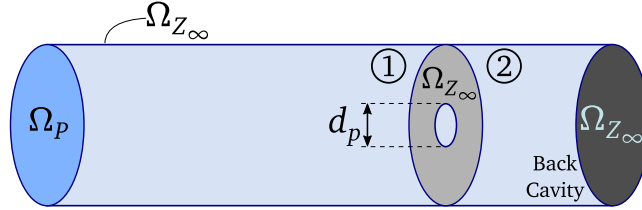


Figure 5.6: Schematic representation of the numerical geometry used in the parametric study for calculating the inviscid reactance contribution of an orifice.

Table 5.2: The parameters used in simulations to calculate the inviscid reactance contribution from the Helmholtz equation.

Porosity (ϕ) [-]	Perforation Diameter (d_p) [mm]	Frequency (f) [Hz]
0.1%	0.5	200
0.2%	1.0	1000
0.4%	2.0	2000
0.8%	4.0	
1.6%		
3.2%		
5.0%		

plate is modelled as a rigid boundary. Since it is a basic acoustic model, the meshing is performed by the built-in meshing tool by COMSOL. The mesh size is selected as the *Extremely Fine* level, which provides the finest grid in the numerical domain. Using the results from this numerical model, a parametric study is performed. The results are represented in terms on non-dimensional parameters so that they can be generalized.

The single orifice illustrated in Figure 5.6 is modelled with the Acoustic module of COMSOL Multiphysics in frequency domain. Therefore no viscous effects are taken into consideration. As a result, the acoustic reactance of the orifice in Figure 5.6, $\Re\{Z_t\}_H$, is the inviscid reactance contribution. Please note that subscript H represents the word *Helmholtz* and indicates the inviscid contribution. This parameter is non-dimensionalized by normalizing it as proposed by Ingard [15]

$$\delta_H = \frac{2\Re\{Z_t\}_H}{\rho_0 \omega d_p}. \quad (5.11)$$

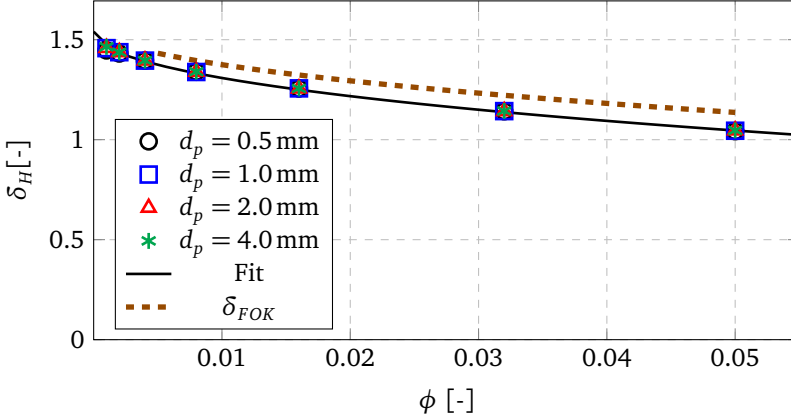


Figure 5.7: The change of inviscid reactive end-correction coefficient with respect to the porosity. For $0.5 \text{ mm} \leq d_p \leq 4.0 \text{ mm}$, the perforation diameter has negligible effect on δ_H .

From Table 5.2, simulations are run for $7 \times 4 \times 3 = 84$ different parameter combinations. Among these combinations, the effect of frequency change between the same porosity and perforation diameter values are found to be less than 1% for δ_H , therefore the number of points to be investigated is reduced to 28 by taking an average value of the three frequency values of the same combination. The resulting 28 data points are plotted with respect to porosity in Figure 5.7.

It is evident from Figure 5.7 that the inviscid reactive end-correction δ_H only depends on the porosity. Even for various diameter values from 0.5 mm to 5.0 mm, the same δ_H value is found for the same porosity. Hence, to estimate the non-dimensional inviscid reactance, a fit which is a function of porosity only is proposed such as

$$\delta_H = 0.85\phi - 2.40\sqrt{\phi} + 1.54, \quad 0 \leq \phi \leq 1. \quad (5.12)$$

The quality of the fit given in Eq. 5.12 is $r^2 = 0.9998$, where $(1 - r^2)$ is the variance of the fit.

The fit is calculated in such a way that when the porosity is unity, in other words when the orifice size is equal to the duct diameter, $\delta_H = 0$ is satisfied. On the other hand, when the porosity becomes very small, the fit value approaches to 1.54. This value is comparable to the theoretical limit value calculated by Pierce [36] who obtains the analytical value for the low frequency limit of the length of the oscillating fluid mass at a circular orifice in an infinite (thin) baffle plate as $\pi/2 = 1.57$

times the orifice radius. Therefore in the very low porosity limit, the fit proposed in Eq. (5.12) leads to an error of no more than 2% compared to the theoretical limit of Pierce [36].

Moreover, Tayong *et al.* [75] discuss the hole interaction effect on the acoustic reactance with the help of Fok's function which also depends on porosity. Their correction is compared to the fit given in Eq. (5.12) for $0.005 \leq \phi \leq 0.05$ and a very similar trend is observed between the two calculations (see Figure 5.7). Therefore, we conclude that using the expression given in Eq. (5.12) for compensating the excess reactance should be adequate.

Finally, the modified transfer impedance Z_t^* , which is used in the imposed transfer impedance boundary layer in the discrete numerical model, is updated as

$$Z_t^* = j\omega t_p \rho_0 \left[1 - \frac{2}{Sh\sqrt{-j}} \frac{J_1(Sh\sqrt{-j})}{J_0(Sh\sqrt{-j})} \right]^{-1} + 2\alpha_s R_s + j(\delta_s - \delta_H)\omega\rho_0 \frac{d_p}{2}. \quad (5.13)$$

In Figure 5.8, the comparison between the predicted absorption coefficient for the conventional analytical model and the discrete model which uses the modified transfer impedance is made. For each Case, the relative percentage error is calculated as

$$\epsilon_{f\%} = \frac{|f_{peak-lm} - f_{peak-dm}|}{f_{peak,m}} 100\%, \quad (5.14)$$

where f_{peak} is the frequency where the absorption peak is observed, subscripts lm and dm represent the lumped and discrete models respectively. The calculated relative percentage errors are presented in Figure 5.8, also.

It can be seen that the discrepancy between the two prediction is practically eliminated when the modified transfer impedance proposed in Eq (5.13) is applied in the discrete model.

5.4 Validation of the Discrete Numerical Model and Discussions

The validation of the discrete numerical model is partly performed in the previous chapter by the parametric study for evaluating the contribution of the inviscid reactance. Figure 5.8 provides the comparison between the discrete and lumped models of the acoustic absorption of an MPP backed by a cavity for rigid plates. In this section, the predicted absorption coefficients for two rigid plate configurations are compared to measured absorption coefficients and then the effect of

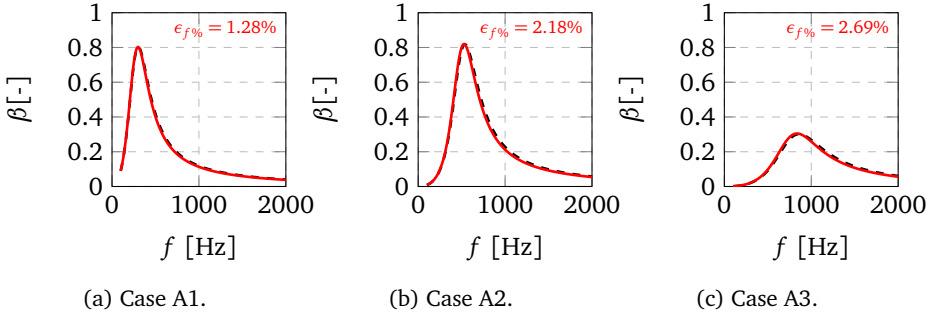


Figure 5.8: Comparison of the absorption coefficients calculated with the discrete model using the modified transfer impedance (—) and the conventional lumped model (---).

vibro-acoustically coupled system is discussed by comparing results from both fundamental analytical models and measurements by Toyoda *et al.* [68] with the discrete numerical model.

5.4.1 Rigid plate

The impedance tube used for the experimental validation of the discrete numerical model is the same set-up described in the study by Temiz *et al.* [24]. The physical properties of the samples used in this validation is provided in Table 5.3.

The measurements are performed in the frequency interval of $100\text{ Hz} \leq f \leq 700\text{ Hz}$. The experimental and numerical results are plotted together in Figure 5.9. As it can be seen from the plots, the numerical model successfully captures the general absorption behaviour of the rigid MPPs.

The samples defined in Cases A4 and A5 have already been used in an earlier study by Temiz *et al.* [34] and they are reported to have some uncertainties in the perforation geometry. The perforations on these samples are manufactured by drilling and some of them have more triangular shape than circular. The reason for the frequency shift between the discrete numerical model and the measurements in Figure 5.9 can be this uncertainty.

Table 5.3: Properties of the samples used in the experimental validation of the discrete numerical model for the rigid plate case. The measurements are carried out with the impedance tube set-up described by Temiz *et al.* [24].

	Case A4	Case A5
d_p [mm]	0.8	1.6
t_p [mm]	1.0	1.6
b [mm]	8	15
n_p [-]	29	7
ϕ [-]	0.7%	0.7%
D [mm]	50	50
L [mm]	150	150
L_c [mm]	20	20
Material	Brass	Brass

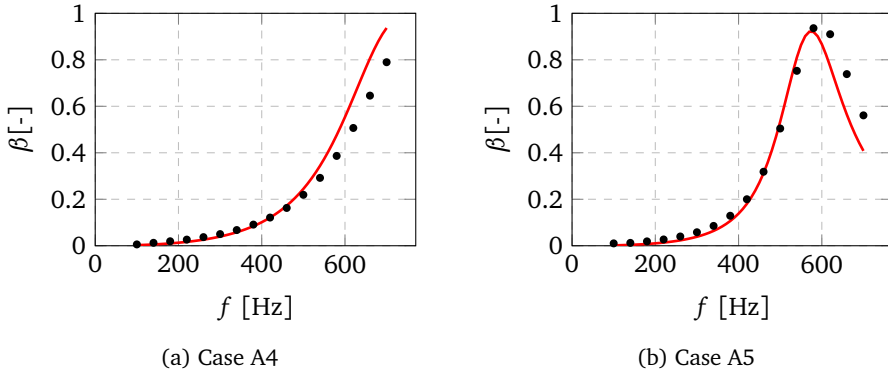


Figure 5.9: Comparison between the (original) experiments (\bullet) and numerical model (—) with modified transfer impedance in Eq. (5.13).

Table 5.4: Parameters defining the validation test cases. Except from the density, they are taken from the study by Toyoda *et al.* [68] who reports the sample material as PVC. The density value is taken from the material library of COMSOL.

	Case VA0	Case VA1	Case VA2	Case VA3
d_p [mm]	N/A	0.5	1.0	2.0
t_p [mm]	0.5	0.5	0.5	0.5
b [mm]	N/A	10	10	10
n_p [mm]	0	76	76	76
ϕ [-]	0	0.2%	0.8%	3.0%
D [mm]	100	100	100	100
L [mm]	300	300	300	300
L_c [mm]	50	50	50	50
E [N/m ²]	3×10^9	3×10^9	3×10^9	3×10^9
η [-]	0.03	0.03	0.03	0.03
ν [-]	0.3	0.3	0.3	0.3
ρ [kg/m ³]	1760	1760	1760	1760

5.4.2 Flexible plate

To validate the discrete numerical model in terms of vibro-acoustic coupling, the test cases from Toyoda *et al.* [68] are used and their properties are provided in Table 5.4. To include the structural effects into the model, the f-MPP boundary condition is applied on the plate (See Figure 5.2 and Eq. (5.8)).

Although the test cases are clearly defined in the study by Toyoda *et al.* [68], the density of the flexible plate is not explicitly provided. Instead, the material used for manufacturing the plates is reported as rigid PVC (*polyvinyl chloride*). As a result, the simulations are carried out using the PVC material which is already in the material library of COMSOL ($\rho_{PVC} = 1760 \text{ kg/m}^3$).

Comparison with fundamental analytical models

First, the eigen-frequencies of the flexible plate Case VA0 is computed analytically and compared with numerical results. The theoretical modes of a circular plate whose circumference is clamped is calculated by [76]

$$J_0(\gamma_m)I_1(\gamma_m) + I_0(\gamma_m)J_1(\gamma_m) = 0, \quad (5.15)$$

Table 5.5: The first four vacuum eigen-frequencies of the circular plate whose circumference is clamped. The plate properties are given in Table 5.4 for a non-perforated plate in vacuum.

γ_m [-]	$\Re\{f_m\}$ [Hz]
3.1962	129
6.3064	500
9.4395	1121
12.5771	1990

where subscript m denotes the m^{th} natural mode and

$$\gamma_m = \frac{D}{2} \sqrt{2\pi f_m \left(\frac{\rho_p t_p}{D_p} \right)^{0.5}}. \quad (5.16)$$

Hence, the eigen-frequencies of a circular plate whose circumference is clamped is found by solving for γ_m in Eq. (5.16). The first four solutions of this equation and corresponding vacuum eigen-frequencies are given in Table 5.5.

The eigen-frequencies calculated with the simple analytical approach are compared with the simulation results in Figure 5.10. It is seen that the first eigen-frequency in the simulation is significantly larger compared to the analytical calculations. This is due to the additional stiffness added by the air volume in the back cavity. This is verified by carrying out another simulation where the back cavity wall is modeled as a sound-soft boundary, *i.e.* $\hat{p}_2|_{z=L_c} = 0$. Doing so it is ensured that the air in the back cavity can flow through the back and forth through this sound soft boundary and does not exert an additional stiffness on the plate. In other words, by changing the boundary condition, the vacuum modes of the plate described in case VA0 is simulated. The results of this updated simulation validate that the structural properties of the plate is captured successfully in the simulations.

The second basic model is the Helmholtz resonator. The eigen-frequency of a Helmholtz resonator can be calculated by [36]

$$f_H = \frac{c_0}{2\pi} \sqrt{\frac{S_n n_p}{V_0 L_{eq}}}, \quad (5.17)$$

where $S_n = d_p^2 \pi / 4$ is the cross-section of the perforation, V_0 is the volume of the backing cavity and $L_{eq} = t_p + 1.70(S_n / \pi)^2$ is the equivalent orifice length. In Table 5.6, the corresponding Helmholtz frequencies of the simulation cases are given.

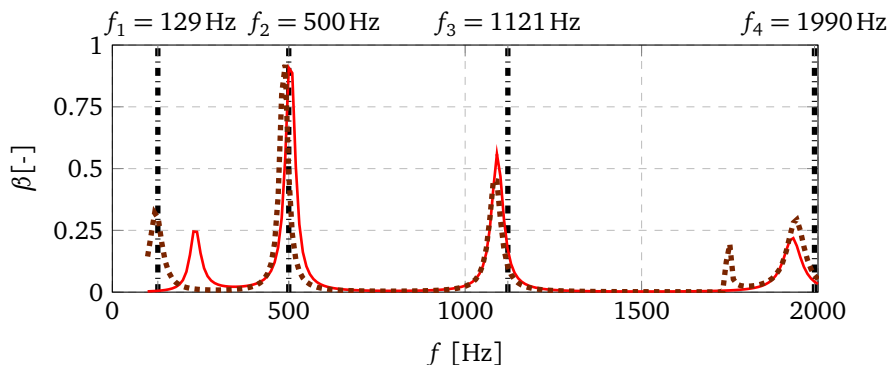


Figure 5.10: The comparison between a simple circular plate and the simulations of Case VA0: (---) Theoretical eigen-frequencies, (—) simulation with vibro-acoustic coupling, and (.....) simulation with vibration only.

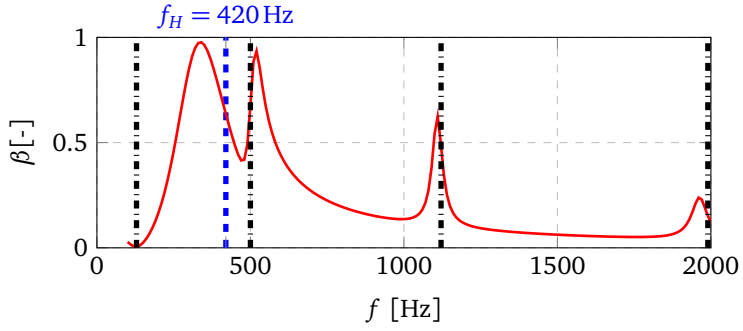
Table 5.6: Corresponding Helmholtz frequency of Cases VA1, VA2 and VA3 (see Table 5.4).

Simulation Case	f_H [Hz]
VA1	420
VA2	682
VA3	1051

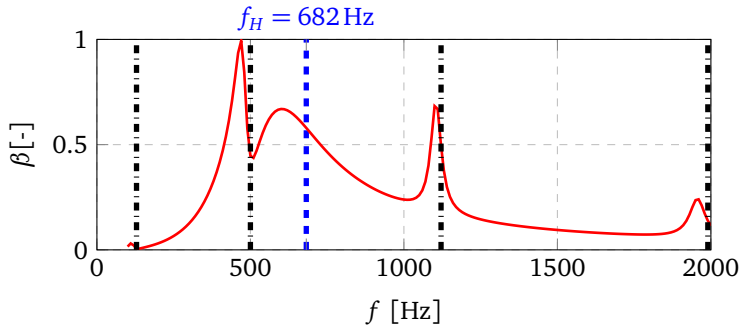
The calculated Helmholtz frequency values using the analytical expression given in Eq. (5.17) is marked in the absorption coefficient vs. frequency graphs for Cases VA1, VA2 and VA3 in Figure 5.11.

First point to observe in Figures 5.10 and 5.11 is that the absorption peaks originating from structural vibrations are *sharper* and have a more narrow-band character. On the other hand, the peaks related to the acoustic modes are effective over a wide frequency band. This is due to the difference in damping mechanisms between the structural and acoustic systems. Since the acoustic system benefits from the viscous damping, which dissipates more energy in case of high particle velocity, the absorption caused by the air particles passing through the perforations expands over a wider frequency bandwidth.

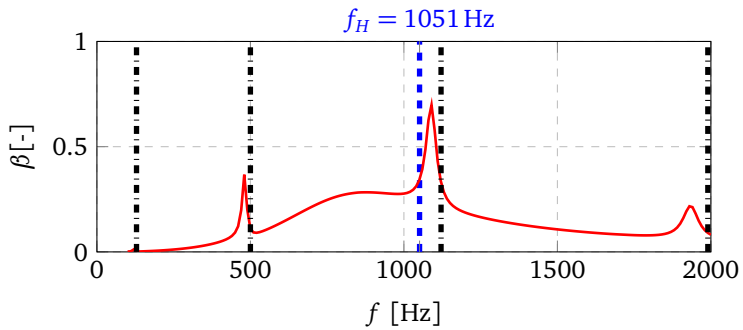
The key observation from Figure 5.11 is that all of the the calculated Helmholtz frequencies (see Table 5.6) are higher than the smooth and wide-band peaks in the



(a) Case VA1



(b) Case VA2



(c) Case VA3

Figure 5.11: Cases VA1 (a), VA2 (b), and VA3 (c). The corresponding Helmholtz frequencies are marked on top of the graphs (■-■-■). Additionally, the first three vacuum eigen-frequencies of the plate are also shown on the graphs (---).

absorption curves, which originate from the sound dissipation due to the back cavity volume and viscous friction in the vicinity of the perforations. This systematic shift to the lower frequencies result from the added mass of the flexible plate described by Cremer [77]. Unlike cases with rigid ones, in non-rigid cavities the compressed air not only pushes out the particles through the perforation, but exerts pressure on the flexible plate also. Therefore, the eigen-frequency corresponding to the fundamental acoustic mode of a non-rigid cavity is referred as *the first cavity resonance frequency*.

Comparison with experimental results

The validation of the discrete numerical model is completed by comparing the predicted absorption coefficient for all cases given in Table 5.4 with the measurements provided by Toyoda *et al.* [68] in Figure 5.12.

As shown in Figure 5.12, the discrete numerical model represents the general behaviour of a vibro-acoustic system successfully. Although, there is a shift between the numerical simulation and experiment results due to the difference in the material properties. When the density is adjusted as a fit parameter to the value $\rho_{PVC} = 1300 \text{ kg/m}^3$, the shift between the numerical simulations and the measurements performed by Toyoda *et al.* [68] is significantly reduced.

5.5 Parametric Study Example

To illustrate that the described numerical model can be used as a tool for parametric studies, the influence of plate thickness and distribution of the parameters are investigated in this section. For the parametric study, the density of the flexible plate material does not matter provided that it is kept constant throughout all the simulations. Hence, the default value from the material library of COMSOL[®] is used ($\rho_{PVC} = 1760 \text{ kg/m}^3$).

5.5.1 Influence of Plate Thickness

The thickness of a flexible plate is an important parameter for coupled vibro-acoustic behaviour since its third power is directly related to the flexural rigidity of the plate. Hence, a thinner plate results in lower structural acoustic peaks in the system. Moreover, for the same acoustic excitation, the amplitude of the plate vibrations is increased with the decreasing plate thickness. Depending on the shape and

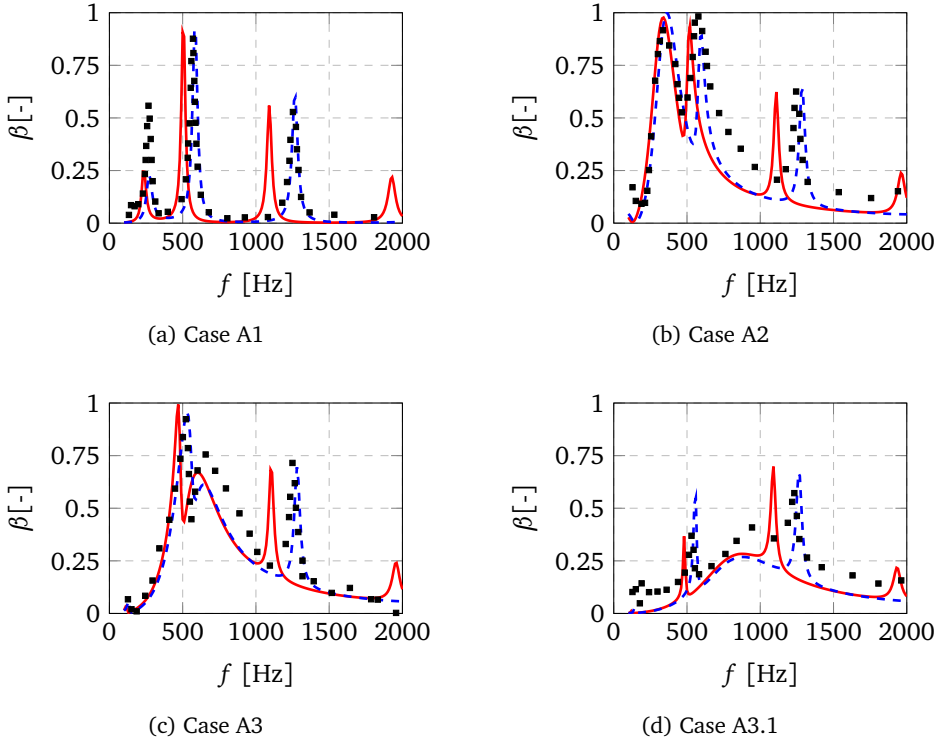


Figure 5.12: Comparison between the discrete numerical model (—) and measurements by Toyoda *et al.* [68] (■). Additional simulations with the density as fit parameter adjusted to $\rho_{PVC} = 1300 \text{ kg/m}^3$ instead of the density reported in the COMSOL library $\rho_{PVC} = 1760 \text{ kg/m}^3$ are shown as (- -).

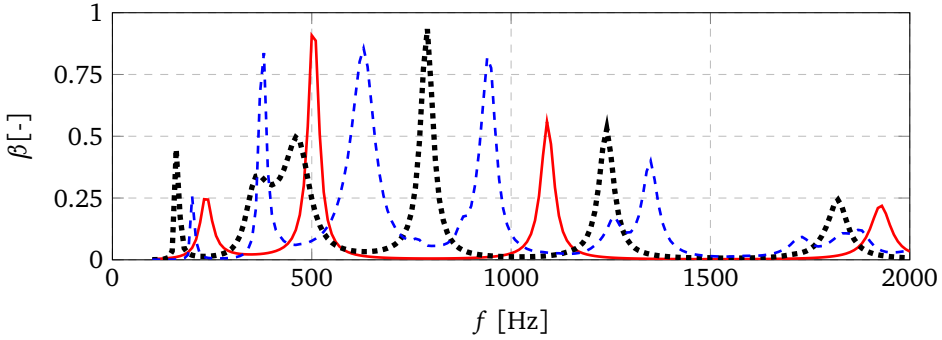


Figure 5.13: The plate thickness effect for a plate with no perforations: (—) $t_p = 0.5$ mm, (••••) $t_p = 0.2$ mm, and (---) $t_p = 0.1$ mm.

boundary conditions of the plate, it is not straightforward to assess the exact outcome of the thickness change on acoustic response. As a result, the model described here can be used to obtain some insight.

For this parametric study, there are three base cases: VA0, VA2 and VA4. The properties of the first two base cases are already provided in Table 5.4 and for Case VA4, one can refer to Table 5.7. The distinguishing properties for these base cases are that Case VA0 has no perforations, Case VA2 has perforations of 1 mm in diameter and Case VA4 has perforations whose diameter is 0.3 mm. As a result this variety of diameters gives a general idea for the typical MPP range.

Besides the aforementioned three base cases, all of which have thickness of 0.5 mm, 6 additional cases are designed to investigate the effect of thickness in vibro-acoustic coupling of f-MPPs. Each base case is related to 2 additional case, whose properties only differ in terms of thickness. The detailed list of the parameters of these additional cases and VA4 is given in Table 5.7.

The first observation that can be made from Figures 5.13-5.15 is that, the presence of micro perforations increases the absorption characteristic of the flexible plate drastically in the frequency span of interest ($100 \text{ Hz} \leq f \leq 2000 \text{ Hz}$). Plates with micro-perforations provide a more wideband absorption compared to the plates without. Moreover, even the structural absorption peaks becomes higher and wider because of the friction losses due to the fluid movement through the perforations.

Another observation is that, the results from the simulations are in harmony with the expectations mentioned earlier: The thinner the plate becomes, towards the lower frequencies the plate eigen-frequencies move. This is visible for all three

Table 5.7: Parameters defining the parametric study test cases for effect of thickness.

	Case VA0	Case VA0-1	Case VA0-2
d_p [mm]	N/A	N/A	N/A
t_p [mm]	0.5	0.2	0.1
b [mm]	N/A	N/A	N/A
n_p [mm]	0	0	0
ϕ [-]	0%	0%	0%
D [mm]	100	100	100
L [mm]	300	300	300
L_c [mm]	50	50	50
E [N/m ²]	3×10^9	3×10^9	3×10^9
η [-]	0.03	0.03	0.03
ν [-]	0.3	0.3	0.3

	Case VA2	Case VA2-1	Case VA2-2
d_p [mm]	1.0	1.0	1.0
t_p [mm]	0.5	0.2	0.1
b [mm]	10	10	10
n_p [mm]	76	76	76
ϕ [-]	0.8%	0.8%	0.8%
D [mm]	100	100	100
L [mm]	300	300	300
L_c [mm]	50	50	50
E [N/m ²]	3×10^9	3×10^9	3×10^9
η [-]	0.03	0.03	0.03
ν [-]	0.3	0.3	0.3

	Case VA4	Case VA4-1	Case VA4-2
d_p [mm]	0.3	0.3	0.3
t_p [mm]	0.5	0.2	0.1
b [mm]	10	10	10
n_p [mm]	76	76	76
ϕ [-]	0.07%	0.07%	0.07%
D [mm]	100	100	100
L [mm]	300	300	300
L_c [mm]	50	50	50
E [N/m ²]	3×10^9	3×10^9	3×10^9
η [-]	0.03	0.03	0.03
ν [-]	0.3	0.3	0.3

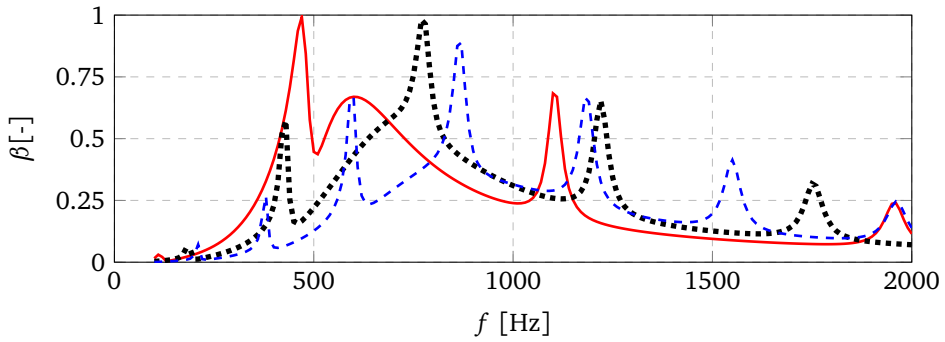


Figure 5.14: The plate thickness effect for a plate with $d_p = 1.0$ mm: (—) $t_p = 0.5$ mm, (••••) $t_p = 0.2$ mm, and (---) $t_p = 0.1$ mm.

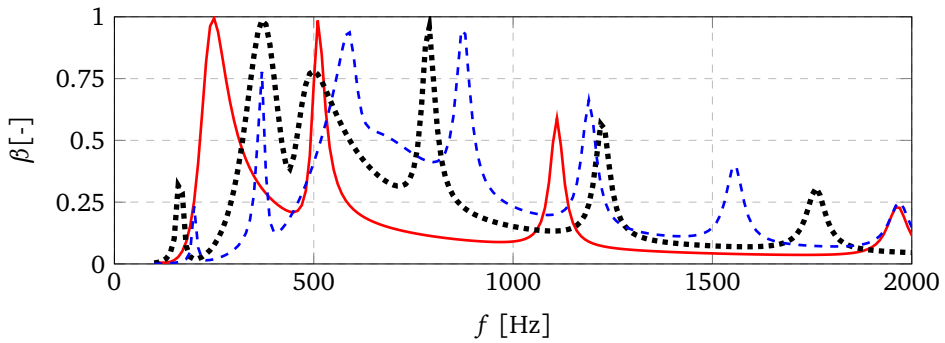


Figure 5.15: The plate thickness effect for a plate with $d_p = 0.3$ mm: (—) $t_p = 0.5$ mm, (••••) $t_p = 0.2$ mm, and (---) $t_p = 0.1$ mm.

Table 5.8: Calculated Helmholtz frequencies of Test Cases VA2, VA2-1, VA2-2, VA4, VA4-1 and VA4-2.

	VA2	VA2-1	VA2-2	VA4	VA4-1	VA4-2
f_H [Hz]	682	757	789	283	355	395

set of cases. Nevertheless, commenting on the Helmholtz frequency of the system is not that straightforward. For Test Cases VA0, VA0-1 and VA0-2, the Helmholtz frequency is not defined since there are no perforations; yet, for the remaining cases, the Helmholtz frequency values are calculated via Eq. (5.17) and given in Table 5.8.

The expected Helmholtz frequencies given in Table 5.8 increase as the plate becomes thinner. As mentioned earlier in the chapter, the Helmholtz frequency is valid for rigid-cavities. The first cavity resonance frequency for the non-rigid cavity is always lower than the calculated Helmholtz frequency. However, this non-rigid cavity resonance frequency is related to the Helmholtz frequency and the change in the latter gives idea about the former one.

The decrease in plate thickness means that the amount of oscillating mass through the perforation decreases. Since the volume in the back cavity does not change, the decrease in oscillating mass results with an increase in the first cavity resonance frequency. Moreover, the thinner the plate is, the less amount of plate mass couples with the acoustic mode in the cavity. Thus this is another reason for the first cavity mode to increase.

As the plate thickness decrease, the sound absorption mechanism by the plate vibration becomes more dominant for two reasons: (1) The plate displacements increase; (2) the viscous losses are reduced. Owing to these two reasons, the smooth and wide-band acoustic peaks become harder to notice in the absorption curves in Figures 5.14 and 5.15. Nevertheless, the change in the first cavity resonance frequencies can still be noticed between the cases with $t_p = 0.5$ mm and $t_p = 0.2$ mm.

5.5.2 Influence of Distribution of the Perforations

The discrete numerical model described in this chapter defines each perforation separately. Thus, it is possible to treat the perforation distribution as an additional parameter in MPP design. In this section, the acoustic response of several f-MPPs with different perforation distributions are compared. This time, the parametric study is based on test cases VA2-1 and VA4-1 (see Table 5.7). The essential differ-

Table 5.9: Geometrical parameters of the test cases used for investigating the perforation distribution on an f-MPP. Structural properties of the flexible plates are the same as previous test cases.

	VA2-1_D0	VA2-1_D1	VA2-1_D2
d_p [mm]	1	1	1
t_p [mm]	0.2	0.2	0.2
b [mm]	10	$3 \times d_p$	$3 \times d_p$
n_p [-]	76	79	72
ϕ [-]	0.8%	0.8%	0.7%
D [mm]	100	100	100
L_c [mm]	50	50	50

	VA4-1_D0	VA4-1_D1	VA4-1_D2
d_p [mm]	0.3	0.3	0.3
t_p [mm]	0.2	0.2	0.2
b [mm]	10	$3 \times d_p$	$3 \times d_p$
n_p [-]	76	79	72
ϕ [-]	0.07%	0.07%	0.06%
D [mm]	100	100	100
L_c [mm]	50	50	50

ence between VA2-1 and VA4-1 is the perforation diameter. The properties of the new cases are given in Table 5.9 and the corresponding perforation distributions are illustrated in Figure 5.16.

The absorption coefficient curves calculated using these test cases are given in Figure 5.17.

Comparing the two sets of simulations in Figures 5.17, it is seen that the set of cases with smaller perforation diameter (Figure 5.17b) have stronger and more wide-band absorption peaks compared to the set with larger perforations (Figure 5.17a). This is due to the difference in the viscous forces acting on the air particles passing through the perforations. The corresponding Shear number Sh is given at the top of the horizontal axis to quantify this effect. The smooth wide-band absorption peaks are visible where $Sh \approx 1$, where the Stokes layer is thick enough to occupy the entire perforation cross-section.

The perforation distributions illustrated in Figures 5.16b and 5.16e are chosen to be central since the largest displacements take place in the central area of a circular

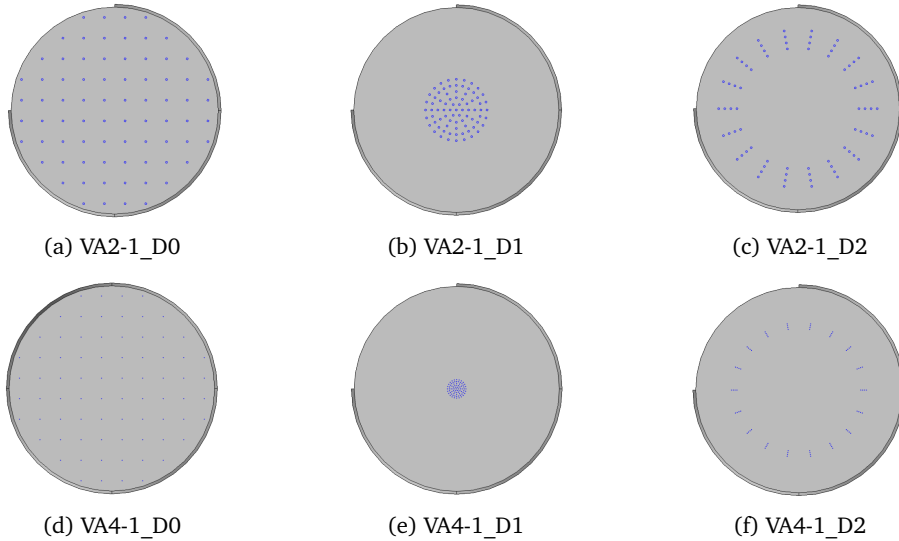


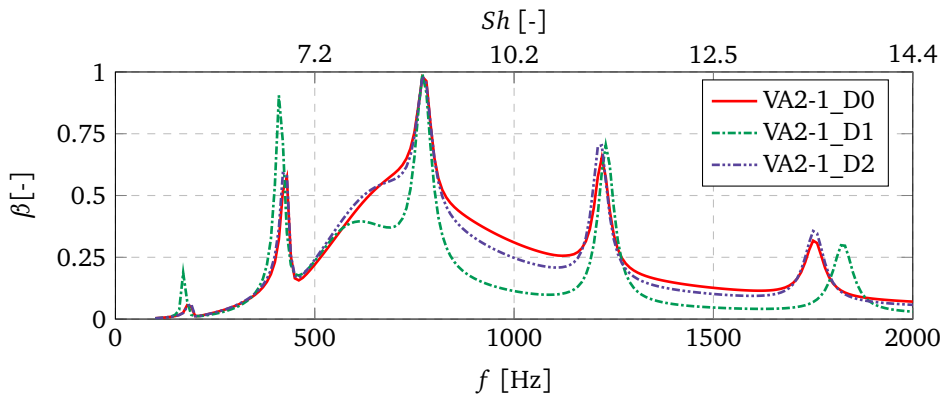
Figure 5.16: Perforation distributions of the cases described in Table 5.9.

plate whose periphery is fixed. Positioning all of the perforations in this central area, it was aimed to maximize the effect of the plate vibrations on the velocity of the particles that passes through the perforations. To minimize the inter-perforation coupling effects, the perforations are located by a minimum distance of $3d_p$ away from each other.

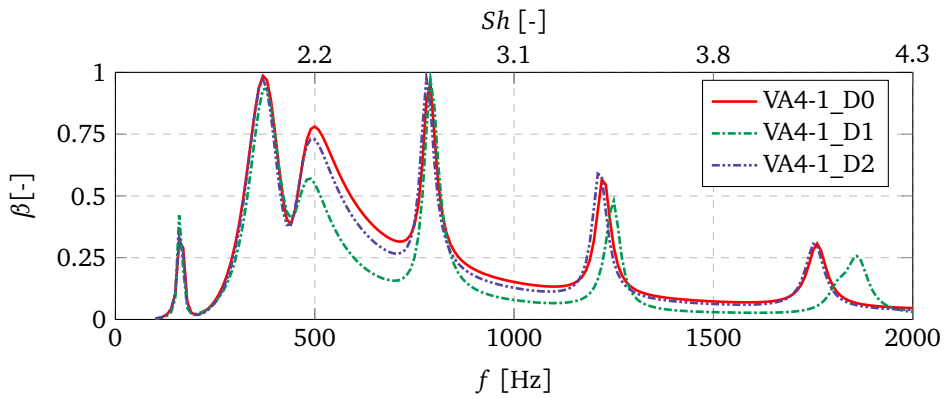
The comparison of the absorption coefficients of cases having central distribution (Cases VA2-1_D1 and VA4-1_D1) to the ones with uniform distribution (Cases VA2-1_D0 and VA4-1_D0) shows that the sound absorption is increased in the lower structural modes, but does not have large effects in the higher ones. Moreover, there is an overall decrease in absorption coefficient for test cases with central distribution.

The overall decrease in the absorption coefficient is also visible in the peripheral distribution (Cases VA2-1_D3 and VA4-1_D2), nevertheless the effect is smaller compared to the central distribution.

In Figure 5.18 the amplitude of the average particle velocity in a perforation, $|\bar{u}_p|$ is given for different distributions. For both of the cases, the difference between the uniform distribution and the central distribution is the largest. Since the viscous dissipation is related with the particle velocity, this difference explains the overall



(a) Test cases based on VA2-1.



(b) Test cases based on VA4-1.

Figure 5.17: The effect of perforation distribution on absorption coefficient for (a) Cases based on VA1, (b) Cases based on VA4. The major difference between these sets of cases is the perforation diameter (see Table 5.9 and Figure 5.16).

decrease in the absorption coefficient.

Since the plate displacement decreases towards the periphery in a circular plate whose circumference is fixed, the difference from the uniform distribution is less for cases VA2-1_D2 and VA4-1_D2 in terms of \bar{u}_p value. Thus, the decrease in particle velocity is the main reason for the overall drop in the viscous dissipation and absorption coefficient.

5.6 Conclusions

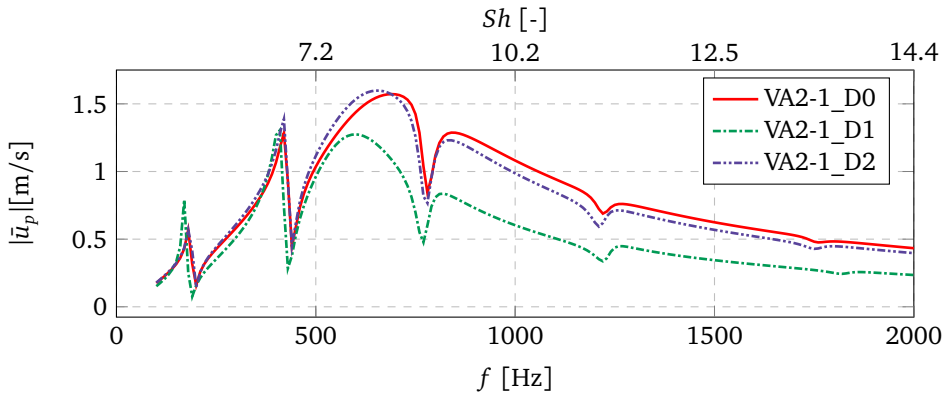
A new, efficient numerical model for estimating the absorption characteristics of flexible micro-perforated plates (f-MPPs) is presented. The model couples the linear acoustics with the shell plate theory. Specifically, the flexible plate is assumed as a shell domain and the micro-perforations are defined separately as imposed transfer impedance boundaries on this domain. The calculation of the transfer impedance value of a single perforation is performed by relations provided by Temiz *et al.* [24].

Since each perforation is represented separately, the proposed model is referred to as the *discrete* numerical model. During the model building it is observed that the Helmholtz solver takes the area changes into account, hence inserting additional reactance to the modelled system. This additional reactance is calculated for several porosity values and a correction to the transfer impedance expression proposed as a part of the numerical model.

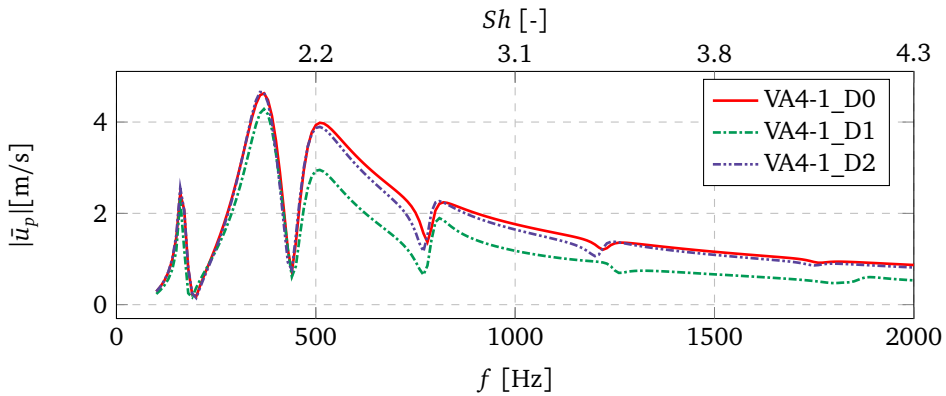
The validation of the discrete numerical model is performed by comparing it to the experiment results. The experiment results from Toyoda *et al.* [68] is used for the validating the vibro-acoustic coupling of the discrete numerical model. Good agreement is achieved between the experimental and numerical results.

The proposed method enables one to treat perforation position as an additional variable. As a result, the effect of non-uniform perforation distribution can be investigated for design purposes. Moreover, even though only circular f-MPPs are studied in this paper, it is possible to use the same model for all types of plate geometries. The model has been used here with impedance of perforations with square edges. The effect of modified edge geometry can be taken into account as proposed by Temiz *et al.* [24].

Some examples of a parametric study using the discrete model is also provided by changing the plate thickness and spatial perforation distribution. For these parametric study cases, the change in flexible plate thickness has a more drastic effect than the perforation distribution. When thickness is changed, the eigen-frequencies of the plate is altered, thus the coupling mechanism is changed completely.



(a) Test cases based on VA2-1.



(b) Test cases based on VA4-1.

Figure 5.18: Comparing the absolute value of the average particle velocity in the perforations for different distributions: (a) Cases based on VA2-1, (b) Cases based on VA4-1. For the complete parameter list and distributions, please see Table 5.9 and Figure 5.16, respectively.

On the other hand, since the typical perforation size and the porosity of an f-MPP is very small compared to the size of the plate, the perforation distribution is expected to have negligible effect on the structural properties. Nevertheless, the average particle velocity in the perforations changes with the distribution. This alters the acoustic properties of the flexible plate. To study such complex problems the numerical model proposed here can be advantageous since, (1) the model uses basic acoustic and shell modules which is found commonly in many commercial FE softwares; (2) the viscous effects in the perforations are included in the model as boundary conditions. Hence solving Helmholtz equation in the acoustic domain is sufficient instead of Navier-Stokes. Moreover, using the shell theory results in with employing 2D meshes to model the flexible plate instead of 3D. These two features result in a significant reduction in the computation time.

Chapter 6

Conclusions and Recommendations

6.1 Conclusions

Combustion instability is a serious problem affecting the efficiency and lifetime of a combustor. The coupling between the unsteady heat release and acoustic waves in the combustors is among the main reasons for this instability [4]. One way to break this coupling is to suppress the effects of acoustic waves by absorbing them. To accomplish this task, the acoustic properties of micro-perforated plates (MPPs) are investigated in this thesis. By numerical and experimental studies, the sound absorption mechanisms for micro-perforated plates are discussed in detail. Impedance tube experiments in a semi-anechoic chamber and finite element model simulations in COMSOL Multiphysics[®] (ver. 5.0) [23] are used throughout the study.

The present thesis involves not only MPPs, but also regular perforated plates since they are also used in combustion systems [78]. As a result, the covered Shear number range in this thesis is $0.75 < Sh < 35$. The acoustic response of MPPs and perforated plates is examined in the linear, transition, and non-linear regimes, *i.e.* $0.05 \leq Sr \leq 100$ (please see Sections 2.2 and 3.2 for definitions of Sh and Sr).

Moreover, the effect of edge-profile on the acoustic response of a perforation is investigated. This study is carried out for both MPPs and perforated plates in the linear, transition and non-linear regimes.

MPPs and perforated plates are not handy only in combustion systems, but they are also used in architectural and room acoustics [9]. In such applications larger

plates are used, hence structural vibration of the plates plays an important role in the acoustic response of the MPPs and perforated plates. When the flexibility of the plate is included, design and optimization of such plates become a challenging task. The current thesis attempts to solve this problem by proposing a numerical method that includes the plate flexibility and the position of each perforation separately. The simulation results from the proposed model is validated with the results from literature and some theoretical limits.

On the other hand, the present thesis focuses only on the circular perforations. Slits, rectangular perforations or any other geometries are out of the scope of this thesis. Besides, all the experiments and simulations are carried out in stagnant acoustic medium, i.e. no mean flow.

The prominent conclusions that are drawn from this thesis are summarized in the rest of this section.

The end-correction coefficients do not necessarily depend on the edge profile of a perforation, yet they do depend on the Shear number. In Chapter 2, expressions for the resistive and reactive end-correction coefficients are proposed in the range $1 < Sh < 35$ [Eqs. (2.9), (2.11) and (2.12)]. These expressions are obtained for square-edge, both-sides-chamfered and inverse-chamfer edge profiles and their linear combination is used for one-side-chamfered and punched-edge profiles [Eqs. (2.13) and (2.14)]. The relative error between the linear combinations and the numerical simulations are less than 3% in the given Sh range [Figures 2.11 and 2.12].

The acoustic response of a circular MPP with a square-edge profile depends not only the Strouhal number, but also the Shear number in the transition regime, i.e. $Sr \sim \mathcal{O}(1)$. However, when $Sh > 3$, its effect becomes quite weak for this regime. Empirical correction functions are provided for the transfer resistance and reactance so that linear and non-linear regimes are linked with one expression for both transfer resistance and reactance [Eq. (3.15)].

The effect of edge-profile in perforations on the non-linear acoustic response cannot be ignored. For example, the normalized resistance [Eq. (4.13)] of both-sides-chamfered profile with $c^* = 0.08$ is 40% less than the one of the square-edge profile [Figure 4.6a]. However, when the chamfer size is tripled, the normalized resistance decreases only by 10% compared to the behaviour of the small chamfer. Therefore, the presence of a chamfer is more important than its

size in the non-linear regime. The inverse-chamfer profile behaves similarly to the square-edge profile in case of high-amplitude acoustic excitations.

The quasi-steady model fails to predict the sound absorption mechanism in the transition regime [Figures 4.8, 4.9 and Tables 4.4, 4.5]. Although it is quite a powerful tool in strongly non-linear regime [18, 57, 56], the quasi-steady approach loses its accuracy when the contribution from linear resistance and reactance to the acoustic response of an orifice is comparable to the non-linear effects ($Sr \simeq 1$). Therefore, there is a need for an improved approach to model the acoustic response of an orifice and sound generation in higher harmonics in the transition regime.

A new, efficient numerical method is proposed to calculate the absorption coefficient of a flexible MPP [Chapter 5]. This method models each perforation separately by a *patch-impedance* approach using the expressions proposed in Chapter 2. It is efficient compared to CFD models since it couples the shell plate theory [71] and the Helmholtz equation [8], which are both linear. The proposed model allows the spatial distribution of the perforations to be treated as an additional parameter in MPP design. It can be used as an optimization tool. An example of a parametric study is provided.

For a rigid MPP absorber one has at least 6 parameters taking geometrical and hydrodynamic flow parameters into account. This implies that even if only a few measurements are carried to vary each parameter, a few hundred experiments would be necessary to choose an optimal design when theoretical models are not used. The proposed models allow to determine the acoustic response in absence of mean flow for circular perforations. When the plate is flexible, flexural rigidity (D_p), plate geometry and spatial distribution of the perforations are also needed to be taken into account. The findings of this study are used for building an engineering tool which can be used for designing a flexible MPP absorber and optimizing its acoustic performance. In particular the effect of individual perforation geometry and spatial distribution can be considered.

6.2 Recommendations

By some minor adjustments, the numerical model proposed in Chapter 5 can be used for designing efficient flexible MPPs for room acoustics. These adjustments

are:

- **Changing the geometry of the flexible plate:** Only circular plates are used in the parametric study examples in Chapter 5. However, there is no restriction about the flexible plate geometry in the model. On the contrary, each geometry have different mode shapes which can couple with the acoustic response of the perforations. Therefore, it is possible to carry out more parametric studies with different plate geometries.
- **Changing the geometry of the perforation:** The perforations are represented as separate boundaries and the governing boundary condition is described by the transfer impedance for a single perforation minus the reaction due to porosity. If the transfer impedance expression for a certain perforation geometry (slit, rectangular, triangular, etc.) is known, implementing this into the discrete numerical model [Chapter 5] is just updating an equation.

On the other hand, before using MPPs in combustion systems efficiently, further study is required in following aspects:

- **The effect of mean flow:** The current thesis does not take the mean flow into consideration. However, combustion systems have main flow which cannot be neglected. In such cases, perforated plates are subjected to grazing and / or bias flows. The effect of mean flow on the acoustic response of MPPs should be investigated.
- **Vibro-acoustic coupling in the non-linear regime:** Since combustion systems can produce acoustic waves which have amplitudes large enough to cause mechanical problems, they are expected to be in the non-linear regime. However the vibro-acoustic coupling theories are developed for linear regime. Investigating the effect of high intensity sound waves in vibro-acoustic coupling would be beneficial for better acoustic estimations.
- **The effect of edge-profile in the transition regime:** As discussed in Chapter 4, quasi-steady approach fails to predict the acoustic response of a perforation accurately. Therefore a study including the effect of edge profiles can fill this information gap. The study presented in Chapter 3 considers only circular MPPs with square-edge profiles.

Last but not the least, the interest in MPPs with slit geometry advances recently due to their ease of mass production and promising acoustic performance [19]. Therefore carrying out studies similar to the ones presented in the current thesis would be beneficial.

Appendices

Appendix A

Impedance Tube Set-Up

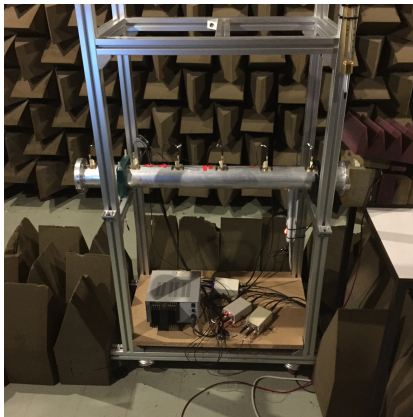
In this part, the impedance tube set-up used in Chapters 2–4 is described in detail with the precautions taken and post-processing methods applied to increase the accuracy of the measurements.

A.1 Technical Description

The impedance tube used in the measurements is a 1-meter long, cylindrical aluminum tube whose wall thickness is 10 mm and inner diameter is $D = 50$ mm. The tube has flanges at both of its ends and 6 holes along for mounting the microphones. The microphones are flush mounted into the tube with a specially manufactured mount having a curved base. The radius of mount base is the same as the inner radius of the tube in order not to create physical obstacles or cavities in the tube. In Figure A.1 the photo of the measurement setup, one of the microphones with its mount and the schematic description of the remaining components are shown. Moreover, the technical properties of the set-up are listed in Table A.1. Finally, the microphone placement on the impedance tube is given in Figure A.2.

A.2 Signal Processing Techniques for Impedance Tube Measurements

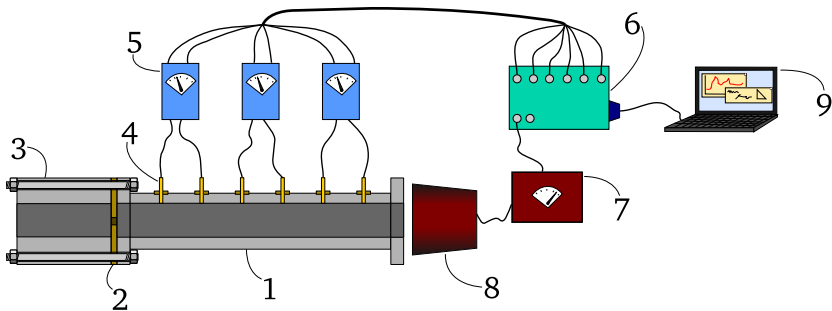
The set-up uses a custom built LabView[®] script as its data acquisition and signal processing (DASP) interface. The excitation signal sent to the loudspeaker is



(a) Photo of the setup.



(b) Microphone with its mounting.



(c) Schematic representation of the impedance tube setup components: 1-Tube, 2-Sample, 3-Tube extension, 4-Microphone, 5-Microphone amplifier, 6-A/D & D/A converter, 7-Loudspeaker amplifier, 8-Loudspeaker, 9-Analyser & signal generator (computer including the data acquisition card).

Figure A.1: The impedance tube setup (a), the microphone with the mounting (b) and the schematic representation of the components (c).

Table A.1: TBC

	Brand & Model	Specifications
(1) Tube	Generic	1-m long, aluminium, 10-mm wall thickness.
(2) Test Sample	Generic	Explained in detail in Section 4.3.2.
(3) Tube Extension	Generic	80-mm long, 50-mm inner diameter, 140-mm outer diameter, aluminium.
(4) Microphone	BSWA Tech MPA 416	Pre-polarized, 1/4" diameter, 50 mV/Pa sensitivity.
(5) Microphone Amplifier	BSWA Tech MC 102	Dual channel, 4 mA output.
(6) D/A & Converter	A/D NI BNC-2111	16 analog input and 2 analog output channels.
(7) Loudspeaker Amplifier	XXL Power Sound PA 240	Dual channel, 240W output.
(8) Loudspeaker	Dayton Audio DA115-8	Aluminum cone, 4" diameter, 60 Hz – 15 kHz, max. 40 W.
(9) Analyser & Signal Generator	NI PCIe-6361 X-Series	16 input, 2 output channels, 2 MHz input sampling rate, 2.86 MHz output sampling rate.

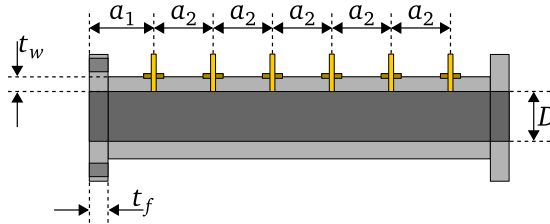


Figure A.2: Equidistant microphone placement on the impedance tube. $a_1 = 50$ mm, $a_2 = 175$ mm, $t_w = 10$ mm, $t_f = 20$ mm, and $D = 50$ mm.

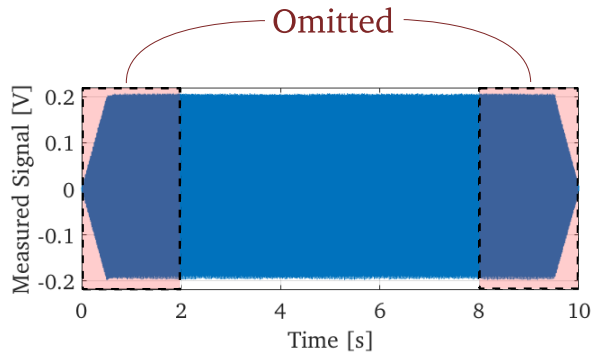


Figure A.3: A sample of the signal read by one of the microphones in the impedance tube at 120 Hz. Due to the transient effects in the beginning and at the end, first and last 2-second portions of the signal are omitted.

sampled with 20 kHz and the signals acquired from the microphones are sampled with 10 kHz. Each measurement is performed for a single frequency for 10 seconds. Since the excitation signal passes through a Planck-taper window, the beginning and the end of the read signals are smoothly goes to zero. Thus, in post-processing first and last 2 seconds of each measurement is omitted to avoid transient effects. A sample of the measurement reading is given in Figure A.3. The post processing of the data is performed separately in a custom built MATLAB[®] script. To minimize the possible measurements errors, some post-processing precautions are taken in this script. In the rest of this section, these precautions are discussed in detail.

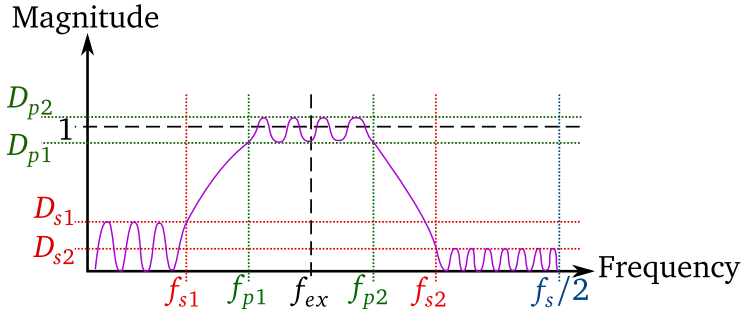


Figure A.4: The schematic drawing of the equiripple band-pass filter in frequency domain. The parameters shown here are explained in Table A.2.

A.2.1 Signal filtering

As mentioned earlier, the air in the tube is excited by a single-frequency signal, f_{ex} . Hence, the expected response is at the same frequency provided that the higher harmonics are neglected. As a result, the components of the frequencies except for the excitation frequency is considered as noise and filtered out in the post-processing. This is performed by the built-in *Filter Design and Analysis* tool of MATLAB[®]. Using this tool, a bandpass equiripple FIR filter is designed for the post-processing script. The parameters required to design this filter and the assigned values for this study are given in Table A.2 and the parameters are schematically illustrated in Figure A.4.

An example of the actual filter for 120 Hz is calculated with the parameters given in Table A.2 and its gain is showed in Figure A.5.

To avoid the phase shift problem caused by using a digital filter, the `filtfilt()` function is used for completing the filtering process. This function filters the data both forward and backward to cancel out the artificial phase shift caused by digital filtering [79].

A.2.2 Converting measurement data to frequency domain

The parameters that will be introduced later in this chapter are meaningful in frequency domain only. As a result, the measured time domain data needs to be converted to frequency domain. The most common way to perform this task is to use an FFT algorithm. Nevertheless, this method does not compensate for the possible frequency shifts in the excitation. To exclude these type of errors, a modified lock-in

Table A.2: Parameters used to design an equiripple FIR filter in the *Filter Design and Analysis* tool of MATLAB[®].

Parameter	Value	Definition
f_{s1}	$f_{ex}/2$	First band-stop frequency [Hz]
f_{p1}	$5f_{ex}/6$	First band-pass frequency [Hz]
f_{p2}	$7f_{ex}/6$	Second band-pass frequency [Hz]
f_{s2}	$3f_{ex}/2$	Second band-stop frequency [Hz]
D_{s1}	0.001	Maximum relative signal amplitude before f_{s1} [-]
D_{s2}	0.0001	Maximum relative signal amplitude after f_{s2} [-]
D_{pass}	0.0575	Band-pass ripple relative amplitude[-]
D_{p1}	$1 - D_{pass}$	Band-pass ripple minimum relative amplitude[-]
D_{p2}	$1 + D_{pass}$	Band-pass ripple maximum relative amplitude[-]
f_s	10000	Sampling frequency [Hz]
d_f	20	Filter ripple density factor [-]

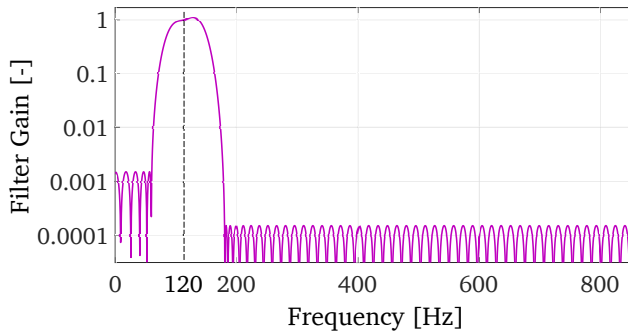


Figure A.5: The example of a filter gain computed for 120 Hz with parameters given in Table A.2.

method is employed in this study.

A lock-in amplifier is described by Scofield [31] as a device to measure the amplitude of a signal who is completely synchronous to a reference input. In this work, the reference input is not taken directly from the output signal due to hardware restrictions, yet one of the microphone signals is chosen to be as a pseudo-reference. To obtain this pseudo-reference signal, the following steps are followed:

- i. The microphone signal with the largest amplitude is chosen as the reference signal.
- ii. The band-pass filter described earlier in the chapter is applied on the the reference signal to clear out the other components and becomes the filtered reference signal.
- iii. The filtered reference signal is normalized by its amplitude becoming the normalized reference signal.
- iv. The Hilbert transform of the normalized reference signal is calculated to obtain the analytical signal.

The analytical signal computed throughout the steps described is taken as the pseudo-reference signal, \tilde{p}_{ref} , for the modified lock-in method. Please note that the Hilbert transform transforms a real valued readings into complex ones and this is designated by the *tilde* accent ($\tilde{\cdot}$).

Once the pseudo-reference signal, whose amplitude is 1, is calculated, the translation of the time domain data to frequency domain is performed by a cross-correlation between the measured pressure signal vector p_m of microphone m , and the pseudo-reference signal \tilde{p}_{ref} . Thus, the pressure reading of the microphone m in the frequency domain (\hat{P}_m) is calculated by

$$A_m = \frac{2}{t_{q_f} - t_{q_i}} \sum_{q=q_i}^{q_f-1} \left[\frac{p_{m,q} \Re\{\tilde{p}_{ref,q}\} + p_{m,q+1} \Re\{\tilde{p}_{ref,q+1}\}}{2} (t_{q+1} - t_q) \right], \quad (\text{A.1a})$$

$$B_m = \frac{2}{t_{q_f} - t_{q_i}} \sum_{q=q_i}^{q_f-1} \left[\frac{p_{m,q} \Im\{\tilde{p}_{ref,q}\} + p_{m,q+1} \Im\{\tilde{p}_{ref,q+1}\}}{2} (t_{q+1} - t_q) \right], \quad (\text{A.1b})$$

$$\hat{P}_m = A_m - 1jB_m, \quad (\text{A.1c})$$

where t is the discrete time vector, p_m is the pressure readings vector of microphone m , q_i and q_f are the initial and final data points, respectively, which are taken into

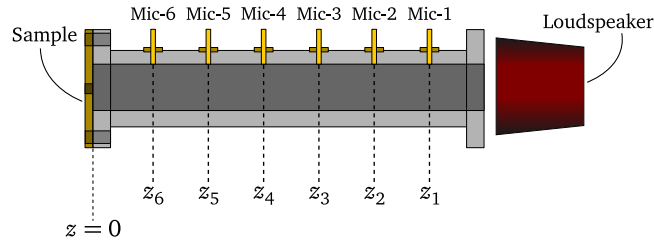


Figure A.6: Naming the microphones on the impedance tube and the reference plane for z -direction.

account in calculations. As it can be deduced from Eq. A.1, the trapezoidal rule is used for calculating the cross-correlation.

A.3 Calibration Procedure

Calibration of the set-up components is necessary to perform accurate acoustic measurements [80]. To achieve the maximum measurement accuracy, a series of several calibrations are performed on the impedance tube set-up described in Figure A.1. In this section, the procedure of these calibration procedures are described. To assist this description, the naming and the positioning of the microphones are illustrated in Figure A.6.

A.3.1 Absolute and Relative Calibration

In the impedance tube set-up described in, the analyser script is programmed in such a way that the output signal is adjusted to a pre-determined amplitude value which is controlled by the microphone closest to the tube termination, which is referred as *Mic-6*. Thus, absolute calibration is applied on *Mic-6*, then taking *Mic-6* as the reference, remaining microphones are calibrated relatively. For the absolute calibration, a Brüel&Kjær[®] piston-phone is used, and *Mic-6* is calibrated for 1 Pa at 1000 Hz. Then, *Mic-6* is placed in the calibration apparatus, which is schematically described in Figure A.7, with the rest of the microphones and relative calibration performed.

As in Figure A.7, all the microphones are located at the same distance from the closed termination. During the calibration measurements, the original microphone locations on the tube are sealed with specially built metal blocks, which are in the

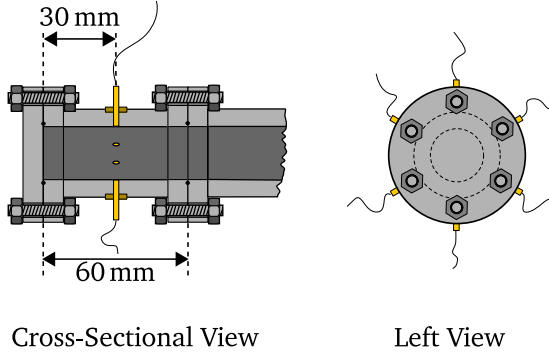


Figure A.7: The cross-sectional view of the calibration apparatus attached to the impedance tube, and the left view. All of the microphones are located around the tube, so that the distance from the termination is the same for each one.

same size as the microphone holders shown in Figure A.1b. The calibration measurements are also performed in the same manner as the actual measurements, *i.e.* single tone excitation during 10 seconds. Assuming plane wave propagation in the tube, every microphone located on the apparatus is expected to measure the same pressure amplitude and the phase.

When the entire frequency span is covered by the measurements, the data from each microphone is processed and the corresponding complex pressure value for each frequency is computed with the modified lock-in method described earlier. Then, taking Mic-6 data as the reference, calibration factors are computed for each microphone at each frequency step. For a certain frequency f , a calibration factor for microphone m (\widehat{CF}_m) is calculated as

$$\widehat{CF}_m(f) = \hat{P}_6^c(f) / \hat{P}_m^c(f), \quad (\text{A.2})$$

where the superscript c denotes the values measured with *calibration measurement* configuration as shown in Figure A.7.

After the microphones are carefully placed into their original positions, the actual measurements are ready to be performed. During the post processing of the actual measurement data, the calibrated complex pressure value of microphone m (\hat{P}_{m-c}) at each frequency step is calculated as

$$\hat{P}_{m-c}(f) = \hat{P}_m(f) \widehat{CF}_m(f). \quad (\text{A.3})$$

Table A.3: Microphone positions for the set-up described in this chapter.

	x_1 [mm]	x_2 [mm]	x_3 [mm]	x_4 [mm]	x_5 [mm]	x_6 [mm]
Position	-925	-750	-575	-400	-225	-50

A.4 Multi-Microphone Method and Reflection Coefficient Measurements

The complex pressure amplitude distribution at a certain frequency and in an acoustic medium represented by planar acoustic waves is given as [8]

$$\hat{p}(z) = \hat{p}^+ e^{-jk_c z} + \hat{p}^- e^{jk_c z}, \quad (\text{A.4})$$

where incident and reflected waves are represented by superscripts (+) and (−), respectively; and k_c is the complex wave number taking thermo-viscous effects into account along the tube wall and described by Peters *et al.* [29] as

$$k_c = \frac{\omega}{c_0} \left[1 + \frac{1-j}{\sqrt{2}Sh_D} \left(1 + \frac{\gamma-1}{Pr^{0.5}} \right) \right] - \frac{\omega}{c_0} \left[\frac{j}{Sh_D^2} \left(1 + \frac{\gamma-1}{Pr^{0.5}} - \frac{\gamma}{2} \frac{\gamma-1}{Pr} \right) \right], \quad (\text{A.5})$$

where γ is the ratio of the specific heats and Pr is the Prandtl number for air. Moreover, in Eq.(A.5), the thickness of the Stokes layer along the tube is given by $Sh_D = D\sqrt{\rho_0 2\pi f / (4\mu)}$, where $\rho_0 = 1.205 \text{ kg/m}^3$ is the density and $\mu = 1.82 \times 10^{-5} \text{ kg/ms}$ dynamic viscosity of air (at 20°C and 1 atm).

Since the microphones in the impedance tube set-up described in this chapter are fixed, the complex pressure amplitudes measured by each microphone is calculated as

$$\hat{P}_m = \hat{p}(z_m) = \hat{p}^+ e^{-jk_c z_m} + \hat{p}^- e^{jk_c z_m}; \quad m = 1, \dots, 6. \quad (\text{A.6})$$

The values for z_m are estimated from Figures A.2 and A.6 and given in Table A.3.

Microphones can only measure the complex pressure amplitude at a certain position. Thus, to decompose the pressure wave into incident and reflected waves, at least one more measurement is necessary. This way, one has two equations to solve for the two unknowns in Eq. (A.4). In other words, measurement two microphones are enough to decompose the complex pressure amplitude into incident (\hat{p}^+) and reflected wave (\hat{p}^-) wave components by providing a determined system of equations [73].

However, the set-up described in this chapter has six microphones. If one uses all the pressure readings from these six microphones to solve for \hat{p}^+ and \hat{p}^- in Eq. (A.4), the system of equations become over-determined as shown below.

$$\begin{bmatrix} e^{-jk_c z_1} & e^{jk_c z_1} \\ e^{-jk_c z_2} & e^{jk_c z_2} \\ e^{-jk_c z_3} & e^{jk_c z_3} \\ e^{-jk_c z_4} & e^{jk_c z_4} \\ e^{-jk_c z_5} & e^{jk_c z_5} \\ e^{-jk_c z_6} & e^{jk_c z_6} \end{bmatrix} \begin{Bmatrix} \hat{p}^+ \\ \hat{p}^- \end{Bmatrix} = \begin{Bmatrix} \hat{P}_1 \\ \hat{P}_2 \\ \hat{P}_3 \\ \hat{P}_4 \\ \hat{P}_5 \\ \hat{P}_6 \end{Bmatrix}, \quad (\text{A.7})$$

which can be simplified as $\mathbf{Ax} = \mathbf{y}$, where \mathbf{A} is the coefficients matrix, the 6×2 matrix on the left-hand side of Eq. A.7; \mathbf{x} is the unknowns vector composed of incident and reflected waves and \mathbf{y} is the vector of known quantities obtained by the measurements from six microphones. Since matrix \mathbf{A} is not a square matrix, the solution of the system given in Eq. (A.7) is not straightforward. Hence, the Moore-Penrose generalized inverse of matrix \mathbf{A} , which is \mathbf{A}^+ , is needed to be calculated as follows [81].

$$\mathbf{A}^+ = (\mathbf{A}^H \mathbf{A})^{-1} \mathbf{A}^H, \quad (\text{A.8})$$

where \mathbf{A}^H is the *Hermitian* of matrix \mathbf{A} .

The best approximate solution for the unknowns vector \mathbf{x} is estimated by [32]

$$\begin{Bmatrix} \hat{p}^+ \\ \hat{p}^- \end{Bmatrix} = \begin{bmatrix} e^{-jk_c z_1} & e^{jk_c z_1} \\ e^{-jk_c z_2} & e^{jk_c z_2} \\ e^{-jk_c z_3} & e^{jk_c z_3} \\ e^{-jk_c z_4} & e^{jk_c z_4} \\ e^{-jk_c z_5} & e^{jk_c z_5} \\ e^{-jk_c z_6} & e^{jk_c z_6} \end{bmatrix}^+ \begin{Bmatrix} \hat{P}_1 \\ \hat{P}_2 \\ \hat{P}_3 \\ \hat{P}_4 \\ \hat{P}_5 \\ \hat{P}_6 \end{Bmatrix}. \quad (\text{A.9})$$

Then, the reflection coefficient ζ at position $z = 0$, at a certain frequency is calculated by [32]

$$\zeta = \frac{\hat{p}^-}{\hat{p}^+}. \quad (\text{A.10})$$

A.5 Validation

Once the set-up is calibrated and the post-processing measures are taken, a well-known case is used for validation: the reflection coefficient of a rigid, closed-end

tube termination. For this measurement, a 20-mm thick aluminium disk is attached to the tube termination and reflection coefficient is measured between 80 Hz and 700 Hz.

In the limit case of no visco-thermal losses, the boundary condition at the rigid tube termination ($z = 0$) yields that

$$\hat{u} = \frac{\hat{p}^+ - \hat{p}^-}{\rho_0 c_0} = 0, \quad (\text{A.11})$$

so that the expected reflection coefficient is $\zeta = 1 + 0j$. As the reflection coefficient is represented in absolute value and phase, then it corresponds to

$$\zeta = |\zeta|e^{j\theta} = 1e^{j0}. \quad (\text{A.12})$$

The validation measurement results for $|\zeta|$ and θ are shown in Figure A.8.

As can be seen from the closed-end measurements in Figure A.8, the measured absorption coefficient amplitude has a deviation of less than 0.5% from the ideal case. It is also observable that there is a decreasing trend in the absolute value of ζ as the frequency increases. This is due to the thermal boundary layer at the rigid end [30].

In terms of phase, we also observe a discrepancy between 0.005 to 0.010 radians from the ideal case. Moreover, this deviation also appears to increase with frequency. However, this systematic deviation results from the difference between the measured and actual microphone positions. This frequency dependent deviation is fixed easily and described here.

A.5.1 Correcting the microphone positions

The impedance set-up measures the *reflection coefficient*, ζ , as described in Section A.4. In case of a rigid closed-end termination, the expected reflection coefficient is $\zeta_{rigid} = 1 + j0$. Thus, the phase of the reflection coefficient should be zero, also. The linear deviation from this value in Figure A.8b is due to the difference between the actual and measured positions of the microphones.

To find an average correction value to all the microphones, the definition of the reflection coefficient is used.

$$\zeta = |\zeta|e^{j\theta}, \quad (\text{A.13})$$

where $|\zeta|$ is the amplitude and θ is the phase angle of the reflection coefficient. In the closed-end measurements shown in Figure A.8, the linear shift in the phase of the reflection coefficient is observed. To quantify this shift, a least-squares linear

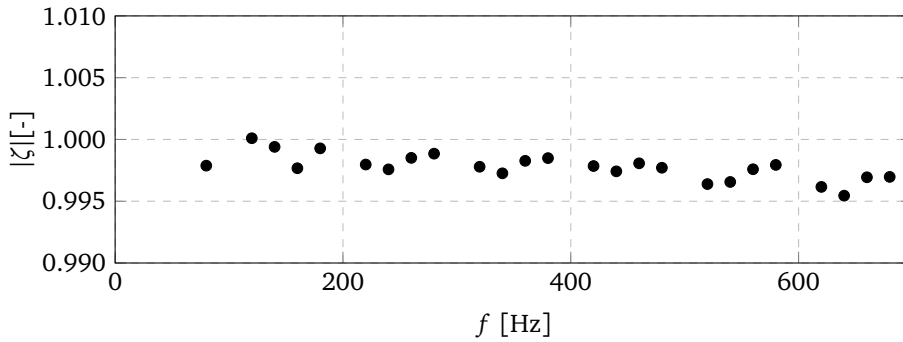
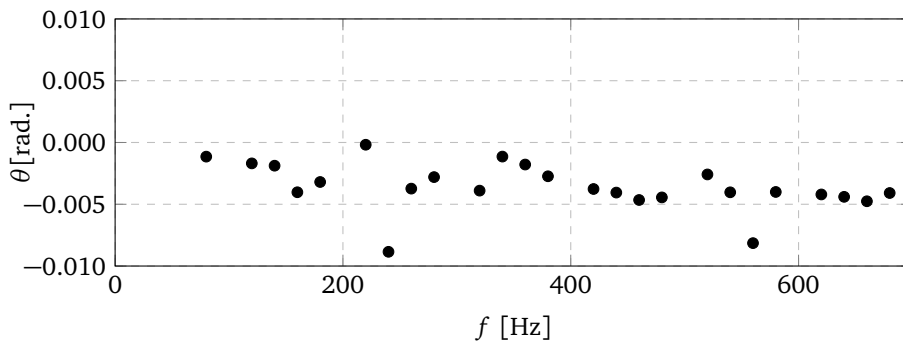
(a) Amplitude of the reflection coefficient, $|\zeta|$.(b) Phase of the reflection coefficient, θ .

Figure A.8: Validation of the impedance tube set-up with closed-end reflection coefficient measurements.

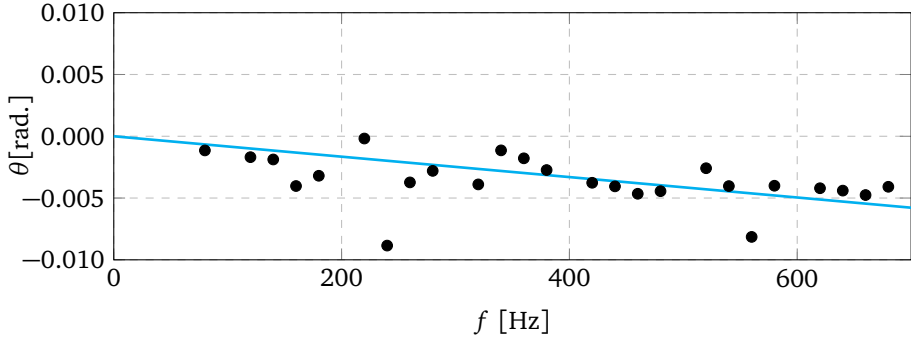


Figure A.9: The shift in the phase of the reflection coefficient of a closed-end termination: (●) the measurements, (—) the least-squares linear fit.

fit, which is forced to pass through $\theta = 0$ when $f = 0$ is calculated. The fit for the phase angle, θ_{fit} is calculated as

$$\theta_{fit} = -8.26 \times 10^{-6} f, \quad (\text{A.14})$$

as can be seen from Figure A.9. The quality of the fit is $r^2 = 0.80$, where $(1 - r^2)$ is the variance of the fit.

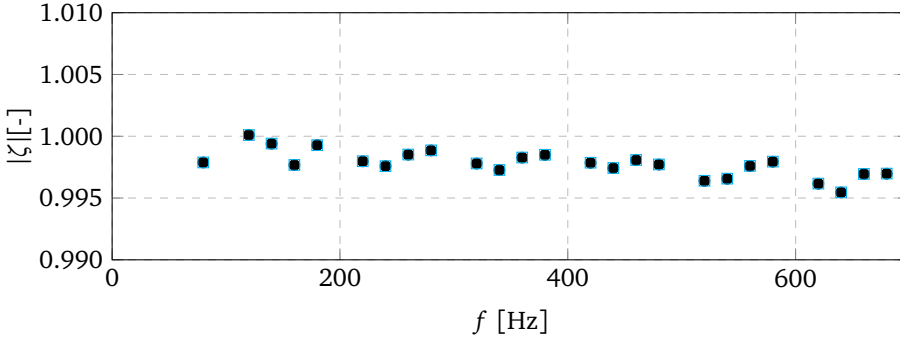
To find the shift between the actual microphone positions and the measured ones, using the definition of the reflection coefficient, the shift between the actual and measured position of each microphone, z_s is calculated by

$$\begin{aligned} e^{j\theta_{fit}} &= e^{2jk_0 z_s}, \\ \theta_{fit} &= 2 \frac{\omega}{c_0} z_s, \\ z_s &= \frac{\theta_{fit} c_0}{2\omega}. \end{aligned} \quad (\text{A.15})$$

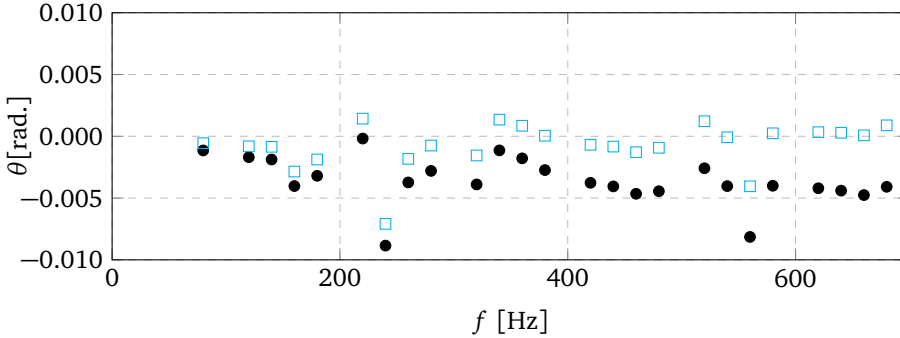
Furthermore, combining Eqs. (A.14) and (A.15), the amount of position shift is calculated as

$$z_s = \frac{-8.26 \times 10^{-6} f 343.3}{4\pi f} = -0.2 \text{ mm}. \quad (\text{A.16})$$

The shift calculated by Eq. A.16 is added to the current microphone positions to



(a) Absolute value of the reflection coefficient for closed-end tube termination.



(b) Phase of the reflection coefficient for the closed-end tube termination.

Figure A.10: The effect of correcting for the microphone positions in a closed end tube termination. (●) before correction; (□) after correction.

compensate for the difference.

$$z_{m-new} = z_{m-old} + z_s, \quad m = 1, 2, 3, \dots, 6. \quad (\text{A.17})$$

Since adding z_s to all microphones does not change the distance between them, the absolute value of the reflection coefficient does not change after this correction. It only affects the phase, as can be seen in Figure A.10.

As it can be observed from Figure A.10, the correction in the microphone positions eliminates the systematic deviation from the phase measurements. Consequently, the impedance tube set-up can perform measurements with an accuracy of

99.5% in terms of reflection coefficient.

A.6 Miscellaneous Precautions

Along with the systematic precautions that is described in the chapter so far, some further individual measures are taken to increase the overall accuracy of the measurements. First of all, as it can be seen from Figure A.1, the loudspeaker is separated from the tube and the gap between them is covered by pieces of acoustic foam. This is due to fact that, the loudspeaker excite the structural modes of the tube around 300 Hz and spurious peaks are observed near that particular frequency. After the separation of the loudspeaker and the tube, this spurious peak has disappeared.

The second precaution is taken to avoid the relative motion between the microphones and their cables in case there is a remaining structural vibration on the tube. To prevent this, each microphone cable is taped on the impedance tube next to the microphones.

Moreover, in the semi-anechoic chamber, there are two tables to support the separate loudspeaker and the measurement computer (analyser). To avoid undesired resonances that may occur from the cavities underneath these tables, wedges made of acoustic foam are used for occupying these volumes. Furthermore, the ground surface at the open termination of the impedance tube is covered with these sound absorbing wedges, so that the sound radiation from the open end is not affected by the waves reflecting from the surface. This configuration can be seen in Figure A.1a.

Another measure is to not calculate the speed of sound from the temperature and the humidity of the room, but to measure it using the excess data obtained in the multi-microphone measurements.

Owing to the fact that the current frequency of the electric network is 50 Hz, this frequency and its multiples are also ignored in measurements and post-processing.

Last but not least, when two metal surfaces have to contact with each other in a measurement configuration, an o-ring is used for preventing the air-leak and causing undesired resonance.

Appendix B

Mesh Convergence

A mesh convergence study is performed for the discrete numerical model. Since the most critical part of the numerical domain is around the perforations, the element size representing the perforations is the main focus of this study. The size of the elements in and around one of the perforations is compared in Figure B.1: Mesh-1 is the typical mesh built for the simulations in this study and Mesh-2 is the finer mesh built for checking the effect of element size.

The parameters of the numerical model used for comparing the effect of mesh is chosen among the test cases, *i.e.* VA1 (see Table 5.4). The reason for selecting

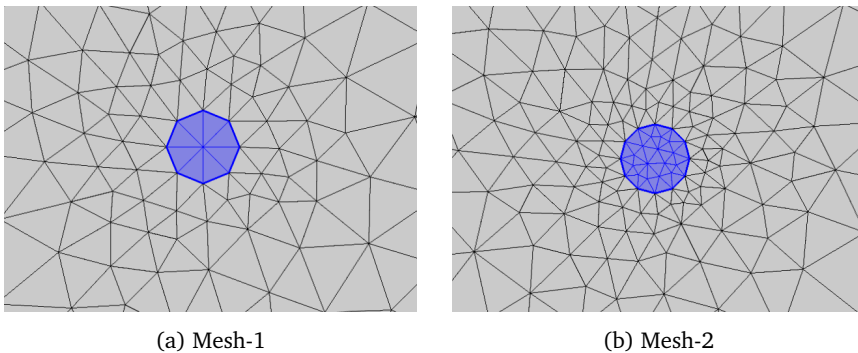


Figure B.1: The element size comparison for two meshes built to represent the same geometry. The diameter of the perforation here is 0.5 mm.

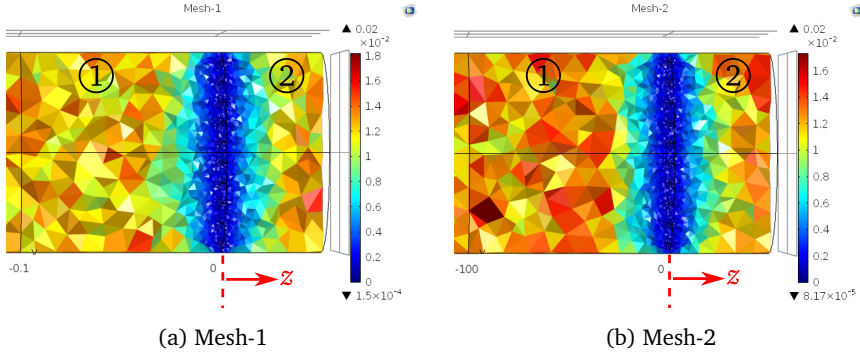


Figure B.2: A slice of the numerical domain in yz -plane to show the gradual increase of the element size from the plate to the rest of the acoustic domain. Different colours represent the element size and the dimensions provided in the scale are in [m].

this particular case is that it has the smallest perforation diameter, thus the number of elements in perforations is more critical than other cases in this study.

To minimize the number of elements in the mesh, a gradually increasing element size is used. The maximum growth rate of the elements are selected as 1.35 in this study. As a result, once the size of the elements around the perforations become smaller, they affect the size of the elements around. The gradual change in the element size away from the plate is given for Mesh-1 and Mesh-2 in Figure B.2.

In Figures B.1 and B.2, it is seen that Mesh-2 has 5 times more elements in a perforation compared to Mesh-1. Moreover, the size of the elements are decreased both for the plate and the acoustic volume around the perforation. In general, the number of elements in Mesh-2 is 30% more than those of Mesh-1. To assess this effect on the absorption coefficient, the relative percentage error, $\epsilon_{\%}$, is calculated as follows:

$$\epsilon_{\%} = \frac{|\beta_2 - \beta_1|}{\beta_2} 100\%, \quad (\text{B.1})$$

where β_1 and β_2 are the absorption coefficients calculated in the simulations using Mesh-1 and Mesh-2, respectively. The graph over the frequency range of interest, $100 \text{ Hz} \leq f \leq 2000 \text{ Hz}$ is illustrated in Figure B.3.

In Figure B.3, it is seen that, increasing the number of elements in the perforations by factor 5 does not affect the absorption coefficient more than 1% for

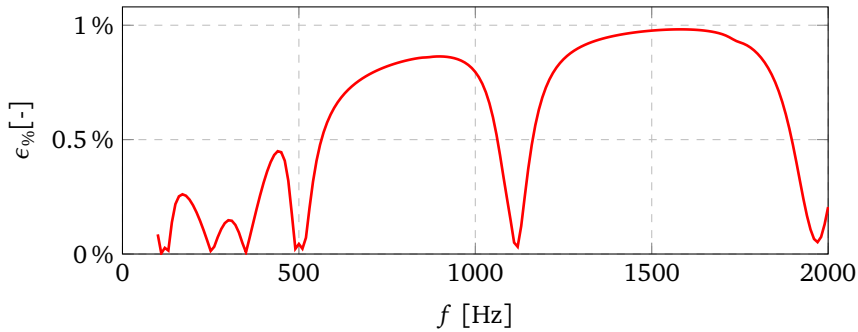


Figure B.3: The relative percentage error between Mesh-1 and Mesh-2. Increasing the number of elements in the perforation by 5 times in each perforation results in a difference of less than 1% relative error in the absorption coefficient. Please note that when the absorption coefficient is not close to zero, the relative error is even less.

$100\text{ Hz} \leq f \leq 2000\text{ Hz}$. Considering the absorption coefficient vs. frequency graph of Case VA1 (see Figure 5.12), the increase in ϵ_0 is due to the division of two small numbers. For absorption peaks, the relative percentage error is significantly lower than 1%.

Bibliography

- [1] J. Hansen, R. Ruedy, M. Sato, and K. Lo, “Global surface temperature change,” Reviews of Geophysics, vol. 48, pp. RG4004 / 1–29, 2010.
- [2] GISTEMP Team, “GISS Surface Temperature Analysis (GISTEMP). NASA Goddard Institute for Space Studies.” <https://data.giss.nasa.gov/gistemp/>, 2017. [Online; accessed 08-February-2017].
- [3] Y. Huang and V. Yang, “Dynamics and stability of lean-premixed swirl-stabilized combustion,” Progress in Energy and Combustion Science, vol. 35, no. 4, pp. 293–364, 2009.
- [4] T. Lieuwen, “Modeling premixed combustion - acoustic wave interactions: A review,” Journal of Propulsion and Power, vol. 19, no. 5, pp. 765–781, 2003.
- [5] TANGO Network, “Thermoacoustic and Aeroacoustic Nonlinearities in Green combustors with Orifice structures.” <http://www.scm.keele.ac.uk/Tango/>, 2014. [Online; accessed 06-February-2017].
- [6] D.-Y. Maa, “Potential of microperforated panel absorber,” J. Acoust. Soc. Am., vol. 104, no. 5, pp. 2861–2866, 1998.
- [7] D. Tonon, E. M. T. Moers, and A. Hirschberg, “Quasi-steady acoustic response of wall perforations subject to a grazing-bias flow combination,” Journal of Sound and Vibration, vol. 332, no. 7, pp. 1654–1673, 2013.
- [8] L. E. Kinsler, A. R. Frey, A. B. Coppens, and J. V. Sanders, Fundamentals of Acoustics. New York: John Wiley and Sons, 4 ed., 2000.
- [9] T. Bravo, C. Maury, and D. Pinhède, “Sound absorption and transmission through flexible micro-perforated panels backed by an air layer and a thin

- plate,” The Journal of Acoustic Society of America, vol. 131, no. 5, pp. 3853–3863, 2012.
- [10] A. P. Dowling and Y. Mahmoudi, “Combustion noise,” Proceedings of the Combustion Institute, vol. 35, no. 1, pp. 65–100, 2015.
- [11] S. H. Park, “A Design Method of Micro-perforated Panel Absorber at High Sound Pressure Environment in Launcher Fairings,” Journal of Sound and Vibration, vol. 332, no. 3, pp. 521–535, 2013.
- [12] R. Kabral, L. Du, M. Åbom, and M. Knutsson, “A compact silencer for the control of compressor noise,” SAE International Journal of Engines, vol. 7, no. 3, pp. 1572–1578, 2014.
- [13] T. Bravo, C. Maury, and D. Pinhède, “Optimisation of micro-perforated cylindrical silencers in linear and nonlinear regimes,” Journal of Sound and Vibration, vol. 363, pp. 359–379, 2016.
- [14] G. Kirchhoff, “Über den Einfluss der Wärmeleitung in einem Gase auf die Schallbewegung,” Annalen der Physik und Chemie, vol. 210, no. 6, pp. 177–193, 1868.
- [15] U. Ingard, “On the Theory and Design of Acoustic Resonators,” The Journal of the Acoustical Society of America, vol. 25, no. 6, pp. 1037–1061, 1953.
- [16] M. C. A. M. Peters and A. Hirschberg, “Acoustically Induced Periodic Vortex Shedding at Sharp Edged Open Channel Ends: Simple Vortex Models,” The Journal of Sound and Vibration, vol. 161, no. 2, pp. 281–299, 1993.
- [17] U. Ingard and S. Labate, “Acoustic Circulation Effects and the Nonlinear Impedance of Orifices,” The Journal of the Acoustical Society of America, vol. 22, no. 2, pp. 211–218, 1950.
- [18] U. Ingard and H. Ising, “Acoustic Nonlinearity of an Orifice,” The Journal of the Acoustical Society of America, vol. 42, no. 1, pp. 6–17, 1967.
- [19] S. Allam and M. Åbom, “A New Type of Muffler Based on Microperforated Tubes,” The Journal of Vibration and Acoustics, vol. 133, no. 3, pp. 503–581, 2011.

- [20] T. Dupont, G. Pavic, and B. Lauglagnet, "Acoustic Properties of Lightweight Micro-Perforated Plate Systems," Acta Acustica United with Acustica, vol. 89, no. 2, pp. 201–212, 2003.
- [21] Y. Guo, S. Allam, and M. Åbom, "Micro-perforated plates for vehicle application," in The 37th International Congress and Exposition on Noise Control Engineering, (Beijing, China), pp. 773–792, 2009.
- [22] J. Lee and G. W. Swenson, "Compact sound absorbers for low frequencies," Noise Control Engineering Journal, vol. 38, no. 3, pp. 109–117, 1992.
- [23] COMSOL Inc., "COMSOL Multiphysics." <https://www.comsol.com>, 2015. [Online; accessed 19-October-2016].
- [24] M. A. Temiz, I. Lopez Arteaga, G. Efraimsson, M. Åbom, and A. Hirschberg, "The influence of edge geometry on end-correction coefficients in micro-perforated plates," The Journal of the Acoustical Society of America, vol. 138, no. 6, pp. 3668–3677, 2015.
- [25] I. B. Crandall, Theory of Vibrating Systems and Sound. New York: van Nostrand Company, 1926.
- [26] J. S. Bolton and N. Kim, "Use of CFD to Calculate the Dynamic Resistive End Correction for Microperforated Materials," Acoustics Australia, vol. 38, no. 3, pp. 134–139, 2010.
- [27] T. Herdtle, J. S. Bolton, N. N. Kim, J. H. Alexander, and R. W. Gerdes, "Transfer Impedance of Microperforated Materials with Tapered Holes," The Journal of the Acoustical Society of America, vol. 134, no. 6, pp. 4752–4762, 2013.
- [28] J. Carbajo, J. Ramis, L. Godinho, P. Amado-Mendes, and J. Alba, "A Finite Element Model of Perforated Panel Absorbers Including Viscothermal Effects," Applied Acoustics, vol. 90, pp. 1–8, 2015.
- [29] M. C. A. M. Peters, A. Hirschberg, A. J. Reijnen, and A. P. J. Wijnands, "Damping and reflection coefficient measurements for an open pipe at low Mach and low Helmholtz numbers," Journal of Fluid Mechanics, vol. 256, pp. 499–534, 1993.
- [30] L. Peerlings, Methods and Techniques for precise and accurate in-duct aero-acoustic measurements: Application to the Area Expansion. PhD thesis, KTH Royal Institute of Technology, Stockholm, 2015. Licentiate Thesis.

- [31] J. H. Scofield, "Frequency-domain description of a lock-in amplifier," American Journal of Physics, vol. 62, no. 2, pp. 129–133, 1994.
- [32] S. H. Jang and J. G. Ih, "On the multiple microphone method for measuring in-duct acoustic properties in the presence of mean flow," The Journal of the Acoustical Society of America, vol. 103, no. 3, pp. 1520–1526, 1998.
- [33] Y. Aurégan and M. Leroux, "Failures in the Discrete Models for Flow Duct with Perforations: An experimental Investigation," Journal of Sound and Vibrations, vol. 265, pp. 109–121, 2003.
- [34] M. A. Temiz, I. Lopez Arteaga, G. Efraimsson, M. Åbom, and A. Hirschberg, "Acoustic end correction in micro-perforated plates - revisited," in 21st International Congress on Sound and Vibration 2014, ICSV 2014, vol. 2, (Beijing), pp. 1203–1209, 2014.
- [35] P. Morse and K. Ingard, Theoretical Acoustics. New Jersey: McGraw-Hill, 1968.
- [36] A. D. Pierce, Acoustics: An Introduction to Its Physical Principles and Applications. London: McGraw-Hill, 2 ed., 1989.
- [37] M. A. Temiz, J. Tournadre, I. Lopez Arteaga, and A. Hirschberg, "Non-linear acoustic transfer impedance of micro-perforated plates with circular orifices," Journal of Sound and Vibration, vol. 366, pp. 418–428, 2016.
- [38] D. Y. Maa, "Microperforated panel at high sound intensity," in Proceedings of Internoise 1994, vol. 94, (Yokohama), pp. 1511–1514, 1994.
- [39] L. J. Sivian, "Acoustic impedance of small orifices," Journal of Acoustical Society of America, vol. 7, pp. 94–101, 1938.
- [40] A. W. Guess, "Calculation of Perforated Plate Liner Parameters from Specified Acoustic Resistance and Reactance," Journal of Sound and Vibration, vol. 40, no. 1, pp. 119–137, 1974.
- [41] J. H. M. Disselhorst and L. van Wijngaarden, "The dissipation of sound at an edge," Journal of Fluid Mechanics, vol. 99, no. 2, pp. 293–319, 1980.
- [42] A. Cummings and W. Eversman, "High amplitude acoustic transmission through duct terminations: Theory," The Journal of Sound and Vibration, vol. 91, no. 4, pp. 503–581, 1983.

- [43] P. Testud, P. Moussou, A. Hirschberg, and Y. Aurégan, “Noise Generated by Cavitating Single-Hole and Multi-Hole Orifices in a Water Pipe,” Journal of Fluids and Structures, vol. 23, no. 2, pp. 163–189, 2007.
- [44] Y. Aurégan and M. Pachebat, “Measurement of the Non-linear Behaviour of the Acoustical Rigid Porous Materials,” Physics of Fluids, vol. 11, no. 6, pp. 1342–1345, 1999.
- [45] G. C. J. Hofmans, R. J. J. Boot, P. P. J. M. Durrieu, Y. Aurégan, and A. Hirschberg, “Aeroacoustic Response of a Slit-shaped Diaphragm in a Pipe at a Helmholtz Number, 1: Quasi-Steady Results,” Journal of Sound and Vibration, vol. 244, no. 1, pp. 35–56, 2001.
- [46] X. Jing and X. Sun, “Sound-excited Flow and Acoustic Non-linearity at an Orifice,” Physics of Fluids, vol. 14, no. 1, pp. 268–276, 2002.
- [47] R. C. K. Leung, R. M. C. So, M. H. Wang, and X. M. Li, “In-duct Orifice and Its Effect on Sound Absorption,” Journal of Sound and Vibration, vol. 299, pp. 990–1004, 2007.
- [48] J. M. Buick, M. Atig, D. J. Skulina, D. M. Campbell, J. P. Dalmont, and J. Gilbert, “Investigation of Non-linear Acoustic Losses at the Open End of a Tube,” The Journal of Acoustical Society of America, vol. 129, no. 3, pp. 1261–1272, 2011.
- [49] C. Ji and D. Zhao, “Lattice Boltzmann Investigation of Acoustic Damping Mechanism And Performance of an In-duct Circular Orifice,” The Journal of the Acoustical Society of America, vol. 135, no. 6, pp. 3243–3251, 2014.
- [50] J. Lighthill, Waves in Fluids. Cambridge: Cambridge University Press, 2 ed., 1978.
- [51] D. Gilbarg, Encyclopedia of Physics, vol. 3 of 9, ch. Jets and Cavities, pp. 311–445. Berlin: Springer-Verlag, 1960.
- [52] M. Firdaouss, J. L. Guermond, and P. Le Quéré, “Nonlinear Corrections to Darcy’s Law at Low Reynolds Numbers,” The Journal of Fluid Mechanics, vol. 343, pp. 331–350, 1997.
- [53] S. Rojas and J. Koplik, “Nonlinear Flow in Porous Media,” Physical Review E, vol. 58, no. 4, pp. 4776–4782, 1998.

- [54] D. H. Keefe, “Acoustic streaming, dimensional analysis of nonlinearities, and tone hole mutual interactions in woodwinds,” The Journal of the Acoustical Society of America, vol. 73, no. 5, pp. 201–212, 1982.
- [55] D. A. Bies and O. B. Wilson, “Acoustic Impedance of Helmholtz Resonator at Very High Amplitude,” The Journal of the Acoustical Society of America, vol. 29, no. 6, pp. 201–212, 1957.
- [56] T. H. Melling, “The acoustic impedance of perforates at medium and high sound pressure levels,” Journal of Sound and Vibration, vol. 29, no. 1, pp. 1–65, 1973.
- [57] A. Cummings, “Transient and multiple frequency sound transmission through perforated plates at high amplitude,” The Journal of the Acoustical Society of America, vol. 79, no. 4, pp. 942–951, 1986.
- [58] A. Hirschberg, J. Gilbert, A. P. J. Wijnands, and A. M. C. Valkering, “Musical aero-acoustics of the clarinet,” Journal de Physique IV, vol. 4, no. 5, pp. 559–567, 1994.
- [59] D. A. Bies and O. B. Wilson, “Nonlinear Acoustic Properties of Orifices of Varied Shapes and Edge Conditions,” The Journal of the Acoustical Society of America, vol. 29, no. 6, pp. 2–5, 1958.
- [60] R. McDonald, A Study of the Undercutting of Woodwind Tone-holes Using Particle Image Velocimetry. PhD thesis, University of Edinburgh, Edinburgh, 2009.
- [61] K. Foerner, M. A. Temiz, W. Polifke, I. Lopez Arteaga, and A. Hirschberg, “On the non-linear influence of the edge geometry on vortex shedding in helmholtz resonators,” in 22nd International Congress on Sound and Vibration, ICSV 2015, (Florence), 2015.
- [62] K. Förner, J. Tournadre, P. Martínez-Lera, and W. Polifke, “Scattering to higher harmonics for quarter-wave and helmholtz resonators,” AIAA Journal, Articles in Advance, vol. 0, no. 0, pp. 1–11, 2016.

- [63] J. P. Oosterhuis, S. Bühler, T. H. van der Meer, and D. Wilcox, "A numerical investigation on the vortex formation and flow separation of the oscillatory flow in jet pumps," The Journal of the Acoustical Society of America, vol. 137, no. 4, pp. 1722–1731, 2015.
- [64] H. Levine and J. Schwinger, "On the radiation of sound from an unflanged circular pipe," Physical Review, vol. 73, no. 4, pp. 383–406, 1947.
- [65] L. Cremer and H. A. Müller, Principles and Applications of Room Acoustics, vol. 2. London: Applied Science Publishers, 1978. Translated by T. J. Schultz in 1982.
- [66] T. G. H. Basten, P. J. M. van der Hoogt, R. M. E. J. Spiering, and H. Tijdeman, "On the Acousto-Elastic Behaviour of Double-Wall Panels with a Viscothermal Air Layer," Journal of Sound and Vibration, vol. 243, no. 4, pp. 699–719, 2001.
- [67] Y. Y. Lee, E. W. M. Lee, and C. F. Ng, "Sound absorption of a finite flexible micro-perforated panel backed by an air cavity," Journal of Sound and Vibration, vol. 287, pp. 227–243, 2005.
- [68] M. Toyoda, R. L. Mu, and D. Takahashi, "Relationship between Helmholtz-resonance absorption and panel-type absorption in finite flexible microperforated-panel absorbers," Applied Acoustics, vol. 71, no. 4, pp. 315–320, 2010.
- [69] T. Bravo, C. Maury, and D. Pinhède, "Enhancing sound absorption and transmission through flexible multi-layer micro-perforated structures," The Journal of Acoustic Society of America, vol. 134, no. 5, pp. 3663–3673, 2013.
- [70] C. Li, B. Cazzolato, and A. Zander, "Acoustic impedance of micro perforated membranes: Velocity continuity condition at the perforation boundary," The Journal of Acoustic Society of America, vol. 139, no. 1, pp. 93–103, 2016.
- [71] G. Kirchhoff, "Über das Gleichgewicht und die Bewegung einer elastischen Scheibe," Journal für die reine und angewandte Mathematik, vol. 40, pp. 51–88, 1850.
- [72] M. A. Temiz, J. Tournadre, I. Lopez Arteaga, P. Martinez-Lera, and A. Hirschberg, "Numerical estimation of the absorption coefficient of flexible micro-perforated plates in an impedance tube," in ICSV 2016 - 23rd

- International Congress on Sound and Vibration: From Ancient to Modern Acoustics, (Athens), 2016.
- [73] H. Bodén and M. Åbom, “Influence of errors on the two-microphone method for measuring acoustic properties in ducts,” The Journal of the Acoustical Society of America, vol. 79, no. 2, pp. 541–549, 1986.
- [74] Siemens PLM Software, “LMS Virtual.Lab 13.1.” https://www.plm.automation.siemens.com/en_us/products/lms/virtual-lab/, 2014. [Online; accessed 19-October-2016].
- [75] R. Tayong, T. Dupont, and P. Leclaire, “On the Variations of Acoustic Absorption Peak with Particle Velocity in Micro-Perforated Panels at High Level of Excitation,” The Journal of Acoustical Society of America, vol. 127, no. 5, pp. 545–557, 2010.
- [76] P. Kelly, “Solid Mechanics Part II: Engineering Solid Mechanics.” http://homepages.engineering.auckland.ac.nz/~pkel015/SolidMechanicsBooks/Part_II/index.html. Accessed: 2016-08-21.
- [77] L. Cremer, The Physics of the Violin. Massachusetts: The MIT Press, 1981. Translated by J. S. Allen in 1984.
- [78] D. Zhao and X. Y. Li, “A review of acoustic dampers applied to combustion chambers in aerospace industry,” Progress in Aerospace Sciences, vol. 74, pp. 114–130, 2015.
- [79] Mathworks, MATLAB Documentation, February 2016.
- [80] L. L. Beranek, Acoustic Measurements. New York: John Wiley & Sons, 4 ed., 1959.
- [81] R. Penrose and J. Todd, “A generalized inverse for matrices,” Mathematical Proceedings of the Cambridge Philosophical Society, vol. 51, no. 3, pp. 406–413, 1955.

Summary

Passive Noise Control by Means of Micro-Perforated Plates: Developing Tools for an Optimal Design

Micro-perforated plates (MPPs) are promising sound absorbers both for industrial and architectural applications because a large variety of materials, from metals to textile products, can be used to manufacture them. These plates have perforations with diameter of the order of a millimeter, corresponding to the Stokes layer thickness at audio frequencies. Hence the acoustic flow through the perforations is dominated by viscous forces. The ratio of the open area to the entire plate is about 1%. MPPs are supported with a back cavity, which acts as volume element in a Helmholtz resonator. Nevertheless, unlike Helmholtz resonators, MPPs perform broadband sound absorption due to viscous dissipation in the perforations.

MPPs can be used as sound absorbers with reduced hazard due to fire. They furthermore can be used in aggressive environments such as combustion chambers and jet engines. In that case they provide passive sound absorption and avoid potential thermo-acoustical instabilities. The present study focuses on the acoustic characteristics of MPPs and perforated plates, which should allow optimal design. The content of this thesis is based on four closely linked studies, which employ numerical and / or experimental methods.

The first study focuses on the influence of the geometry and size of the perforations on the acoustic response at low amplitudes, such that a linear theory can be used. The numerical model used for this study solves linearized Navier-Stokes equations in frequency domain and simulations are performed for perforations with various edge geometries. The verification experiments are open-end impedance tube measurements, which are performed in the semi-anechoic chamber to minimize the external effects. This study shows that for a given geometry the acoustic response depends mainly on the ratio of viscous boundary layer (Stokes layer) and perforation diameter. Empirical correlation formulas are provided.

The second study focuses on the non-linear effects on acoustic response of an MPP with sharp, square edges. Transfer impedance of MPP samples with different perforation diameter and thickness are measured by means of an impedance tube. To capture the non-linear acoustic effects, the excitation amplitude is increased up to acoustic particle displacements larger than the plate thickness. At such high amplitudes, the commonly used quasi-steady approximation can be used. The results of the present work provides a bridge between the linear to non-linear transition regime which has not received much attention until now.

The effect of edge-geometry on the acoustic non-linearity of a perforation is investigated in the third study. Samples with same thickness and perforation diameter but different edge profiles are used in the experiments. These experiments are performed as open-end transfer impedance measurements. It is observed that the edge profiles have a significant effect on the non-linear response. Moreover, a quasi-steady model is employed for estimating the acoustic energy dissipation in the fundamental harmonic and sound generation in higher harmonics. It is observed that, the quasi-steady theory fails to predict the acoustic response of a perforation in the transition regime.

Finally, vibro-acoustic coupling of MPPs are studied. As thin materials with large surfaces are commonly used, vibration does often influences the performance of the micro-perforated plates. A numerically efficient finite element model is used for examining the effect of perforation positions relative to vibrational modes of a micro-perforated plate. This numerical model solves Helmholtz equation for the acoustic domain and the plate is assumed to behave as a shell element. The perforations are described as discrete transfer impedance islands which are represented as internal impedance boundaries connecting the acoustic domains. With the help of this model, the distribution of perforations over the MPP can be optimized.

Our results should allow new and accurate designs of MPPs with non-conventional perforation edge geometries and with non-uniform spatial perforation distribution.

Samenvatting

Micro-geperforeerde platen (MPP's) zijn veelbelovende geluidsdempers voor zowel industriële als architectonische toepassingen aangezien ze gemaakt kunnen worden van een grote verscheidenheid aan materialen, variërend van metalen tot textielproducten. MMP's hebben perforaties met diameter in de orde van één millimeter, die correspondeert met de dikte van de Stokes grenslaag bij hoorbare geluidsfrequenties. Daarom wordt de akoestische stroming door de perforaties gedomineerd door viskeuze krachten. De verhouding tussen het open gebied en de oppervlakte van de gehele plaat is ongeveer 1%. MPP's worden gebouwd met een achterholte, die zich gedraagt als een Helmholtz resonator, maar in tegenstelling tot Helmholtz resonatoren absorberen MPP's geluid in een grote bandbreedte door de viskeuze dissipatie in de perforaties.

MPP's kunnen worden gebruikt als geluidsdempers met verminderd brandgevaar. Ze kunnen ook worden gebruikt in agressieve omgevingen zoals verbrandingskamers van vliegtuigmotoren. Dat resulteert in passieve geluidsabsorptie en vermijdt potentiële thermo-akoestische instabiliteiten. De huidige studie concentreert zich op de akoestische eigenschappen van MPP's en geperforeerde platen, die gebruikt kunnen worden om het ontwerp van MMP's te optimaliseren. De inhoud van dit proefschrift bestaat uit vier studies die nauw met elkaar verbonden zijn. Deze studies maken gebruik van numerieke en/of experimentele methoden.

De eerste studie richt zich op de invloed van de geometrie en de grootte van de perforaties op de akoestische respons bij lage amplitudes, zodat een lineaire theorie kan worden gebruikt. Het numerieke model dat wordt gebruikt voor deze studie lost de gelineariseerde Navier-Stokes vergelijkingen op in het frequentiedomein. Simulaties worden uitgevoerd voor perforaties met diverse randgeometrieën. De verificatie experimenten zijn gedaan met een open-end impedantiebus in een semi-anechoïsche kamer om externe effecten te minimaliseren. Dit onderzoek toont aan dat de akoestische respons vooral af hangt van de verhouding tussen de dikte van de

Stokes grenslag en de perforatie diameter voor een gegeven geometrie. Empirische formules zijn ontwikkeld.

Het tweede onderzoek richt zich op de invloed van niet-lineaire effecten op de akoestische respons van MPP's met scherpe, haakse perforatieranden. De transferimpedantie van MPP's met diverse perforatiediameters en diktes wordt gemeten door middel van een impedantiebus. Om de niet-lineaire akoestische effecten te meten, is de excitatie-amplitude verhoogd tot niveaus waarbij de akoestische deeltjes verplaatsingen groter dan de plaatdikte hebben. Bij dergelijke hoge amplitudes kan de veelgebruikte quasi-stationaire benadering worden toegepast. De resultaten van het huidige werk vormen een brug tussen het lineaire en niet-lineaire transitierégime dat niet eerder in detail werd bestudeerd.

Het effect van perforatieranden op de akoestische niet-lineariteit van een perforatie wordt onderzocht in de derde studie. Monsters met dezelfde dikte en perforatie diameter maar met verschillende perforatieranden worden gebruikt in de experimenten. Deze experimenten worden uitgevoerd als open-end transferimpedantie metingen. Opgemerkt wordt dat de randprofielen een significant effect hebben op de niet-lineaire respons. Bovendien wordt een quasi-stationaire model toegepast voor het schatten van de akoestische energie dissipatie in de grondharmonische en geluidsgeneratie in hogere harmonischen. De quasi-stationaire theorie is niet in staat de akoestische respons van een perforatie in het transitierégime voorspellen.

In de vierde studie wordt de vibro-akoestische koppeling van twee akoestische domeinen door middel van een MPP bestudeerd. Aangezien MMP's gewoonlijk dunne platen met een groot oppervlak zijn, beïnvloeden trillingen vaak het gedrag van MMP's. Een numeriek efficiënt eindige elementen model wordt gebruikt om het effect van perforatie posities ten opzichte van trillingsmodes van de MMP te onderzoeken. Dit numeriek model lost de Helmholtz vergelijking op voor het akoestische domein. Verder wordt verondersteld dat de dikte van de plaat klein is. De perforaties worden beschreven als discrete transferimpedantie gebieden, die de koppeling tussen de twee akoestische domeinen beschrijven. Met behulp van dit model kan de verdeling van perforaties over de MPP worden geoptimaliseerd.

Deze resultaten moeten nieuwe en nauwkeuriger ontwerpen van MPP's mogelijk maken met niet-conventionele perforatieranden en met niet-uniforme ruimtelijke perforatie distributies.

List of Publications

Peer Reviewed Journal Articles

- M.A. Temiz, J. Tournadre, I. Lopez Arteaga and A. Hirschberg, Modelling vibro-acoustic coupling in flexible micro-perforated plates by a patch-impedance approach, *Submitted to Applied Acoustics in November 2016*.
- M.A. Temiz, J. Tournadre, I. Lopez Arteaga and A. Hirschberg, Non-linear acoustic transfer impedance of micro-perforated plates with circular orifices, *Journal of Sound and Vibration*, **366**, 418–428, 2016.
- M.A. Temiz, I. Lopez Arteaga, G. Efraimsson, M. Åbom and A. Hirschberg, The influence of edge geometry on end-correction coefficients in micro-perforated plates, *The Journal of the Acoustical Society of America*, **138** (6), 3668–3677, 2015.

Conference Papers

- M.A. Temiz, J. Tournadre, I. Lopez Arteaga, P. Martínez-Lera and A. Hirschberg, Numerical estimation of the absorption coefficient of flexible micro-perforated plates in an impedance tube. *23rd International Congress on Sound & Vibration (ICSV 23)*, 10-14 July 2016, Athens, Greece.
- M.A. Temiz, I. Lopez Arteaga and A. Hirschberg, Non-linear behaviour of tone holes in musical instruments: an experimental study. *Le 13e Congrès Français d'Acoustique (CFA 2016)*, 377–382, 11-15 April 2016, Université du Maine, le Mans, France.

- M.A. Temiz, J. Tournadre, I. Lopez Arteaga, P. Martínez-Lera and A. Hirschberg, Non-linear acoustic resistance of perforated plates in the transition regime. *22nd International Congress on Sound & Vibration (ICSV 22)*, 12-16 July 2015, Florence, Italy.
- K. Förner, M.A. Temiz, W. Polifke, I. Lopez Arteaga and A. Hirschberg, On the non-linear influence of the edge geometry on vortex shedding in Helmholtz resonators. *22nd International Congress on Sound & Vibration (ICSV 22)*, 12-16 July 2015, Florence, Italy.
- M.A. Temiz, I. Lopez Arteaga and A. Hirschberg, Sound absorption measurements for micro-perforated plates: the effect of edge profile. *EuroNoise 2015*, 31 May-3 June 2015, Maastricht, the Netherlands.
- M.A. Temiz, I. Lopez Arteaga, G. Efraimsson, M. Åbom and A. Hirschberg, Acoustic end-correction in micro-perforated plates: Revisited. *21st International Congress on Sound & Vibration (ICSV 21)*, 13-17 July 2014, Beijing, China.

Curriculum Vitae

Muttalip Aşkın Temiz was born on 25th March 1987 in Erbaa, Turkey. He studied Mechanical Engineering in Middle East Technical University from 2004 to 2009 in Ankara, Turkey. He obtained his MSc degree in Istanbul Technical University on ‘Machine Dynamics, Vibration and Acoustics’ in 2012, in Istanbul, Turkey. The main focus of his MSc thesis was in noise reduction with reactive mufflers.

Since February 2013, Muttalip has been working on the research topic ‘Passive Control by Micro-Perforated Plates’ as a PhD student in the Dynamics and Control Technologies group of Prof. Henk Nijmeijer in Eindhoven University of Technology, the Netherlands. During this study, Prof. Ines Lopez Arteaga and Prof. Avraham Hirschberg have been his daily supervisors. This research topic is a part of a Marie Curie Initial Training Network: TANGO Project (Thermoacoustic and Aeroacoustic Non-linearities in Green combustors with Orifice structures), which was funded by European Commission. The present thesis provide the findings of his study in TU/e.

Acknowledgements

I have a long list of people to thank...

First of all I would like to thank my advisors, Ines Lopez Arteaga and Mico Hirschberg. Without your invaluable guidance and help, this thesis would never be completed. I don't think I can find the right words to describe my gratitude for you even if I try it in my native language! Thank you... I am extremely lucky to have the opportunity to be your student.

Next, I would like to thank Henk Nijmeijer, who believed in my academic potential and gave the chance to be a part of this wonderful university. I am also grateful to Geertje Janssen-Dols who has been around to make things easy for me, just like she does for everybody in our group! Thanks to both of you, I was sure I didn't have to think about anything but my research during my PhD.

I want to thank my (ex-)office mates: Duarte Antunes, for our conversations about football and weekly matches; Elise Moers for answering all of my questions and her patient attempts to integrate me into Dutch culture; Maarten Hoeijmakers, for helping me at the very beginning by teaching the fundamentals of the FE program and measurement script I used throughout my study; Joris Michielsen for our discussions leading to the idea of the patch-impedance approach and showing me that being a father is not just responsibilities but also fun; Hefeng Zhou for his insistent attempts to integrate me into Chinese culture and his hospitality whenever I am in his turf; Daniël Veldman for contributing to this thesis by translating the summary into Dutch and listening to my complaints about, umm, everything. Also Igor Rodriguez and Andy Aribowo... We did not have the chance to spend much time, however thank you for the conversations and keeping the office live! Thanks to all of you, and the rest of the group, I have enjoyed my time in Gemini Zuid!

I would like to thank TANGO project for providing me with the funding for the research and introducing me wonderful people whom I enjoyed seeing in every project meeting: Hans Bodén, Susann Boij, Giovanni Campa, Alan Cummings,

Gunilla Efraimsson, Maria Heckl, Jakob Hermann, Paul Hix, Paula Martínez Lera, Wolfgang Polifke, Rick Scholte, R.I. Sujith, Joàn Teerling, Alp Albayrak, Alessandra Bigongiari, Nitin Babu George, Javier Crespo Anadón, Sreenath Gopinathan, Naseh Hosseini, Dmytro Iurashev, Nalini Mukharejee, Wei Na, Luck Peerlings, Driek Rowenhorst, Lin Strobio Chen, Aswathy Surendran and Jonathan Tournadre. I will definitely miss all the professional and social harmony we had. You really made TANGO more than just a scientific project. Furthermore, I would like to thank Kilian Förner and Chenyang Weng for the opportunity of working together and valuable discussions. Although they were not members of this project, we are connected through TANGO members.

I also want to thank Emma Machan for her critical and technical contribution to the design of the thesis cover. Your magical touch made the cover complete, Emma!

Bu tezle ilgili olmasa da haytımın genelinde çok önemli yerleri olan, arkadaştan da öte insanlara teşekkür etmek istiyorum fırsattan istifade ederek: Mustafa, senin yapıcı eleştirilerin; İlke, senin her konuya getirdiğin farklı bakış açısı; Özmen, vizyonunu geliştiren konuşmalarımız; ve Gökhan, senin engin hayat tecrübelerinin olmasa, hayatım şimdi olduğundan çok daha sıkıcı olurdu. Teşekkürler! İyi ki varsınız!

Hakkını asla ödeyemeyeceğim sevgili Annem ve Babam... Zamanında binbir güçlük kurmuş olduğunuz hayatınızı, sırf ben ve kardeşim daha iyi eğitim alabilsem diye bozup sıfırdan tekrar başlamanızın kıymetini her geçen gün daha iyi anlıyorum. Sizler o gün o fedakarlığı yapmasaydınız, ben şu anda elinide tuttuğunuz bu kitabın hayalini bile kuramazdım. Ve elbette Anneannem... Sen olmasaydın, sen bizleri yetiştirmeseydin, sen bizlere neşe kaynağı olmasaydın, ben bugün bu noktada asla olamazdım. Keşke sen de burada olsaydın...

Kardeşim, Akın... Sadece kardeşim değil, aynı zamanda en iyi arkadaşım ve meslektaşım... Mesleki konular da dahil, her şey hakkında konuşabileceğim biri olduğun için teşekkürler. Ben seninle aynı takımda olduğum için ne kadar şanslı olduğumun farkındayım, umarım sen de benim için ne kadar kıymetli olduğunun farkındasındır.

And Yolanda... My amazing wife... If it weren't for you, maybe I would never have the courage to start this adventure. You have given me all the support I could ask for and more. You put up with my frequent travels, unusual sleeping pattern and presentation rehearsals during this last four and a half years. As if all of these were not enough, you have even helped me producing this book by designing its cover. Now this one is over, I am looking forward to our next adventure. Continue inspiring me, my love!

